



TECHNISCHE
UNIVERSITÄT
WIEN
VIENNA
UNIVERSITY OF
TECHNOLOGY

DISSERTATION

Development, Construction and Application of a Portable X-Ray Fluorescence Device for Analysis of Art Objects

ausgeführt zum Zwecke der Erlangung des akademischen Grades eines Doktors der technischen
Wissenschaften unter der Leitung von

o. Univ. Prof. Univ. Doz. Dipl.-Ing. Dr. techn. Manfred Schreiner
Institut E164

Institut für chemische Technologien und Analytik

eingereicht an der Technischen Universität Wien
Technisch-Naturwissenschaftliche Fakultät

von

Mag. Vladan Desnica
Matrikelnummer 9126542
Gymnasiumstrasse 85
1190 Wien

Wien, im Februar 2005

A handwritten signature in black ink, appearing to read 'Vladan Desnica', is written in the bottom right corner of the page.

Acknowledgment

The work presented in this thesis was carried out at the Institute of Science and Technology in Art of the Academy of Fine Arts in Vienna in co-operation with institutes of the Vienna University of Technology in the years 2002-2004.

First of all I would like to thank my doctoral advisor Prof. Dr. Manfred Schreiner. He supported my efforts with his superior knowledge, guiding me and helping whenever I was in need, without restricting my ways when trying to solve a problem. His urge and desire in advancing the analytical capabilities of the institute opened new possibilities for me and made the work presented here possible.

I also wish to thank Prof. Dr. Michael Mantler, Institute of Solid State Physics of the Vienna University of Technology, for helpful discussions and all the support I have received from him throughout the last couple of years.

I wish to express my gratitude to Prof. Dr. Peter Wobrauschek, Atomic Institute of the Austrian Universities, for his eagerness to help and a wholehearted support.

Special thanks to my former fellow students Gerhard Hammerschmid and Christopher Ede for their enthusiastic and highly valuable support in helping to solve the problems encountered during the development of the instrument.

A huge thanks, of course, to all the members of the institute; especially Bernadette Frühmann, Ernst-Georg Hammerschmid, Dubravka Jembrih-Simbürger, Christine Jiru, Christoph Kleber, Robert Linke, Max Mäder, Michael Melcher, Karin Schädler, and Katharina Uhlir. Their scientific support as well as the wonderful working atmosphere they provided had me singing each morning when going to work.

Last, but definitely not least, a special “thank you” to my sister and my parents for their enormous support I have received throughout all these years. They stood behind me in everything, encouraging even my wildest endeavors. Thanks guys!

Kurzfassung

Röntgenfluoreszenzanalyse (RFA) gehört zu den am besten geeigneten Methoden für die Untersuchung von archäologischen, historischen und Kunstobjekten. Die Entwicklung von tragbaren RFA-Geräten, die einen Einsatz direkt vor Ort erlauben, ermöglicht eine noch breitere Anwendung dieser Methode an Objekten unabhängig von ihrer Größe, Form und dem Ort, an welchem sie aufbewahrt bzw. ausgestellt sind.

Diese Arbeit beschreibt die Entwicklung und den Bau eines portablen RFA-Geräts, das entwickelt wurde, um *in situ* Untersuchungen zu ermöglichen. Das Ziel war ein tragbares und handliches Gerät zu bauen, das aber gleichzeitig die Leistung und Genauigkeit eines Laborgeräts aufbringen kann. Bei der Komponentenauswahl wurde daher beachtet, dass sie gute Auflösung und schnelle Datenerfassungsvermögen besitzen, und gleichzeitig klein, leicht und robust sind. Der Messkopf des Systems besteht aus einer 50 Watt Röntgenröhre (50 kV, 1,0 mA, Modell 5011 der Fa. Oxford/USA), einem Silicon-Driftkammer-Detektor (SDD - Modell XFlash 1000 der Fa. Röntec/Deutschland) und zwei Laser-Pointer als Positionierungssystem. Unter Verwendung des mittels Peltier-Element thermoelektrisch gekühlten SDDs ist ein unhandliches und sperriges Detektorkühlsystem mit flüssigem Stickstoff nicht mehr notwendig. Bei typischen Arbeitsbedingungen wird eine Energieauflösung von < 150 bei 1 keps für die MnK α -Linie erreicht und mit Hilfe eines Pin-Hole Kollimators wird der Röntgenstrahl auf eine effektive Brennfläche mit ca. 1,5 mm Durchmesser fokussiert. Für die Steuerung von einzelnen Systemkomponenten, Datenübertragung und Datenerfassung wird eine auf LabVIEW Entwicklungsumgebung (der Fa. National Instruments/USA) basierende selbstentwickelte Software verwendet. Die gesammelten Daten werden anschließend mit Hilfe der WinAxil[®] Software (der Fa. Canberra Eurisys/Belgien) bearbeitet und analysiert. Zusätzliche weitere Miniaturisierungen am Instrument ermöglichen volle Freiheit der Positionierung und Verwendung des Gerätes auch außerhalb des Labors. Damit sind auch Untersuchungen und Analysen an Kunstobjekten z.B. von Wandmalereien direkt vor Ort möglich. Die Verwendung einer 50 Watt Röntgenröhre gewährleistet genügend hohe Strahlungsintensitäten auch für die Anregung kleineren Probenmengen, womit die mit dem portablen RFA-Gerät erhaltenen Ergebnisse mit den Laborwerten durchaus vergleichbar sind.

Einige konkrete Anwendungen des portablen RFA-Geräts sind als Fallbeispiele genauer beschrieben. Im Besonderen handelt es sich hier um Pigmentcharakterisierung der Wandmalerei an Wandfragmenten aus dem Wiener Stephansdom, der romanischen Wandmalerei in der St. Nikolaus Kirche in Winkl bei Wien, Charakterisierung von chinesischen Lacktafeln im Wiener Schloss Schönbrunn, sowie von belgischen Glasemailfragmenten aus dem 17. und 20. Jahrhundert.

Abstract

X-ray fluorescence analysis (XRF) is regarded as one of the most appropriate analytical techniques for examination of artistic, historic and archaeological objects. Development of XRF instrumentation suitable for portable employment expands the range of use of this technique to an even wider area, by allowing *in situ* measurements on objects disregarding of their shape, size or place where they are stored and/or displayed.

This thesis describes design, construction and assembly of a field portable XRF (PXRF) analyzer, which was developed in order to enable *in situ* examinations in the field of archaeometry. The goal to design a portable instrument with lab-like precision performance was achieved by careful selection of individual components based on several important factors - high precision, high-speed data acquisition, and at the same time undemanding and simple portability. The system is based on energy dispersive XRF using a 50 kV and 1.0 mA x-ray tube from Oxford Instruments, USA, type XTF5011, a silicon drift chamber detector (SDD) from Roentec, Germany, type XFlash 1000, and two lasers as pointing devices. The air cooled 50 W x-ray tube and the Peltier-cooled SDD provide a strong excitation source and a very efficient detection system resulting in fast measurements (short acquisition time) with very good precision – two highly important features in the field of archaeometric examinations. SDD circumvents the need of a bulky liquid N₂ detector cooling system. In combination with the overall miniaturization of all components and versatile positioning of the measuring head, it allows also high quality *in situ* measurements. For communication between the particular system components, for data acquisition and qualitative spectrum evaluation a software package based on LabVIEW[®] from National Instruments was developed and adapted to specific needs and requirements encountered in the field of archaeometry. The collected data are subsequently quantitatively analyzed using WinAxil[®] Software from Canberra Eurisys, Belgium. To fully evaluate the assembled instrument, the system's analytical capabilities are tested, compared with the results obtained by a laboratory XRF, and a comparative evaluation of the systems is established.

After the completion of construction, the instrument was used for studies of art objects in museums and galleries, ceiling frescoes in churches and cathedrals, archaeological findings at

the excavation sites etc. Several case studies, where the PXRf has been utilized, have been presented in more details, in particular characterization of mural paintings on the wall fragments from the St. Stephan's Cathedral in Vienna, Romanesque mural paintings from the St. Nicholas church in Winkl, Chinese wood panel lacquer decoration (lacquerware) in Schoenbrunn Castle in Vienna, and Belgian enameled stained glass fragments from the 17th and the 20th century.

Abbreviations

CC – Cryogenically Cooled

CdZnTe – Cadmium Zinc Telluride

EDXRF – Energy Dispersive X-Ray Fluorescence

EPMA – Electron Probe Micro-Analysis

ER – Energy Resolution

FET – Field Effect Transistor

FWHM – Full Width at Half Maximum

HgI₂ – Mercury Iodine

HPGe – High Purity Germanium

IR – Infrared

LN₂ – Liquid Nitrogen

MCA – Multi-channel Analyzer

MDL – Minimum Detection Level

ÖGUSSA – Österreichische Gold- und Silber-Scheideanstalt (Austrian Gold and Silver Separation Institute)

PIXE – Particle Induced X-Ray Emission

PXRF – Portable X-Ray Fluorescence

SDD – Silicon Drift Detector

Si(Li) – Lithium drifted Silicon detector

SR-XAFS – X-ray Absorption Fine-Structure using Synchrotron Radiation

Si-PIN diode – A silicon diode consisting of intrinsically pure silicon layer (I) diffused with P- and N-regions on both sides

TC – Thermoelectrically Cooled

WDXRF – Wavelength Dispersive X-Ray Fluorescence

XRF – X-Ray Fluorescence

Contents

Acknowledgment	1
Kurzfassung	2
Abstract	4
Abbreviations	6
Contents	7
1. Introduction	9
1.1. Development of XRF Spectroscopy as a Portable Application	10
2. Basic Principles	15
2.1. X-Rays Interaction with Matter	15
2.1.1. Matrix Effects on XRF Intensity and Mathematical Corrections	19
2.1.2. Further Influence Factors on XRF Intensity	22
2.1.3. Question of (Non-)Destructiveness of XRF and Radiation Damage	24
3. Component Selection	26
3.1. X-Ray Source	28
3.1.1. Excitation Types	28
3.1.2. Tube Cooling	29
3.1.3. Anode Material	29
3.1.4. High Voltage Power Supply	31
3.2. Focusing/Collimating the X-Rays	31
3.2.1. Capillary Optics	32
3.2.2. Pin-Hole Collimation	32
3.3. Pointing Device (Alignment System)	35
3.4. Detector	36
3.4.1. Compact Detectors	37
3.4.2. Principles and Advantages of SDD	37
3.5. Assembly of the Main Components	41
3.6. Analyzing Electronics (Spectrometer)	43
3.6.1. Signal Shaping Time and Energy Resolution Dependency	43

3.7.	Communication between Components, Data Acquisition, Evaluation, and Presentation	45
3.7.1.	Development Software LabVIEW	45
3.7.2.	Component Control and Acquisition	45
4.	Instrument Operation and Test Measurements	47
4.1.	Selection of Efficient Operating Conditions	47
4.1.1.	X-Ray Tube Operating Voltage	48
4.1.2.	X-Ray tube Operating Current	50
4.2.	Component Tests	50
4.2.1.	Stability Tests	50
4.2.2.	Rh-Tube Excitation Spectrum Energy Distribution	52
4.2.3.	Beam Diameter – Measurements with a Cu-Wire and Micro-Stage	54
4.2.4.	Sum Peaks Effect and Speed Processing Electronics	55
4.3.	Care and Maintenance of the PXRF System	57
4.3.1.	X-Ray Source	57
4.3.2.	Detector Maintenance	58
4.4.	Improvement Suggestions	58
4.4.1.	Secondary Radiation for Excitation	58
4.4.2.	Primary Filters	59
5.	Case Studies and Experimental results	60
5.1.	Mural Paintings on Fragments from the St. Stephan's Cathedral in Vienna	60
5.2.	Chinese Lacquer Panel Paintings in the Schoenbrunn Castle in Vienna	68
5.3.	Mural Paintings in the Church of St. Nicholas in Winkl	70
5.4.	Research of the Enameled Stained Glass Fragments	76
6.	Summary and Conclusions	82
7.	References	85
Appendix A – Analysis Software Manual		
Appendix B – Absorption Edges for Some Important Elements		
Appendix C – High Voltage Interface		

1. Introduction

The widespread use and number of different instruments that have been developed and employed for the application of x-ray fluorescence analysis (XRF) illustrates well the established value of this analytical method. The most general use of this technique, dating from the early 1900s [1], is turned toward the characterization of materials, i.e. a determination of the properties and as an extensively non-destructive method it is vastly used for investigations on artistic, historical and/or archeological samples/objects. Among the other truly non-destructive methods are the spectroscopies based on ultraviolet, visual and infrared (IR) radiations as well as x-ray based methods [2]. Such techniques allow analytical information to be obtained with no damage to the sample or to the artifacts in question. In that case all visible damage is avoided and the objects under examination remain aesthetically unimpaired. The option of using these types of methods is of great advantage when sampling is not feasible or when fragments used for analysis need to be put back in their original location after the investigation.

According to Lahanier et al.[3], an ideal method for analyzing objects of artistic, historic or archeological nature should be *non-destructive* (to eliminate sampling and avoid any alteration of the object's structural and chemical integrity), *fast* (so that large numbers of similar objects may be analyzed or a single object analyzed at various measuring points), *universal* (so that many objects of various shapes and sizes can be analyzed), *versatile* (to allow obtaining average compositional information but also permit local analysis of small areas), *sensitive* (making possible the use of trace-element fingerprints) and *multi-elemental* (so that in a single measurement, information on many elements is obtained simultaneously and, more importantly, information is also obtained on elements which were not initially thought to be relevant to the investigation). Because XRF meets most of these requirements it is one of the most appropriate and most used analytical methods in the field of archaeometry [4, 5].

The technological advances such as miniaturization of x-ray sources, detectors and other components, helped analytical instrumentation to become smaller, allowing us to start developing field-portable XRF systems for *in situ* investigations. One of the limiting factors of the conventional XRF instruments is that they cannot be easily transported to the museum, gallery or archeological site where the usually valuable objects of interest are stored or displayed. This can, in fact, represent a restricting issue for the archaeometric examinations, arising from

practical, bureaucratic or safety problems. It is only by portable systems that non-destructivity - one of the most attractive features of this technique - can be fully exploited. Thanks to the possibility of working *in situ*, portable spectrometers have virtually extended the range of use of XRF to any type of object.

This thesis describes the development, construction, and first analytical applications of a small beam portable XRF (PXRF) instrument for *in situ* measurements. The goal was to design an instrument which will approach lab-like precision performance, but still remains portable. For that purpose, the individual components were carefully decided on, with selection being based on several important factors - high precision, high-speed data acquisition, and at the same time undemanding and simple portability. The chosen components were subsequently assembled in a compact and manageable way, and tested to comply with the above requirements. Furthermore, Chapter 4 may serve as a fundamental manual on PXRF utilization, giving essential guidelines for the instrument conditions settings and maintenance propositions.

1.1. Development of XRF Spectroscopy as a Portable Application

Material analysis of our cultural heritage goes a long way before the first x-ray experiments were conducted and is almost as old as the scientific documentation of objects of art and archaeology itself. The first reports of chemical composition analysis date to the late 18th century (1795), when Prof. Martin H. Klaproth (1743-1817) of the University in Berlin reported on investigation of Roman coins, ancient alloys and glass based upon gravimetric analyses and on newly developed chemical recipes for the separation of Cu, Pb and Sn, and their quantitative determination [6-8]. However, during his studies great amounts of sample material had to be destroyed, a procedure which would hardly comply with the requirements and ethics of today's conservators and curators.

At the beginning of the 20th century, as the apprehension for the importance of cultural heritage continually grew, other analytical procedures, which significantly reduced the amount of sample material needed for the analysis, i.e. microchemical techniques [9-15] and spot tests [16, 17], have started emerging.

In 1913, the same year when Henry Moseley laid a foundation for qualitative and quantitative x-ray analysis by discovering a relationship between the wavelength (energy) of x-ray spectral lines and the atomic number of the elements [18], Coolidge introduced the hot-filament, high-vacuum x-ray tube [19]. When using that device, solids or powders were placed directly on the x-ray tube anode target and their characteristic radiation, after being dispersed using a calcite crystal, was recorded on a photographic film. First quantitative analysis using a secondary target was conducted only ten years later, by Coster and von Hevesy [20]. In 1928, Geiger and Müller improved the reliability of their famous gas-filled detector to a degree which allowed its routine use [21]. But it was only twenty years later, in 1948, when Friedman and Birks built the very first prototype of the first commercial spectrometer, that x-ray spectrometry reached its full analytical potential [22].

The principle underlying of this technique is the excitation of the atoms by means of mono- or polychromatic x-ray radiation. During sample irradiation, inner shell electrons of the elements in the sample absorb specific x-ray photons and are ejected from the atom. The excited atoms subsequently return to ground state under emission of the so-called fluorescent x-rays, whose energies are characteristic for the elements from which they originate. These energies can then be used for qualitative and quantitative characterization of the samples.

The first generations of the x-ray fluorescence spectrometers were based on the wave length dispersive detection and because of their very good resolution this systems are still being widely used today. In wavelength-dispersive x-ray fluorescence (WDXRF) spectrometry, the polychromatic beam emerging from a sample surface is dispersed into its monochromatic constituents by the use of an analyzing crystal according to Bragg's law ($n\lambda = 2d \sin\theta$, where λ denotes the wave length, d the separation between atomic planes in the crystal used, and θ the diffraction angle). The wavelength for any measured line is therefore computed from a knowledge of the crystal parameters (d values) and diffraction angle. However, because d is fixed for a given crystal, the maximum value of λ , that can be measured, is $2d$, so that several crystals are required and must be interchanged within the instrument for a wide wavelength range to be covered. In a sequential WDXRF spectrometer the crystals are turned and the spectrum is measured sequentially scanning the wavelengths by changing the 2θ angle. The elements and their concentrations are identified by the spectral intensities. The intensities are detected using a proportional counter and/or a scintillation counter. These instruments offer excellent spectral resolution, but their size and weight as well as a need of high-power x-ray

tube sources never really made it a candidate for miniaturization and employment as a portable system. Only one known example of a non-laboratory WDXRF spectrometer exists, under the trade name of Portaspec [23], and it has been used exclusively for alloy analysis.

The development of the energy dispersive x-ray fluorescence (EDXRF) depended highly on the evolution of the semiconductors, which came after the invention of the transistor in 1948. One of the by-products in the progress of this technical revolution was a development of the new family of detectors for nuclear radiation. These detectors, based on silicon and germanium crystals doped with lithium, offered spectroscopists an energy resolution almost 10 times better than that of standard, gas-filled proportional counters. It was this improvement in the detector technology, which in the early 1970s yielded a solid starting ground for the rapid development of the EDXRF systems [24, 25]. Such a spectrometer makes use of the fact that the pulse height of the detector signal is proportional to the x-ray photon energy, which is correlated with the wavelength. The elements and their concentration are identified by counting the pulses at the different energy levels and a multichannel analyzer is used to provide and display the data. Here each channel counts the number of photons with a certain energy level (i.e. from every element in a sample) simultaneously and in real time. This makes this technique extremely versatile and the identification of the elemental constituents in a sample very efficient. In other words, the dispersion takes place in the energy rather than in the wavelength domain. Unfortunately, EDXRF suffers from more severe line overlaps than WDXRF does. Also, the sensitivity for the light elements (e.g. carbon and nitrogen but also sodium and magnesium) is much lower than with WDXRF, and, consequently, the lower limit of detection is worse (0.02 % for sodium with WDXRF versus 2 % for sodium with EDXRF) [26].

As already stated, the WDXRF systems need very high-power x-ray tubes, in order to compensate for significant losses of incident beam intensity. In an EDXRF spectrometer the optical path is simpler because no crystals or goniometers are needed so the fluorescence photons from the sample hit the detector directly. Therefore, the samples can be irradiated by x-rays from a tube with lower power than that used with the WDXRF spectrometers. This feature, as well as the fact that the detection system became much lighter and simpler, made it possible to build EDXRF systems smaller and more compact. Subsequently, it allows even more versatile utilization of the method and enables investigations of bigger and bulkier objects.

The absence of analyzing crystals and bulky goniometers in EDXRF systems allowed specimens to be placed very close to the detector without compromising the analytical performance, thus making it possible to employ even weaker excitation sources. Therefore, the next big step in opening the door to a field application of XRF systems was introduction of radioisotope sources as means of sample excitation in the late fifties [27]. Such radioisotopes are ^{55}Fe , ^{109}Cd and ^{241}Am . The very first portable designs using such sources were targeted at less demanding, single analyte applications such as sulfur in oil, which did not require the best possible detector resolution [28, 29], and those early designs are sometimes referred to as first-generation portable instruments. To improve the energy resolution of these portable XRF systems, specifically for adjacent analytes, whose atomic numbers Z did not differ by more than 1, mechanical means in form of so-called *balanced filters* were used [23]. But if a rather strong excitation x-ray source is an imperative (power of an order of 50 W), one will still opt for a conventional x-ray tube. Unfortunately, throughout the years there has not been a lot done to improve this system. Over the last decades the sources have become somewhat smaller and more compact, but the theory and practical execution of the design has not changed as drastically as it was the case with detection systems.

As already mentioned, it was in the mid-seventies when the design of a small, gas-filled proportional detector with improved resolution resulted in the first truly portable, energy dispersive x-ray analyzer, which was capable for multi-elemental analysis without balanced filters [30]. The early eighties brought with the development of microprocessors and electronic memory a new group of portable EDXRF systems, which could now contain onboard interactive calibration software, and allow the electronic storage of the results. Regarding the detectors, the efforts were directed toward improving the existing gas-filled proportional counters and at adapting new semiconductor materials for a new generation of detectors. The first portable system to introduce a room-temperature semiconductor detector was Metallurgist-XRTM of Texas Nuclear Corporation using a mercuric iodide as detector material [31].

Recently, non-cryogenic detectors, like silicon PIN diodes, simply cooled by a Peltier element have been introduced. Because of the big improvement in terms of their size and weight they are being readily employed in portable systems for XRF analysis [32, 33, 34]. The system is rather compact, so it enables the construction of measurement heads to be used for *in situ* analyses. Their energy resolution is in the order of 220-250 eV FWHM at 6 keV, which is sometimes not satisfactory for archaeometrical purposes, especially for the identification of

light elements [35]. Nevertheless, the application of silicon PIN diodes to XRF analysis is today widely spread, and the commercial availability has led to be used in other applications as well (i.e. PIXE, SR-XAFS etc.) [36-40]. Due to the reduced thickness of the Si-diode, the efficiency of this detector rapidly decreases beyond 25-30 keV [41].

Further advances in silicon-based semiconductor energy dispersive detectors brought another new detection module based on the silicon drift detector (SDD), first introduced by Gatti and Rehak in 1983 [42]. Due to the on chip electronics and the very small size of the anode, the anode capacitance is drastically reduced, which consequently reduces the electronic noise. Therefore, very good energy resolutions can be obtained already at room temperatures or further improved with the help of a simple Peltier stage (i.e. in the order of 150-160 eV FWHM at 6 keV) [43, 44]. Because of the compact size of such detectors (thermoelectrically cooled, therefore no need for liquid nitrogen) and energy resolution that is comparable to that of conventional Si(Li) detectors, the SDDs are becoming more and more applied as standard detector systems in compact and portable XRF instrumentation [45, 46].

All these technological developments led to a really rapid increase of use of portable XRF systems. The expansion of the XRF method into the field of portable, *in situ* applications is a rather recent development, a little more than 30 years old [47]. The great number of recent reports on PXRF employments in the field of archaeometry [48-62] proves once again the importance, great advantages, and expanded usability of such a small, versatile and precise instrument.

2. Basic principles

2.1. X-rays Interaction with Matter

X-rays, together with γ -rays, constitute the range of the electromagnetic spectrum having the highest energy. From this range a typical span of wavelengths used in x-ray fluorescence analysis lays between 0.02 nm and 2 nm, which corresponds to an energy range of 0.6 to 60 keV. When this electromagnetic radiation interacts with matter (atoms), they produce secondary radiation that carries useful information about the atoms comprising the target.

The radiation is emitted from its source in form of a spherical wave and its intensity decreases with the second power of the distance from the origin. By passing through the matter the intensity sinks further due to attenuation. The physical attenuation processes that cause this effect are scattering and photoelectric absorption, which depend highly on the energy of the incident radiation as well as from the composition of the irradiated matter [25]. These mechanisms influence not only the constructional aspects of an XRF spectrometer, but have an effect on analysis and evaluation of the XRF spectra as well. Depending on the area of the use for a given XRF analyzer its components have to be customized and optimized to cover and adapt to the specific field they are being used in. For example, in order to obtain the best possible fluorescence to background intensity ratio one has to take two important factors into consideration. The excitation of the examined line has to be optimized and at the same time the widest possible range of the characteristic spectrum should be acquired.

The scattering occurs during the interaction between the x-ray photon and the absorber matter, when the atomic electrons are so tightly bound to the atom that no ionization or excitation is possible. If the collision has an elastic character (no energy loss) the scattering is called *elastic (Rayleigh) scattering*. Because there is no change in the energy during the process, the wave length of the scattered radiation is the same as the wavelength of the incident radiation. It can be readily accepted that the condition for elastic scatter would be favored for low incident photon energies and for high atomic number (high Z) target atoms, where the electrons are more tightly bound [63].

But it can also happen that an x-ray photon loses a part of its energy during the collision, especially if the electrons are loosely bound. This effect is referred to as *inelastic (Compton) scattering* and the energy of the scattered photons is lower than that of the incident radiation. The angle at which the photon is scattered can take on any value and the energy imparted to a free electron correspondingly has a continuous distribution from zero to maximum of E_{\max} when the photon is scattered through 180° :

$$E_{\max} = \frac{2E_0^2}{m_0c^2 + 2E_0} \quad (2-1)$$

where E_0 is the incident x-ray energy and m_0 is the electron rest mass. For all other angles, θ , the Compton shift may be conveniently represented as:

$$E = \frac{E_0(1 - \cos \theta)}{m_0c^2 + E_0(1 - \cos \theta)} \quad (2-2)$$

For a spectrometer with a beam-sample-detector geometry of 90° , a Compton scattered Ag K α line (22.104 keV) from a silver x-ray tube will be observed at 21.186 keV.

The photoelectric effect, mostly responsible for the absorption of radiation in the matter, causes the change in the intensity $I(\lambda)$ of the radiation passing through the absorber along the path x_i for a given wave length λ :

$$I(\lambda) = I_0 \exp[-(\mu_i \frac{\rho N}{A} x_i)] \quad (2-3)$$

μ_i is the absorption coefficient of the absorber i ; ρ , A and N represent the density of the absorber, atomic number and Avogadro's number, respectively. The atomic attenuation coefficient μ_i , in units of cm^2 or barns ($= 10^{-24} \text{ cm}^2$), is the usual choice, which describes the physics of interactions [64].

The photoelectric absorption occurs in every energy level of an atom; hence, the total photoelectric absorption τ_{tot} is a sum of single level photoelectric absorptions:

$$\tau_{tot} = \tau_K + \tau_{L_I} + \tau_{L_{II}} + \tau_{L_{III}} + \tau_{M_I} + \dots + \tau_n \quad (2-4)$$

where τ_n is the most outer level of the atom, still occupied with electrons.

In the photoelectric absorption the energy brought in by the photon is used to eject the electron, and the remainder of the energy appears as kinetic energy of the now free electron, i.e. the incident photon is completely absorbed. This process requires a minimum energy or critical energy equal to the binding energy of the electron. The probability for the photoelectric effect exhibits characteristic discontinuities, the so-called absorption edges, which occur at the critical energy for the shell in question. The maximum probability for the photoelectric effect occurs when the photon energy is just above the critical energy. Among the considerations for maximum analytical efficiency, this defines one of the important considerations in x-ray fluorescence analysis: the analytical efficiency for a given element is enhanced by exciting the target with the photon energy as close as practically possible to (but higher than) the critical energy. In other words, the excitation of a line succeeds the best if the x-ray radiation used for the excitation has the energy right above the line's absorption edge. For a photoelectric process with an x-ray of energy near the K shell binding energy the cross section for an x-ray with frequency ν is given approximately by:

$$\sigma_{ph} \propto \frac{Z^5}{\nu^3} \quad (2-5)$$

The fluorescence yield is not expected to be constant for all the elements, but varies with Z as shown in Fig. 2.1.

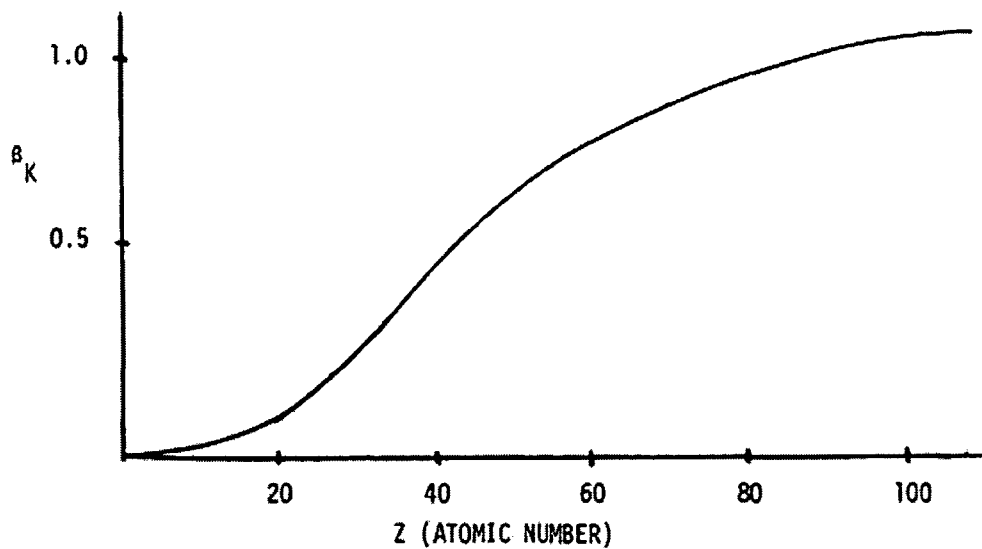


Fig. 2.1: Fluorescence yield as a function of atomic number [63].

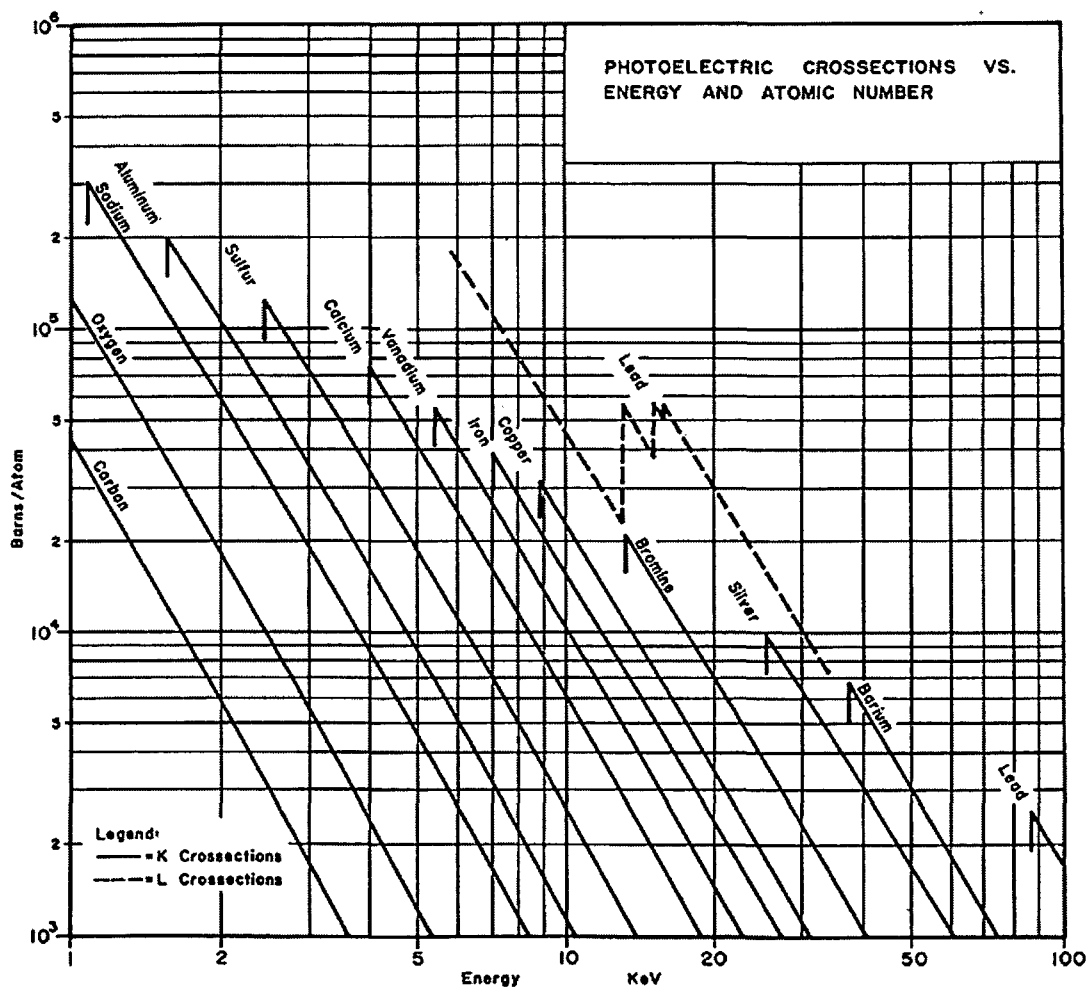


Fig. 2.2: Photoelectric cross section vs. energy and atomic number [63].

Furthermore, when choosing appropriate spectroscopic conditions, it should be kept in mind that the photoelectric effect is increasingly probable with the decreasing energy of the fluorescing radiation, and the increasing atomic number of the target. Fig. 2.2 exhibits this trend for the photoelectric cross section for selected elements. The practical consequences and concerns of this effect will be additionally discussed in Chapter 4.

2.1.1. Matrix Effects on XRF Intensity and Mathematical Corrections

The intensity, or the number of counts in a peak, is a direct result of the number of excited i.e. fluorescing atoms of the specific element in a sample. Thus, the area under a peak is proportional to the concentration of that element in the sample. But the relation of intensity to a real concentration of the element in a sample is affected by several factors. Except for the effects of the surface conditions (should be smooth and flat) and the particle size distribution (as particle size increases, intensity decreases), which can both be usually resolved by adequate grinding and sample preparation, the measured x-ray intensity can also be affected by interelement absorption and enhancement effects within the sample. The absorption effect originates because atoms within the sample matrix may absorb x-rays emitted by other atoms before they reach the detector. This effect causes decrease of the measured intensity below the expected values and the ability of an element to absorb x-rays increases with its atomic number. On the other hand, the enhancement effect is caused by atoms not excited by the original x-ray source (tube), but by x-rays from neighboring atoms. In this case, the intensity is higher than expected. Therefore, in order to obtain accurate quantitative results from the collected data (spectra), the general requirements include not only adequate sample preparation and good standard reference materials, but also mathematical corrections for matrix effects (absorption and enhancement). With the use of the appropriate theoretical methods not only concentrations of bulk materials can be computed, but also of thin layers and multiple layer structures. In addition, layer thicknesses (mass thicknesses) can be determined [65].

Having that in mind, the characteristic radiation intensity from the sample is determined by the intensity of the radiation from the x-ray source as well as from the absorption characteris-

tics of the sample material. The total fluorescence yield for a given element i in a matrix with j elements can be calculated using:

$$I(\lambda_i) = P_i W_i \int_{\lambda_{\min}}^{\lambda_{\text{Edge}}} J(\lambda) \frac{\mu_i(\lambda)}{\sum_j \alpha_j W_j} \cdot d\lambda \quad (2-6)$$

where $I(\lambda_i)$ stands for the intensity of the characteristic radiation, W_i for the weight proportion of the element i and P_i for a factor of proportionality in regard to the geometrical arrangement and the excitation conditions [66]. The integral over $J(\lambda)$ characterizes the x-ray excitation source spectrum within the excitation boundaries, i.e. from the shortest wave length of the continuum to the absorption edge of the element i .

There is a great number of correction algorithms available, but, in general, three basic approaches are used: calculations from fundamental parameters, interelement influence coefficients, and correction with scattered radiation.

The basis of a scattered radiation correction method is that, for a given concentration of some analyte, the intensities of the analyte radiation and primary radiation (from the excitation source) scattered by the specimen at a wavelength near the analyte line are affected in the same way by absorption of the sample [67]. Therefore, their ratio should be almost independent of the matrix, and, in fact, this ratio has been found to be almost completely insensitive to excitation conditions, particle size, and the packing density of the samples. The scatter method is applicable only to those elements with a higher atomic number than the major constituents.

Another widespread method for correction of absorption and enhancement is the use of interelement influence coefficients. In that routine the effect of the matrix elements j , on the analyzed element i can be described by the α coefficients in the empirical parameter equation:

$$\frac{c_i}{R_i} = 1 + \sum_{j \neq i} \alpha_{ij} c_j \quad (2-7)$$

which is also widely used to compute concentrations c_i from count ratios R_i [68]. The simplified version of the equation can be written as $\frac{c_i}{R_i} = 1 + \alpha_{iM} c_M$, where M denotes the general influence of the matrix. The ideal solution is $\alpha_M = 0$ (neutral matrix) and consequently $R_i = c_i$. If α_M is a positive number, lower count rates must be expected (absorbing matrix), while negative numbers indicate higher count rates (enhancing matrix). The coefficients can be calculated empirically from a set of multielement standards through a multiple least-squares approach or from one of the many algorithms [69, 70, 71 and 72]. Alternatively, the coefficients can be calculated from fundamental parameters [73].

The fundamental parameter method was developed in 1968 [74] and the principle consists of assuming an approximate composition for the unknown specimen calculating the fluorescence intensities from fundamental equations, and comparing it with the measured intensities. Successive adjustments of the composition are made until the theoretical and the measured intensities are consistent. Conventional fundamental parameter approaches describe the number of fluorescent photons emitted from a specimen by the sum of photons from primary and secondary radiation, i.e., those derived directly from tube photons (or electrons in case of SEM or EPMA), and those derived by subsequent process by such directly excited photons. Mathematical models can be based on closed sets of equations or on Monte Carlo simulations [75]. It should be noted here, that from a technical point of view the Monte Carlo method is slower and less accurate (within a given computing time-frame), but there exists almost no restrictions with respect to shape and type of the inhomogeneities. A graphically oriented software package, which is capable of processing such information, has been developed by Mantler [65].

The physical (fundamental) atomic parameters involved in the mathematical models are the concentrations of the chemical elements c_i , their absorption coefficients $\mu = \tau + \sigma$ (total, photo-absorption and scattering), the absorption edge jump ration (assuming K-ionization) S_K , the probability for the expected transition relaxing the excited state (assuming $K\alpha$) $P_{K\alpha}$, the probability for emission of a photon (rather than of an Auger-electron, for the K-shell) ω_K , and the number of primary tube photons of energy E , $I(E)dE$. The number of $K\alpha$ -fluorescent photons emitted from a layer of thickness D and density ρ is then:

$$dn_{K\alpha} \propto \frac{\Omega}{4\pi \sin \psi_1} \frac{\rho}{\rho_i} w_i \tau_i(E) \frac{S_K - 1}{S_K} P_{K\alpha} \omega_K c_i A(E, K\alpha) \frac{I(E) \left(1 - e^{-D\rho \left(\frac{\mu(E)}{\sin \psi_1} + \frac{\mu(K\alpha)}{\sin \psi_2} \right)} \right)}{\frac{\mu(E)}{\sin \psi_1} + \frac{\mu(K\alpha)}{\sin \psi_2}} dE \quad (2-8)$$

The differential dn denotes the fact that only a monochromatic region of the generally polychromatic primary spectrum is taken into account, and a summation over all available photons must be carried out. The angles ψ_1 and ψ_2 are the angles of incident and observed radiations with respect to the specimen surface. $\Omega/4\pi$ is the fraction of $K\alpha$ -photons from element i emitted into the aperture of the detector. The factor $A(E, K\alpha)$ stands for the shielding effect by the layers above (i.e., towards tube and detector) the analyzed layer in a multilayer structure.

2.1.2. Further Influence Factors on XRF Intensity

As mentioned earlier, there are further effects that influence the intensity of the fluorescent radiation, i.e. the number of counts in a peak, and might need to be taken into account. One of them is the particle size distribution in the sample. But for the pigments the size of a typical pigment grain is around 1 μm , depending on the manufacturing process. Historical pigments are often much larger and those made by modern industrial producers sometimes much smaller. A not too great number of Monte Carlo simulations has been carried out so far on such systems, but they suggest that the error introduced by this inhomogeneity is low and usually need not be taken into account unless the average grain size exceeds about 5 μm (depending on the matrix)[76].

The intensity of radiation (more correctly, the number of photons) which is eventually observed in the detection system is a function of the composition of the specimen and its thickness D , where:

$$D = \frac{1}{\rho \left[\frac{\mu(E)}{\sin \psi_1} + \frac{\mu(K\alpha_1)}{\sin \psi_2} \right]} \quad (2-9)$$

emits about 63,2 % of the fluorescent intensity of an infinitely thick bulk material, and correspondingly more for thicker layers [75]. Secondary excitation effects may alter this expression slightly. As an information depth it is reasonable to define (arbitrarily) $D_{inf} = 3D$. Therefore, the information depths depend on the absorption coefficients (and thereby on the photon energies) $\mu(E)$ and $\mu(K\alpha_1)$ as well as on the angles ψ_1 and ψ_2 .

Sometimes the energy lines of some analyzed elements can be of very different energies, in most cases a K- and L-line (e.g. Cd K α and Cd L α in cadmium yellow/red/orange or Ba K α and Ba L α in permanent white). Because of their lower energy, there is a much higher absorption of the L-lines, hence, their information depth is much lower. This effect can sometimes be used for the analysis of layered materials (pigments). One should though pay special attention to the case, when the absorption edge of a matrix element in the material happens to have an energy between the K α and K β lines of an element, because in that case the K β /K α ratio of the element to be analyzed is a sensitive function of the concentration of the absorbing matrix element [68].

Decrease of the x-ray intensities of the primary and fluorescence radiation during the measurements under atmospheric conditions is a consequence of attenuation of the photons in the air. The low energy radiation is influenced by this effect the most, so for analysis of light elements the reduction of the optical radiation path is of utmost importance. The effect of this may well be seen when considering that the intensity of the P-K α (2.015 keV) characteristic radiation in air in 11 mm drops down to a half of its initial value [77]. Needless to say, this leads to a noticeable decrease of the signals needed for the analysis.

2.1.3. Question of (Non-)Destructiveness of XRF and Radiation Damage

As already mentioned in Chapter 1, Introduction, and as often seen in the works reporting on the use of XRF in archeology, this method is generally referred to as non-destructive. But to what extent is this assumption correct and what are the limiting values regarding the measurement parameters for that statement? What is the exact meaning of the term non-destructivity? Before the analytical procedure the specimen may first need to be prepared to fit into a specimen holder, meaning it may have required cutting or grinding, and has possibly undergone also further treatment by cleaning, polishing, coating etc. If the further analytical procedure doesn't alter the specimen's condition, it is said to be non-destructive. However, even this process of taking a specimen from an object and preparing it for the analysis may be a destructive step by itself and unacceptable from the viewpoint of a conservator, an art historian, or archaeologist. With the development of the XRF systems a number of analyzers have been built and employed for investigation of small areas of large objects without the need to sample the object, remove any material or even touch the object. The downside of such systems is that they are limited regarding the elements that can be analyzed in air (or under a protective, light gas) and roughness and surface contamination may affect the quality of quantitative analysis [45, 50].

Furthermore, one has to consider the possible damage caused by the radiation using XRF methods. The radiation damage by x-rays can be defined as the permanent alteration of the chemical state of atoms (bound to other atoms) in the specimen. In general, this process is cumulative and its effect approximately a function of the product of the photon flux, time and the particular photon energy, i.e. of the absorbed total radioactive dose. Being a cumulative, photon conditioned process, it is not only limited to x-rays, but can occur during illumination with any other intense electromagnetic radiation, particularly by visible and ultraviolet light (natural daylight). Having that in mind, a short duration of exposure to x-rays during an investigation is therefore not necessarily more harmful than exposure to natural (day)light over a period of many years. The one effect of the high radiation dose in many materials, that is most visible, is a permanent or temporary darkening (yellowing) of the irradiated area. Not only organic materials are affected by this, as the deterioration has been observed, e.g. at a polished copper surface or at most glasses as well. Organic materials are, however, particularly sensi-

tive and, besides darkening, they may even visually decompose and become mechanically brittle, as it was observed, for example, after prolonged exposure of white fabrics to x-rays [68, 78]. Still, when the XRF method is used in a typical regime (e.g. with a maximal energy of 2.8 kW at 60 kV and with most measurements carried out at 50 kV and 10 mA (0.5 kW), and an acquisition time for one spectrum of 30 s), the same authors report that they observed no radiation damage at any object analyzed in the 8 years of operation.

3. Component Selection

Portable x-ray fluorescence instruments for *in situ* measurements should employ simple, compact, and lightweight components and must be able to produce x-rays of satisfactory intensity while still having a small beam diameter. The correct selection of the components when designing and building such an instrument will have a crucial impact on its precision, usefulness, and of course on its economically-technical feasibility. A number of differently designed and executed PXRF systems have been so far described in the literature. Table 3.1 gives an overview.

Reference	Excitation			Collimation of primary beam	Detection ¹	Estimated weight [kg] ²
	Type	Max. Power	Cooling			
Hall et al. [62], 1973	Mo anode and ²⁴¹ Am	30 W (30 kV, 1 mA) + 20 mCi	air	not specified	CC Si(Li), ER 160 eV	60, including electronics
Cesareo et al. [49], 1996	W anode	50 W (50 kV, 1 mA)	air	pin-hole, 2.5 mm	TC HgI ₂ , ER 200 eV or TC Si-PIN, ER 250 eV	8, only the mobile part
Lutz et al. [79], 1996	Rh anode	17.5 W (50 kV, 0.35 mA)	air	not specified	TC Si(Li), ER 170 eV	40
Ferretti et al. [80], 1997	W anode	240 W (60 kV, 4 mA)	water	pin-hole, 2 mm	CC HPGe, ER 195 eV	20, only the mobile part
Longoni et al. [45], 1998	W anode	3 W (30 kV, 0.1 mA)	air	not specified	TC SDD, ER 155 eV	5, only the mobile part

Reference	Excitation			Collimation of primary beam	Detection ¹	Estimated weight [kg] ²
	Type	Max. Power	Cooling			
Ferrero et al. [53], 1999	Rh anode	50 W (50 kV, 1 mA)	air	methacrylate system, 5 mm	CC Si(Li), ER 140 eV + TC CdZnTe, ER 340 eV	not specified
Vittiglio et al. [34], 1999	Mo anode	60 W (60 kV, 1 mA)	Air	pin-hole, 0.3 mm	TC Si-PIN, ER 190-220 eV	ca. 3.8 kg, the mobile part
Caneva et al. [81], 2000	W anode	240 W (60 kV, 4 mA)	water	pin-hole, 3 mm	TC Si-PIN, ER 250 eV	25
Sugihara et al. [51], 2001	Rh anode	50 W (50 kV, 1 mA)	not specif.	type not specified, 2-10 mm	TC Si-PIN, ER 250 eV	20 including electronics
Ferrero et al. [54], 2001	Rh anode	50 W (50 kV, 1 mA)	air	methacrylate system, 5 mm	TC CdZnTe, ER 340 eV + TC Si-PIN, ER 220 eV	not specified
Cesareo [52], 2003	W anode	1.75 W (35 kV, 50 μ A)	air	< 1 cm ²	TC Si-PIN, ER 200 eV	not specified

¹ - CC = cryogenically cooled; TC = thermoelectrically cooled; ER = energy resolution for FWHM at 5.9 keV

² - Weight estimated by the authors

Table 3.1: An overview of some portable XRF systems reported in the literature, including the relevant features.

3.1. X-ray Source

3.1.1. Excitation Types

The excitation of the elements in a sample to emit their characteristic x-ray radiation can be accomplished by several means: by bombardment of the target using high energy electrons or accelerated charged particles, or irradiation by x-rays. The use of high energy particles as well as electrons is not of practical value in the methodologies of portable analytical applications of x-ray analysis. The use of x-ray radiation for excitation of the elements in a sample/object is a more realistic and functional approach. The further choice with photon radiation is either to use radioactive isotopes or an x-ray tube.

Radioactive isotopes which emit gamma rays or beta particles (electrons) have been readily used for excitation of samples for decades and because of their compactness, small dimensions and lack of drift they are often used in portable systems. The typical radioisotopes used are Fe-55, Cd-109 and Am-241, with strengths of up to 40, 20, and 30 mCi, respectively [47]. Their disadvantage is that they usually emit in one or two energy regions useful for the photoelectric process leading to x-ray emission. Therefore, several different sources may be required to excite a wide range of elements as the energy of the source radiation must be greater than the absorption edge of the element to be analyzed. Additionally, the efficiency of excitation decreases if the energy is much higher than the absorption edge. Therefore, one source will be only efficient for a few elements. A further disadvantage, which might be even more important, when designing a mobile, portable XRF system using it outside a controlled laboratory environment, is the safety. The activity or flux from these radioactive sources must be very low. This means that the x-ray intensity from the sample will be also very low. When using such a source with a pin-hole collimating system this problem will be even more drastic.

The utilization of tube excitation is the most common approach in EDXRF and is widely used in PXRF systems as well. The high advantage of such instruments is that they use a low filament voltage to heat the filament wire for emission of electrons. A potential of up to 50 kV or even 60 kV is applied between the filament (cathode) and a target of a pure element (anode) for producing continuous (bremsstrahlung) and characteristic x-rays emitted from the anode.

The tube is under high vacuum, so x-rays have to pass through a window, usually made of beryllium. As mainly the bremsstrahlung is used for the excitation, the background in the spectra is quite high and hence the signal to noise ratio is quite low, which hampers the analysis of trace elements by such systems.

3.1.2. Tube Cooling

Most of the energy produced by the interaction of the accelerated electrons with the target (anode) is heat. The tubes operating in wavelength dispersive x-ray spectrometers are rated at the order of 1-3 kW and must be water cooled. In EDXRF spectrometers however, higher efficiency of the system and therefore lesser decrease in the end excitation intensity allows to employ tubes with lower power as well. They can be only air cooled and are therefore manageable and small enough to be used in portable systems too. Having that in mind, a 50 W maximum power air cooled x-ray tube was chosen for our PXRF system. To make sure that the optimal working temperature of 55°C (measured on the casing of the tube) is not exceeded during longer measurements, an additional fan cooling can be mounted.

3.1.3. Anode Material

The next factor to decide on was the anode material of the tube. For different applications it should be possible to change the x-ray tube, as it is common when working with wavelength dispersive techniques. However, the use of energy dispersive spectrometers has been enhanced by computer control of tube current and voltage as well as primary filter selection. Furthermore, in energy dispersive spectrometers the continuum excitation is utilized more efficiently. Consequently, the choice and efficient utilization of a single x-ray tube is an important decision, when a portable energy dispersive x-ray spectrometer is designed.

As the characteristic lines emitted by the target (anode) material of a x-ray tube have much higher intensities than the continuous spectrum emitted, it is wise to utilize these lines for excitation, whenever possible. Usually a big variety of anode materials is offered nowadays and depending on the applications, one has to select the right material. The principal concern

is to select an anode which has characteristic lines close to, but always of higher energy than the absorption edge energies to be encountered. Table 3.2 summarizes the characteristic line energies for anode materials offered by Oxford Instruments for a 50 W x-ray tube, model XTF5011. It should be kept in mind that none of the characteristic lines from the anode should coincide with the lines of the elements to be determined. The interference of a Compton scatter peak, whose energy can be calculated from *Equation 2-2*, should also be considered. Furthermore, it must be also taken into account that it is difficult to perform determinations of the element of the anode material, especially if the samples have low concentrations of that element.

If one doesn't have any specific needs, a universal tube anode material for general purposes is rhodium. The characteristic lines of Rh can be efficient for excitation of elements with absorption edges up to approximately 15 keV [82], but the excitation efficiency for the K-lines of the transition elements ($Z = 22-30$) is rather low. However, the continuum can be used efficiently in this region. Additionally, the characteristic L-lines of Rhodium at approximately 2.7-3.0 keV can be efficient for excitation of K-lines of low atomic number elements, such as Al, Si, P, and S. Additionally, Rh is very rare in materials used for artifacts and there is no real need to determine it. Therefore, a rhodium anode x-ray tube was chosen for our PXRf system.

<u>Anode Element</u>	<u>Line Energies (keV)</u>	
Cr	5.41	K α
Mo	17.5	K α
	2.29	L α
Rh	20.2	K α
	2.70	L α
Pd	21.2	K α
	2.83	L α
Ag	22.1	K α
	2.98	K α
W	8.40	L α

Tab. 3.2: Characteristic energies of the x-ray tube anode materials commercially offered by Oxford Instruments for their line of 50 W packaged x-ray tubes.

3.1.4. High Voltage Power Supply

For delivering a voltage of 50 kV with a maximum current of 1.0 mA the Matsusada HXR-505-50-01 High Voltage Generator was selected. It was highly recommended by Oxford Instruments (manufacturer of the chosen x-ray tube) and its function in connection with the x-ray source has been flawless. Most of the x-ray tube failures occur due to a lack of adequate filament current protection. Therefore, this power supply has been carefully matched to the existing x-ray source to provide necessary filament protection by utilizing an integrated filament supply in conjunction with matched filament over-current protection. That way, the maximum x-ray tube life can be assured.

In order to both digitally control and monitor the operating conditions of the x-ray tube during the measurements (accelerating voltage and filament current) a special interface with an analog/digital and digital/analog converter was built. It is operated using a self-developed software based on the LabVIEW development environment (see Chapter 3.7.). The complete constructional documentation and a command manual for the High Voltage Generator Interface can be found in Appendix C.

3.2. Focusing/Collimating the X-Rays

Use of a conventional XRF for exact qualitative and quantitative analysis is usually severely hampered by the fact that the irradiated area is usually large. This is normally not a problem when analyzing powders, but this prevents investigations of details of decorations, distinct features etc. Also, even for smaller homogeneous objects (such as coins), which might be analyzed as a whole in a conventional XRF instrument, the use of a small beam instrument offers advantages as only a small area of the (altered) surface needs to be removed in order to expose the underlying original material. Since many objects of artistic, historical and/or archaeological nature are often fairly large and bulky (e.g. statues, oil paintings, vases, treasury objects), an instrumentation is very useful that can accommodate the objects of various sizes and shapes and can function properly in air. The use of smaller x-ray beams can circumvent some of these limitations. It is also useful to analyze an object at various locations in order to

verify that all parts of the object are made of the same material and to investigate the homogeneity of the materials used. Furthermore, conventional XRF on curved or non-flat surfaces can lead to errors in quantification, especially for metallic materials [83]. With a beam collimated to a small diameter (approximately 1 mm in diameter), it is in general easier to select locations on an object which resemble more closely to the ideal, flat and polished surface normally required for reproducible quantitative measurements.

3.2.1. Capillary Optics

One option to focus an x-ray beam is to use capillary optics (cylinder moncapillaries, tapered moncapillaries, polycapillaries) [25]. Employment of such a system provides a beam radius on a micrometer scale and a number of laboratory-built instruments with this feature are already available [84-86]. Recently, a compact and moveable micro-XRF spectrometer has been designed and built as well [87]. By employing tapered moncapillaries higher flux densities can be achieved [86], meaning that even with a beam size of microscopic dimensions the excitation intensities can be strong enough for analytical purposes. But for most applications the collimation to such dimensions is not necessary. On the contrary, it is sometimes even undesirable, e.g. when analyzing objects where an average composition is required, but the elemental constituents within the sample are clustered and not homogeneously distributed. Therefore, only a great number of measurements, yielding a statistical correction, can produce an acceptable result. In that case, a beam collimated down to a diameter of 1-2 mm will be a better choice. Secondly, such a fine micro-beam requires a sensitive system for a micro-adjustment of the sample, ensuring the sample is in focus and the correct measurement geometry is retained throughout the measurement. Therefore, for most applications of a truly portable XRF system, such collimating devices are not necessarily appropriate; in some cases they may even be disadvantageous.

3.2.2. Pin-Hole Collimation

The most straight-forward and easiest way to obtain a 1-2 mm small beam, is to put a pin-hole of a required diameter in the optical path of the x-rays. Besides being low priced (in compari-

son with polycapillary optics by a factor of 100), such a system is more robust, yielding a much lower degree of necessary maintenance, hence, making it very appropriate for use with a PXRF for the application of field measurements under non-laboratory conditions.

However, when designing a pin-hole collimator, one has to keep in mind that this solution is, of course, associated with a great loss of the primary intensity of the beam. When leaving the anode, x-ray beams disperse in a sphere, and only a very small amount reaches the pin-hole exit of the collimator. Furthermore, the intensity of x-rays striking the sample is inversely proportional to the square of the distance between the x-ray tube anode and the sample. The same inverse square law applies to the sample-detector distance. To overcome this intensity loss, it is very important that, besides having a powerful and sufficient x-ray excitation source, the pin-hole collimator has to be carefully constructed.

The difficulty of obtaining x-rays with satisfactory intensity after they have been collimated has always been a great problem. A lot of work on behavior of x-rays passing through such a pin-hole has been conducted already [88] and the optical characteristics such as divergency, beam radius and spatial resolution under varying instrument parameters have been analyzed. As already mentioned, only a fractional amount of the initial photon flux passes through such a collimator and when using that kind of a system one must accept a lower count rate. To compensate for the loss of the intensity due to the small opening on the collimator the more powerful, water-cooled x-ray tubes (in kilowatt range) could be used [89, 90]. However, as already discussed in Chapter 3.1.2, the use of water-cooled tubes is not acceptable for a portable XRF system. In order to obtain still enough intensity for analytical purposes using a tube with a given maximum power, the radius of the pin-hole must not be too small and the whole system must have a geometry that allows positioning of a sample as close to the x-ray source and the detector as possible.

Because of its ability to be handled and shaped easily, and at the same time of its rather high attenuation coefficient (safety concern), brass was chosen as a main material for the construction of the collimator (Fig. 3.1). The collimator cylinder is mounted on a convex brass support which, in turn, is firmly attached to the side exit window of the x-ray tube (Fig. 3.2). In order to enable easy adjustment and optimum collimator alignment, thus ensuring high x-ray intensities, the radius center of the convex support curvature is located in the focal point of the

anode. During the alignment the four screws holding the collimator in place are left loose to allow slight adjustment movement of the cylinder and when the optimal photon flux is reached they are slowly tightened to prevent misalignment in the future.

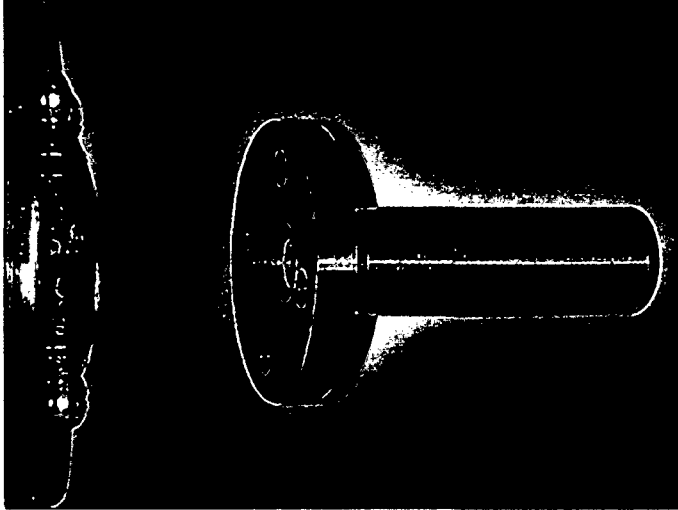


Fig. 3.1: The convex brass collimator support and the collimator, before being mounted on the x-ray tube.

A system of 2 pin-holes with different diameters (4 and 1.5 mm) was constructed inside the collimator tube in order to avoid interactions of the primary beam with the inner side of the collimator, and hence secondary radiation from the cylinder material itself. In addition, the inside of the collimator tube was coated with a 1 mm thick aluminum foil, which, beside Al, contains mostly light elements [e.g. Mg, Si as minor components (traces)], whose characteristic radiation does not affect the measurements in great extent. Between the aluminum foil and the brass tube an additional 1 mm thick lead cylinder is mounted for safety reasons. From *Equation (2-3)* it can be calculated that the maximum transmission through a 1 mm thick lead film (cross section for lead at 50 keV is $\sigma = 2701$ [barns/Atom][90]) is only 0.014 % of the initial value, which is quite sufficient.

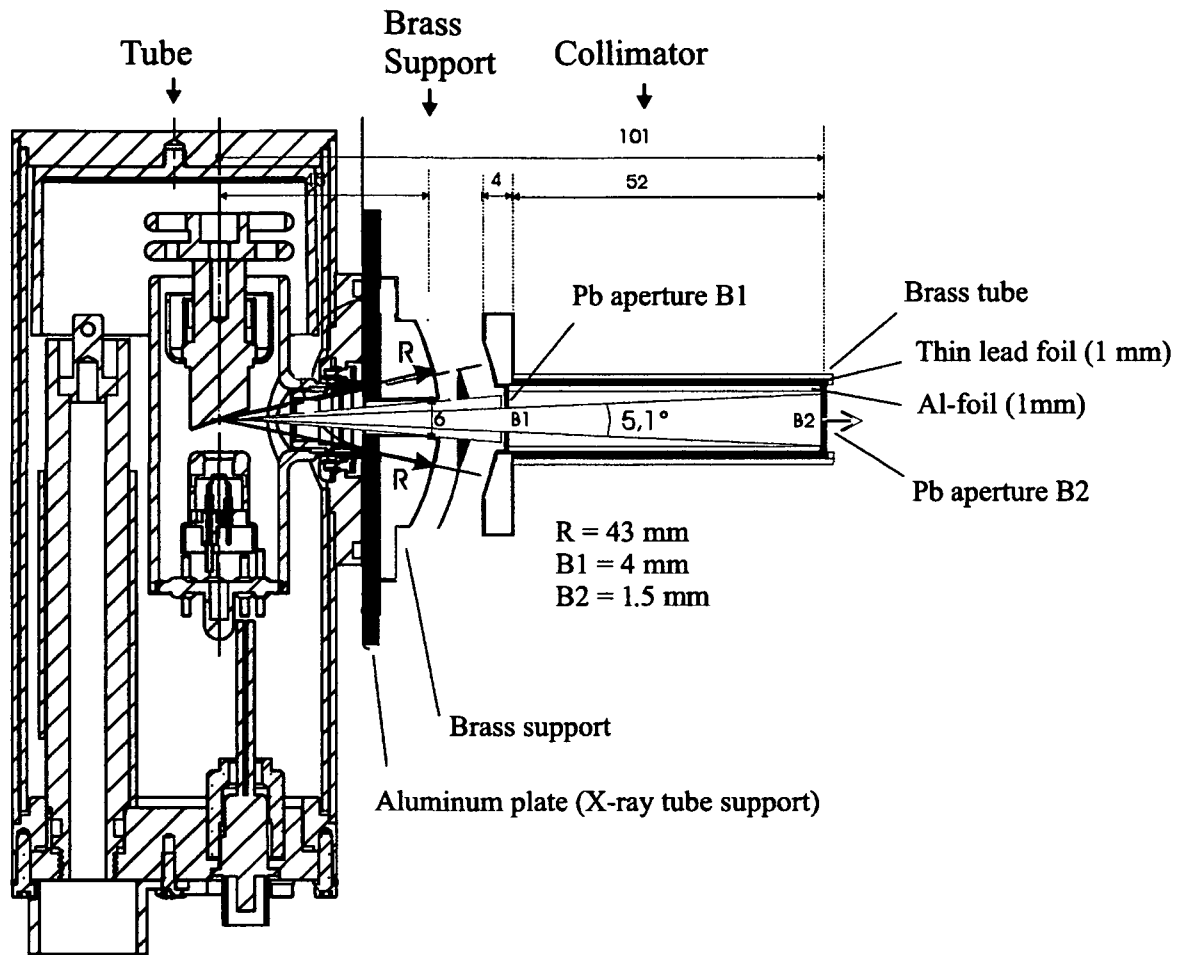


Fig. 3.2: Schematic drawing of a cross section of the x-ray tube and the collimator showing the different parts in the cylinder.

The final aperture defining the radiation beam diameter was thus 1.5 mm, yielding a radiation spot on a sample around 2 mm. Detailed test measurements determining this value are described in Chapter 4.

3.3. Pointing Device (Alignment System)

When designing and constructing an alignment system, one should keep in mind that it should serve two purposes. It should not solely assist in locating and defining a measuring point, but it should also assure the constant and correct distance from the sample to the x-ray tube and the detector is maintained throughout all the measurements. The importance of this lays in the

fact that the uncertainties in the distance of the sample from the designed focal plane are raised to the fourth power in detected intensity. For a system with a tube-sample and sample-detector distance of 2 cm, a variation of 0.2 mm results in a variation of approximately 0.4% in the measured intensity of the sample.

Having that in mind, two laser pointers were mounted on each side of the collimator and were positioned in such a way that the intersection point of the two laser beams coincides with the cross-point of the x-ray beam and the detector-axis (Fig. 3.5 and Fig. 3.7).

The lasers utilize a 670 nm radiation (red light), with a maximum power of only 1 mW. Additionally to the rather low power, a pin-hole with an aperture of 0.5 mm was placed in the beam path of each laser in order to refine additionally the beam and further minimize the danger of destructiveness to the sample during alignment of a PXRF prior to the measurement.

3.4. Detector

The simultaneous identification of the elements in a sample using x-ray spectroscopy depends on resolving the spectral lines emitted by various elements. This process requires some form of energy sorting or wavelength dispersing device. In case of wavelength dispersive x-ray spectrometry, for this purpose some sort of mechanical devices, such as analyzing crystals, are required. Energy dispersive systems, however, are based upon the ability of the detector to create signals proportional to the x-ray photon energy, so no mechanical gadgets are required. Solid-state detectors are qualified for detecting and analyzing the x-ray radiation. Their operation is based on the interaction processes of the electromagnetic radiation with matter. The incoming x-rays create charges (electrons and holes) in the semiconductor crystal, which are separated by an applied bias field. The electrons and holes are attracted to the opposite surface and constitute an electrical pulse in response to the ionizing radiation.

3.4.1. Compact Detectors

At the moment there are several types of detectors commercially available, which are being applied in EDXRF applications [35, 92, 93, 94]. They may have different cooling systems, significantly different energy resolutions, and various pulse throughput capabilities. For the use with a portable system, cooling mechanism based on liquid nitrogen is not appropriate, so a system based on thermoelectrical (Peltier) cooling is a prerequisite. The Si-drift chamber detector (SDD) and the Si-PIN diode both feature LN_2 -free operation and are available as compact, light-weight devices. However, they employ different charge collection principles and show significant differences with respect to maximum count rates and energy resolution.

The Si-PIN detectors were developed during recent years and are characterized by a rather small active area (in the order of $5\text{-}8\text{ mm}^2$) consisting of a $300\text{ }\mu\text{m}$ thick Si-diode, cooled with a Peltier cell. Due to the reduced thickness of the active Si-diode the efficiency of this detector type rapidly decreases beyond $25\text{-}30\text{ keV}$ [41]. At 5.9 keV its energy resolution is about $200\text{-}250\text{ eV}$.

3.4.2. Principles and Advantages of SDD

The functioning of a SDD is based on the general principle of the solid-state detectors. The detector uses a silicon crystal composed of several areas doped in different ways (n- or p-type). Reverse-bias voltage is applied forming a central region absent of free charge within the crystal. This region is also called the depletion region. When a charged particle or photon enters this region, it interacts with the semiconducting material to form electron-hole pairs in a cascade process. The number of created charge carriers can be calculated and it is dependent on the energy of pair formation. This is the energy, which is needed to produce one electron-hole pair and is affected slightly by the semiconductor temperature T and the energy of the absorbed photon E_γ . For silicon (at $T \approx 300\text{ K}$ and $E_\gamma \approx 1\text{ keV}$) it lies at around 3.65 eV . The number of created charge carriers is proportional to the energy deposited by the incident particle in the depletion region. For example, an x-ray photon with energy of 8 keV ($\text{Cu K}\alpha$) originates around 2190 electrons.

Silicon Drift Detector (SDD) is characterized by a specific design of the contact areas. It is based on a principle of sideward depletion, a novel feature introduced by Gatti and Rehak in 1984 [42]. It consists of a volume of fully depleted silicon in which an electric field with a strong component parallel to the surface drives signal electrons towards a small sized collecting anode. The basic idea is that a large semiconductor area (e.g. n-silicon wafer) can be entirely depleted by an n^+ -junction, when a negative voltage is applied to two big p^+ -junctions on upper and lower side of the wafer. In an advanced SDD design optimized for applications in x-ray spectroscopy, the concentric ring-shaped p^+ strip system which generates the drift field and the collecting anode (n^+) in the center are placed on one side of the structure, while the opposite surface is covered by a non-structured p^+ -junction acting as homogeneous radiation entrance window, thus ensuring homogeneous sensitivity over the whole detector area (Fig. 3.3)[44, 95]. The electrons drift towards the area of positive potential, meaning towards the anode (voltage difference ≈ 100 V), with the drift speed between 10^3 and 10^4 m/s. As the device is fully depleted, the whole thickness of $300\text{ }\mu\text{m}$ is sensitive to the absorption of x-rays.

Due to various engineering reasons, the thickness of the detector chip for both SDD and Si-PIN diode detector is usually limited to about $300\text{ }\mu\text{m}$. This leads to a low detection efficiency in the high-energy range (due to the decreasing probability for a detector-photon interaction) and an increased background in the low-energy range (due to the increasing recombination probability for the charge carriers near the p^+ -doped layer). Accordingly, both detector types feature similar detection efficiencies in the low ($< 15\text{ keV}$) and high ($> 15\text{ keV}$) energy ranges. The quantum efficiency of these detection systems is greater than 90% in the range between 1.5 and 10 keV [45], and $> 50\%$ at 20 keV .

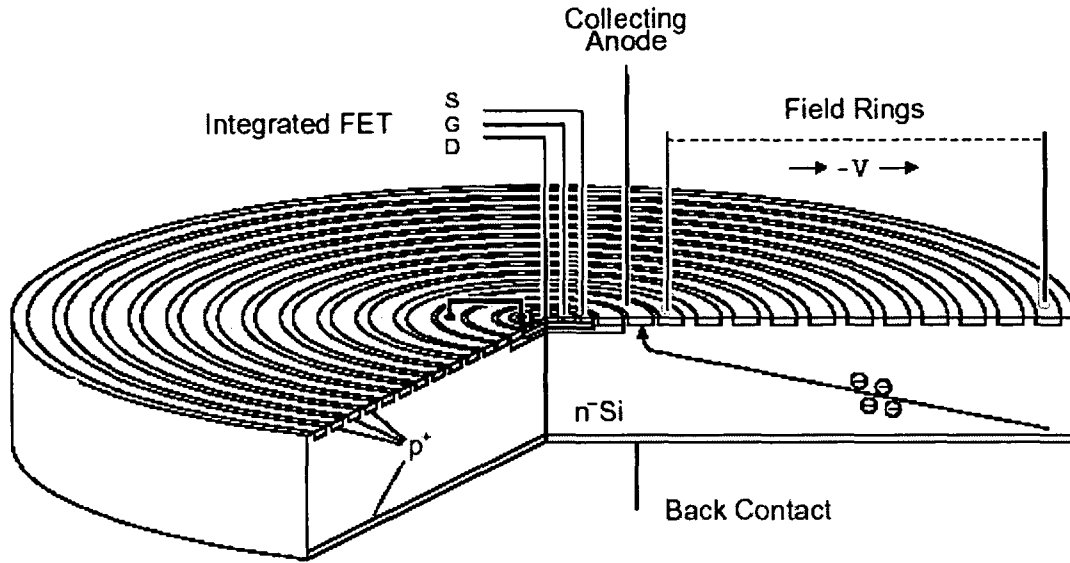


Fig. 3.3: A schematic drawing of a cylindrical Silicon Drift Detector [44].

The outstanding property of this type of detector is the extremely small value of the anode capacitance, which is practically independent of the active area. This feature allows to gain higher energy resolution at shorter shaping times compared to conventional photodiodes and Si(Li)-detectors. Consequently, the SDDs can be operated at exceptionally high count rates, allowing spectroscopic measurements with count rates up to 10^6 cps [44]. Due to the sophisticated process technology used during the manufacturing of the SDDs the leakage current level is so low that the drift detector can be operated with good energy resolution already at room temperature (FWHM < 200 eV at 5.9 keV). With additional moderate cooling by a single stage Peltier element the SDD's energy resolution reaches values FWHM < 160 eV at 5.9 keV, which can be already compared to that of a Si(Li) or HPGe detectors requiring expensive and inconvenient liquid nitrogen cooling.

A useful and detailed comparison of these two detector systems (PIN-diode and SDD) regarding their maximum output range has been reported by Bichlmeier et al. in 2001 [87]. They found that the important difference between the two devices is the amplifier shaping time required to obtain acceptable resolution. In order to achieve a 210 eV resolution at 5.9 keV using the PIN-diode, a 20 μ s shaping time is required; the drift chamber achieves a 160 eV resolution with a 5 μ s shaping time. For comparison, a tested Si(Li) detector offered a 180 eV

resolution at 12 μ s time. The long shaping time causes the PIN-diode to start showing a non-linear response from 2.200 cps onwards, whereas for the drift chamber a linear response is maintained even at 25.000 cps net count rate. Therefore, since the SDD can handle higher count rates easily, a further improvement of the minimum detection level (MDL) can be reached if the tube current is increased to the maximum settings. This is often not possible, however, for the PIN-diode, which is in its non-linear region already at count rates just above 2.200 cps.

Due to the above mentioned advantageous features of a SDD, namely LN_2 -free operation and cooling with a single Peltier element as well as energy resolutions in the order of 150-160 eV FWHM at 5.9 keV, this detection system appears ideal for portable high-resolution XRF spectrometers. For the portable XRF described in this thesis an XFlash Detector (Series 1000) from Röntec, Berlin, was chosen (Fig. 3.4), with a nominal energy resolution of < 150 eV FWHM at 1 kcps for a Mn K α line (5.9 keV).

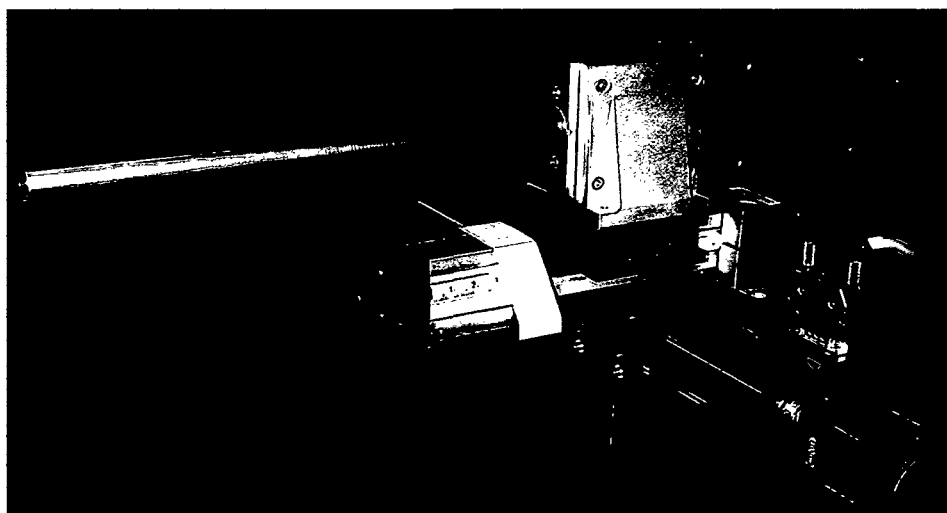


Fig. 3.4: XFlash Detector (Röntec, Berlin) used in the PXRF. The detector is mounted here on a movable micro-stage during test measurements.

3.5. Assembly of the Main Components

PXRF measurement head showing the arrangement of the main components is illustrated in Fig. 3.5. The collimator of the x-ray source is placed perpendicular to the investigated object/specimen, and the detector is positioned under 45° to the primary x-ray radiation. As mentioned in Chapter 3.3, the beam intersection of the two pointing lasers coincides with the cross-point of the x-ray beam and the detector-axis. That way the exact position of the measuring point can be determined, as well as the exact distance between the x-ray source and the sample.

The measuring head is fixed on an extension arm, which can be stabilized on a tripod using a counter weight, as shown in the Fig. 3.6 during a measurement in the Gallery of Academy of Fine Arts in Vienna. A set of different extensions and joints enables to position the measuring head in virtually every direction (see Chapter 5), according to the different shapes and sizes of objects, which are in the field of archaeometry often very fragile, bulky and can not be moved or turned around easily.

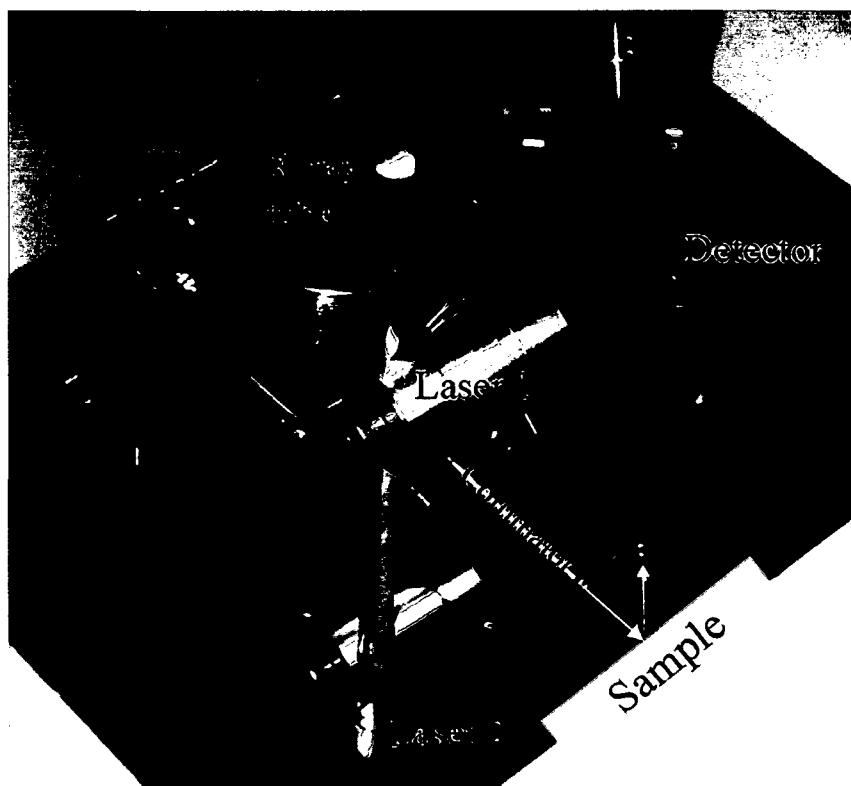


Fig. 3.5: Component arrangement on the measurement head of the PXRF.

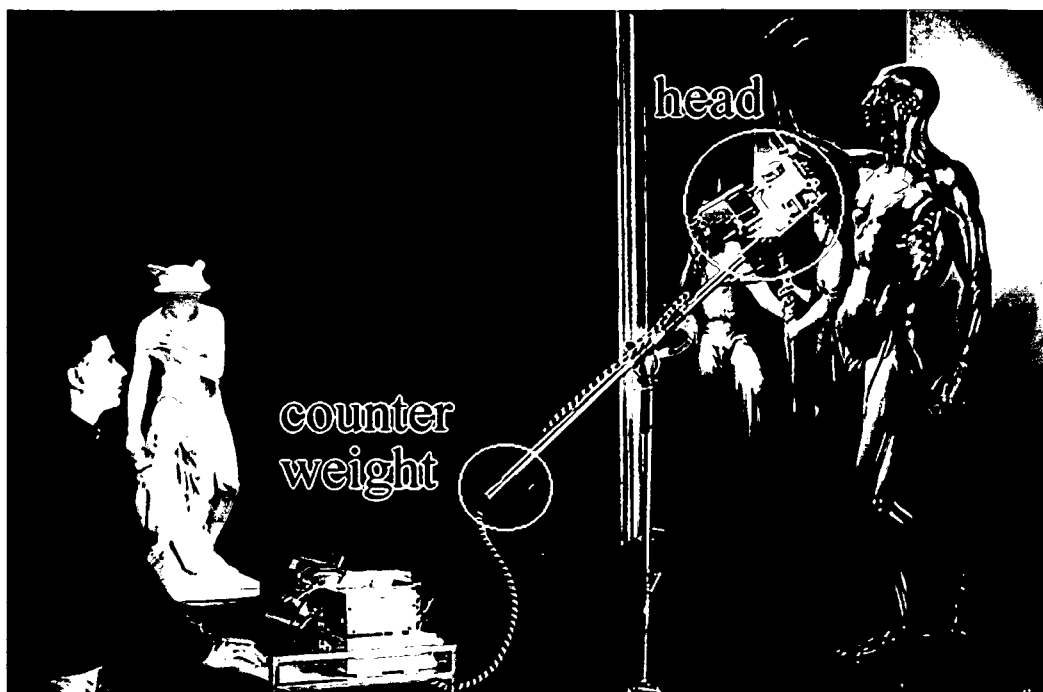


Figure 3.6: Portable XRF during a measurement in the Gallery of the Academy of Fine Arts in Vienna.

A schematic diagram of the entire system is shown in Fig. 3.7. Sufficient cable length between the measurement head and the control electronics (3 m) assures safe distance between the operator and the x-ray source, and therefore, safe utilization of the PXRF.

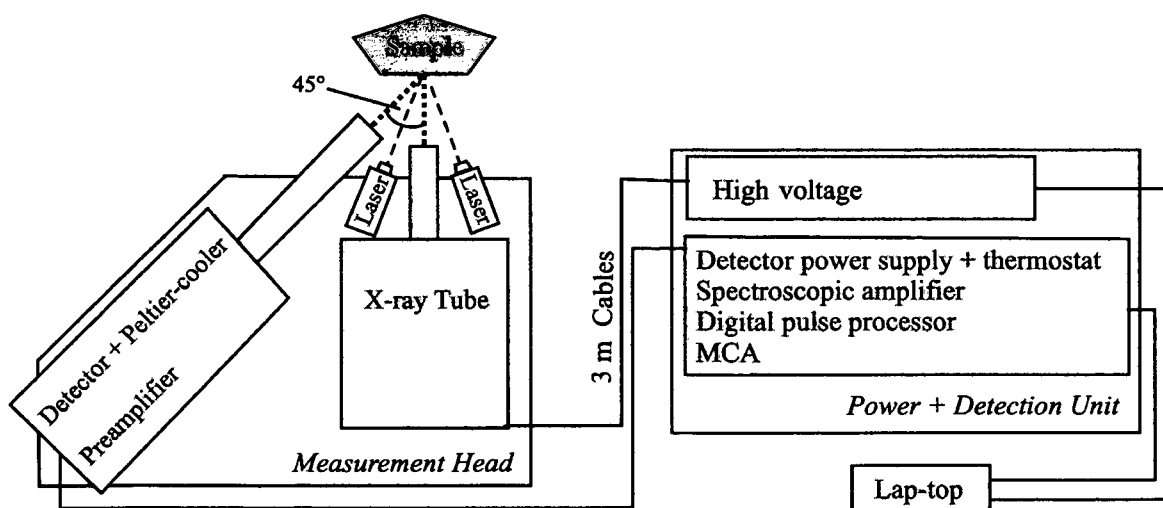


Fig. 3.7: Schematic illustration of the entire portable XRF system.

3.6. Analyzing Electronics (Spectrometer)

During EDXRF analysis x-rays emitted by the sample are absorbed by a detector, which converts these incident x-rays into electronic pulses. Therefore, the x-ray spectrum of the sample is obtained by processing the energy distribution of x-ray photons which enter the detector.

By entering the detector, a photon causes photoionization and produces a charge proportional to the photon energy. To convert this charge to a data point in the spectrum, numerous electrical sequences must take place. The amplitudes of these electronic pulses are proportional to the energies of the corresponding x-rays. Pulses are then processed and sorted according to their energies and the entire range is divided into a certain number of intervals (e.g. 4096). Those pulses falling within each interval are counted in a multichannel analyzer. That means that an EDXRF spectrum is actually a histogram of the number of counts of those (4096) channels. Usually, the channel number is converted to energy units by calibration.

When choosing a right spectrometer for a given application two important issues have to be kept in mind. The analyzing electronics has to be modified and adopted for faultless cooperation with a given detection system, and an appropriate pulse processor, yielding adequate pulse throughputs for the planned applications, has to be chosen. To meet the first demand a Röntec Max Spectrometer was decided on, which was custom-tailored for ideal performance with the present Röntec XFlash Detector.

3.6.1. Signal Shaping Time and Energy Resolution Dependency

Pulse shaping is performed by the pulse processor to improve signal-to-noise ratio in the system, and to optimize the resolution. The right selection of the pulse shaping time should be optimized to the expected x-ray count rate. The more time is spent for measuring the pulse from the detector, the more precise is the measurement, and the better is the resolution. And vice-versa, very fast processors for high count rate application can be chosen, which yields to a lower energy resolution.

During the development of the PXRF two different configurations of the detecting unit were tested. The first one employed a signal processing unit with a signal shaping time of 0.21 μ s (Gauss approximation), maximum pulse throughput of 275 kcps, with a maximum impulse density of 700 kcps, and an energy resolution of under 220 eV at 250 kcps FWHM for Mn K α . The second measuring system included a signal processor with a signal shaping time of 1.0 μ s (Gauss approximation), maximum pulse throughput of 60 kcps, with a maximum impulse density of 150 kcps, and an energy resolution of under 150 eV at 1 kcps FWHM for Mn K α .

The question was, of course, which of the two pulse processors is more suitable for applications that are planned to be carried out with this instrument. The first processor provided very high maximum possible count rates, but only rather average energy resolution of 220 eV. The second one provided somewhat lower maximum counting rates, but the improvement of the energy resolution down to 150 eV was a significant improvement. The decision in such a case is always a compromise, sacrificing the least relevant concern for a given system. Because it was clear that we needed the best possible energy resolution of a detection system, it was opted for the slower processing, higher resolution processor. But prior to final decision, trial measurements had to be carried out to make sure the count rate in a standard operating mode wouldn't be too high for this pulse processor, thus leading to detector saturation, pileup, and consequently to a loss of valuable spectroscopic information. Measurement tests employed on Pb-sample indicated, however, that even for lead, a substance yielding the highest intensity of secondary fluorescent radiation for a relevant energy range, the maximum count rates (up to 20 kcps) were still well below the upper limit of the processor (60 kcps). The main reason for this rather low count rate is an intensity decrease of the primary excitation x-ray beam, which is conditioned, on one hand, by a functional nature of the employed pin-hole collimator, and, on the other hand, by limitation of the maximum x-ray tube power to 50 W, imposed by its portability requirements. Accordingly, the XSVP 60 pulse processor was chosen and installed in the PXRF, yielding nominal energy resolution below 150 eV FWHM at 1 kcps for Mn K α line (5.9 keV).

3.7. Communication between Components, Data Acquisition, Evaluation, and Presentation

A self developed software package based on LabVIEW development environment of National Instruments controls and manages the communication between the particular system components and their functions. Furthermore, using the same software the spectra are acquired, calibrated (gain/offset correction) and evaluated qualitatively. The complete user manual can be found in Appendix A.

3.7.1. Development Software LabVIEW

National Instruments LabVIEW (Lab Virtual Instrument Engineering Workbench) is a graphical development environment designed specifically for building test and measurement applications. LabVIEW is also a full-featured graphical programming language with all the standard features of a general purpose programming environment. It delivers a powerful graphical development environment for signal acquisition, measurement analysis, and data presentation giving the flexibility of a programming language without the complexity of traditional development tools. Due to its structural functionality that can be expected in a powerful programming language, such as data structures, looping structures, and an event handler, it compares well with other strong text-based programming languages such as Visual Basic and Visual C++.

3.7.2. Component Control and Acquisition

LabVIEW is an open environment and its design made interfacing with individual PXRF hardware components rather straightforward. Using LabVIEW it is possible to digitally control the x-ray source voltage and current conditions, detector power supply and temperature control as well as the operation of the whole data acquisition system. With the help of the built-in tools, LabVIEW provides great help for data visualization, user interface design, and

data management. Additionally, due to the software connectivity, the spectra can be subsequently evaluated quantitatively using the spectrum processing package WinAXIL (from Canberra Eurisys, Belgium), which also includes a module for quantization by means of the fundamental parameter method [96].

4. Instrument Operation and Test Measurements

Beside having chosen the adequate single system components and having them assembled in the way so that they function properly and effectively as a unit, it is also important that the x-ray spectrometric theory is well understood and the reasoning for pros and cons of the method application for a given investigation is correctly judged. All too often the poor functioning of equipment is blamed for faulty investigation results, whereas the real problems may lie either in the erroneous preparation of the sample material or/and in the poor judgment and false selection of the measurement conditions. This chapter covers some of the basic application principles and selection of efficient operating conditions, gives guidelines for utilization of the PXRF for specific problems, and describes the tests done in order to determine the instrument's performance. Furthermore, it gives some basic maintenance suggestions to keep the system working on the same level for the years to come.

4.1. Selection of Efficient Operating Conditions

X-ray spectrometric theory is relatively simple and allows precise prediction of the optimum excitation conditions when only one single element is present. However, the ability of the PXRF system to simultaneously analyze multi-elemental samples complicates the selection of optimum conditions because of the factors which must be considered for each of the elements. In that case, just like with other spectroscopic techniques, compromises must be made. During the measurements there are too many varieties of sample and element mixtures encountered to establish strict rules and conditions of x-ray tube operation. However, some guidelines are possible and will be discussed here. It should be noted, that due to the difficulty to consider all factors, the experimentation with different instrument settings is encouraged and no setting should be regarded to as ideal, if several different samples are investigated. The only time, when this is encouraged, is when acquiring reference spectra from reference samples. In that case, to obtain accurate results, the reference spectra for spectrum fitting must be obtained under the same conditions as those for the analysis.

4.1.1. X-Ray Tube Operating Voltage

The initial selection of instrumental conditions can follow a logical sequence of decisions. Firstly, the x-ray photon energy used to excite a sample, whether from a characteristic line of the anode element or from the continuum, must be greater than the highest absorption edge energy to be excited. Because usually materials containing several different elements are investigated, a wide range of absorption edges may be encountered using a given excitation spectrum. In that case, the excitation efficiency for some elements will be greater than that for others. However, the continuum maximum should not be set too close to the highest absorption edge which is to be excited. As a rule of thumb, the operating voltage of the x-ray tube should be set approximately 5 kV above the highest absorption edge to be excited [82]. Contributing to the background of the corresponding emission line there will be a component of Compton scatter from the continuum, which should be also taken into account.

An issue which should be also kept in mind is which x-ray lines are to be used for determination. As a general rule, K-lines should be used which have K absorption edge energy up to a few keV below the characteristic line of the x-ray tube anode element, in this case of Rhodium (20.2 keV for Rh $K\alpha$). That means, for operation of the Rh x-ray tube, one should utilize the K-lines of the elements up to an atomic number of approximately 40 (Zr, $K_{\text{absorption}} = 18.9$ keV). Beside using the Rh characteristic lines the continuum may be used for excitation as well, if the voltage set to the tube is sufficiently high to place the continuum maximum at an energy higher than the absorption edge. In that case a background filter is very helpful. However, the observed peaks will lie on a continuum background and reduce the signal to noise ratio. For a 50 kV x-ray tube, absorption edges as high as 30 keV ($Z = 51$, Sb, $K_{\text{absorption}} = 30.5$ keV) may be used provided the element is present in sufficient concentration. A list of K and L absorption edges for a number of elements can be found in the Appendix B.

The elements above the atomic number 51 (Sb) are generally determined by using the L-lines of their x-ray spectra. In order to excite all L-lines, the incident excitation energy must be greater than the L_1 absorption edge. Because of practical reasons, the energy of the L-lines must be greater than approximately 2 keV. This means that elements with an atomic number higher than 40 (Zr) can be determined using their L-lines spectra. However, at such low x-ray energies, absorption of the x-ray in air as well as low fluorescent yield in the L emission in this region, require a high concentration of the element to be determined. Further problems

are the difficulties with overlap of some K-lines of the low atomic number elements in that region, which lie rather close to each other. For example, the L-lines of zirconium overlap with the K-lines of phosphorus. Another example is the K-line of sulphur, which overlaps with the L-lines of molybdenum, and at the same time with the M-lines of lead at approximately 2.3 keV. These problems must be considered and may give false indications. However, after a more careful analysis using data processing software they are resolved to a great deal.

That means that, when investigating transition elements in a mixed sample which contains light elements as well, and when determining them using both K- and L-lines, the following should be kept in mind. For as long as it is practically possible, one should try to excite and compare the higher energetic K-lines of the transition elements, because their lower energy L-lines may be affected by the above mentioned factors, thus altering subsequently the end result.

The next step to be undertaken is to decide whether all analyte constituents in the sample can be effectively excited, and therefore determined, using only one instrumental setting. Even though the multielement capabilities of an EDXRF system are powerful, one has to keep in mind that a measurement with only one set of instrumental parameters is not always sufficient. A good example when an investigation needs more than one condition is when an analyzed sample is a mixture of both light and transition elements. In that case the transition elements are best determined by excitation using the K-lines of Rh anode, and the low atomic number elements with the L-lines, or a properly adjusted continuum (preferably using a background filter). Because the PXRF system offers digital computer control of the instrumental parameters, it is easy to change conditions. Some sources [82] suggest that, when changing instrumental parameters, all the samples should be analyzed under one set of conditions, and only then reanalyzed using the alternate set. However, first hand experience using PXRF showed that it is better to change conditions while still being on the same sample, in order to assure that the selected area remains the same, and the constituents ratio in the examined sample volume is unchanged.

4.1.2. X-Ray Tube Operating Current

The adjustment of the x-ray tube operating voltage will have an effect on the efficiency of the excitation of each element in the sample as well as on the x-ray photon flux from the tube. On the other hand, the tube current will affect the flux only. Therefore, once the operating conditions regarding the accelerating voltage have been set, it is important to adjust the tube current in a way that the system processes enough counts effectively. With the older generation of detectors employing slower pulse processors rates (Si(Li), HP(Ge), Si PIN-diode,...) it was important not to excite the sample too much and to keep the dead time below, or near 50%. With the SDD utilizing fast processing electronics (capable of count rates of 100 kcps and more), this problem doesn't occur any more for most of the applications. Therefore, the tube current adjustment can be set freely to the highest settings required to get efficient peak readings, without having to worry about detector saturation and pileup effects.

As already mentioned at the beginning of this section, these guidelines should only be used for initial selection of operating conditions. The final instrument parameters yielding the best spectroscopic results will consequently be reached by experimenting and comparing the obtained results. Furthermore, they are interactive, meaning that change in one parameter will most likely influence the adjustment of another. For example, a decrease in the tube voltage may require an increase in the tube current. Additionally, subjective factors, such as a special interest in one of the constituents in a sample, may further impose a change in the conditions and alter the guidelines, in order to enhance the x-ray intensities from that specific element.

4.2. Component Tests

4.2.1. Stability Tests

One of the prerequisites for precise and reproducible measurements is a stable and predictable functioning of the system over a prolonged time of use. For that purpose, both x-ray source and the detector were tested by carrying out eight successive measurements of a reference sample, under same excitation conditions, and with a measurement time of 200 s per measurement. The sample was a ÖGUSSA standard with Cu and Ag as constituents (50/50). The applied voltage and current were 35 kV and 0.6 mA, respectively. In order to confirm fault-

less operation of both components, an additional, independent detection system was simultaneously employed during the test measurements. The experimental set up is shown in Fig. 4.1. In case the system would show some irregularities and instabilities during operation, with help of the second detector it would be possible to undoubtedly distinguish the faulty component.

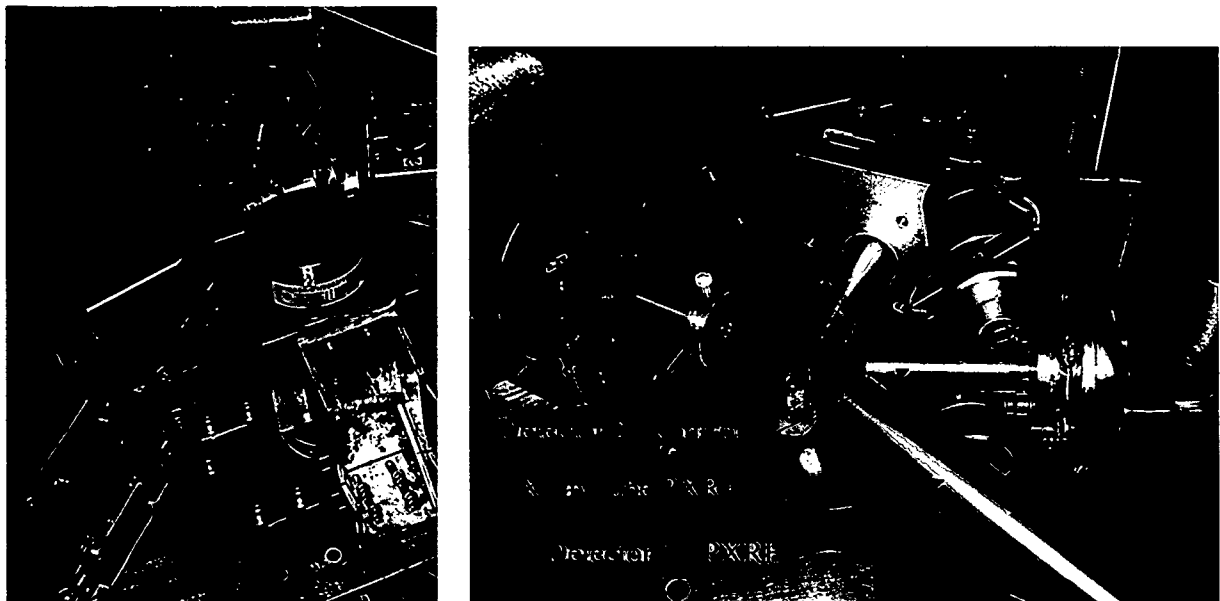


Fig. 4.1: Experimental set up during the stability measurements to determine the proper functioning of the x-ray source and the detector over a prolonged period of time (40 min). Two independent detectors, operated by two different processing units, were employed to monitor the functioning of components.

When directly compared, the spectra of all eight measurements showed similar intensity values for both constituents (Fig. 4.2). The 8 measurements were carried out in 5-minute cycles, thus investigating performance of the system over a period of 40 minutes.

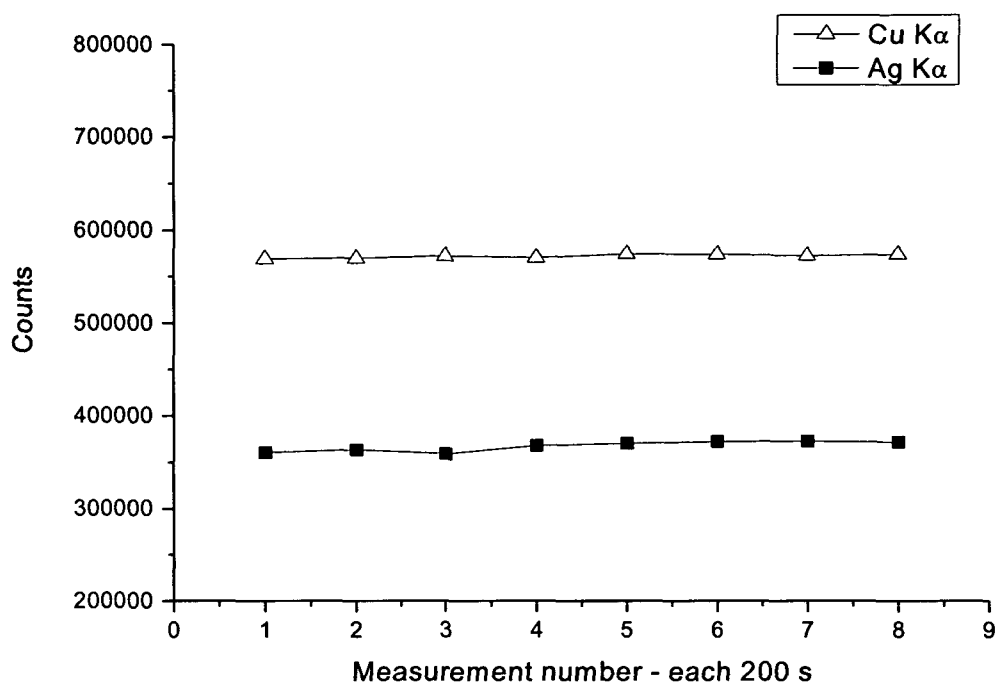


Fig. 4.2: Stability tests of 8 consecutive 200 s measurements of a Cu/Ag reference sample, performed over a period of 40 minutes.

4.2.2. Rh-Tube Excitation Spectrum Energy Distribution

As already mentioned in Chapter 2, the excitation of a characteristic line of an element succeeds the best if the excitation energy is just above the absorption edge of a given element. Therefore, in order to apply the XRF method most efficiently, it is important to know the energy distribution of the excitation spectrum. For that purpose the primary radiation exiting the x-ray tube was measured (Fig. 4.3) and the alternating tube voltage yielding different energy distribution spectra was investigated (Fig 4.4).

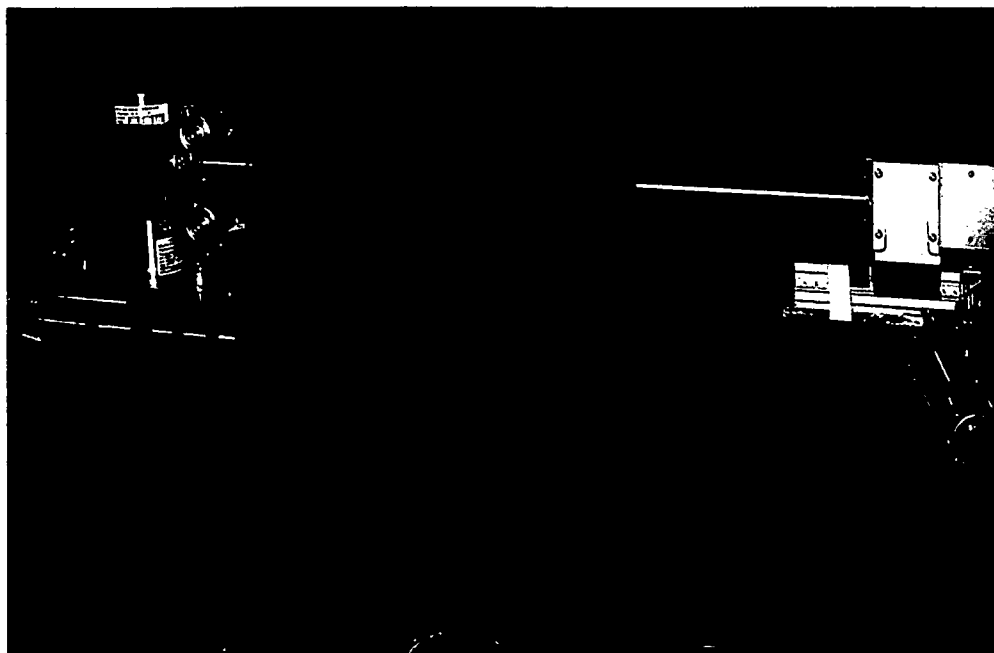


Figure 4.3: Experimental set up during determination of the primary radiation energy distribution. The SDD is set directly in the path of the primary x-rays exiting the collimator.

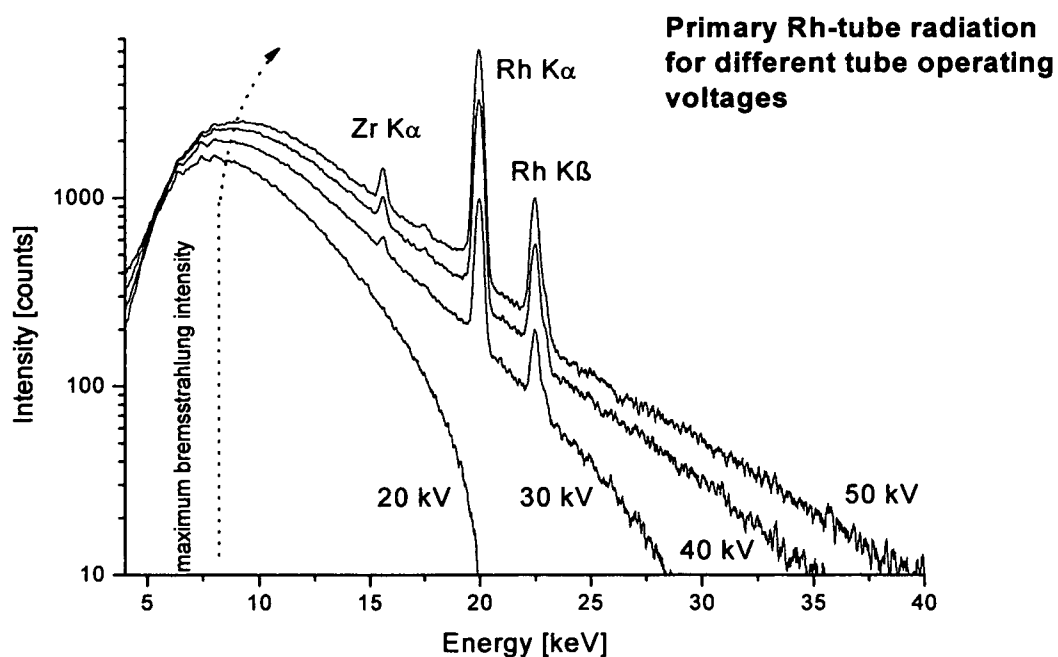


Figure 4.4: Energy distribution of the primary radiation spectra for excitation tube voltages of 20, 30, 40, and 50 kV. With the increasing accelerating voltage the continuum maximum shifts slightly towards higher energies (from 8 keV at 20 kV to 9.3 keV at 50 kV). The peak at 15.7 keV corresponding to a zirconium K α line, stems from the zirconium collimator on the detector entrance window.

As mentioned already in Chapter 3, when investigating samples, which consist of elements having various atomic numbers, both the continuum from the x-ray tube (with a maximum at around 9 keV), and the characteristic Rh-lines (20.2 keV and 22.7 keV) can be utilized effectively for excitation (Figure 4.4). The increasing acceleration voltage in the tube delivers increasing bremsstrahlung yield, shifting slightly its maximum towards higher energies. For excitation using a tube operating voltage below ca. 35 kV the highest photon intensity (cps) is obtained at the continuum maximum at around 9 keV, whereas for accelerating voltages above ca. 35 kV the highest photon intensity is reached at the energy of the characteristic Rh-line (20.2 keV).

4.2.3. Beam Diameter – Measurements with a Cu-Wire and Micro-Stage

In order to determine the exact diameter of the x-ray excitation beam a procedure by scanning a 0.5 mm thick copper wire has been conducted (Fig. 4.5). For that purpose the Cu wire was scanned in 0.25 mm steps, and the detected Cu peaks on the recorded spectra defined the

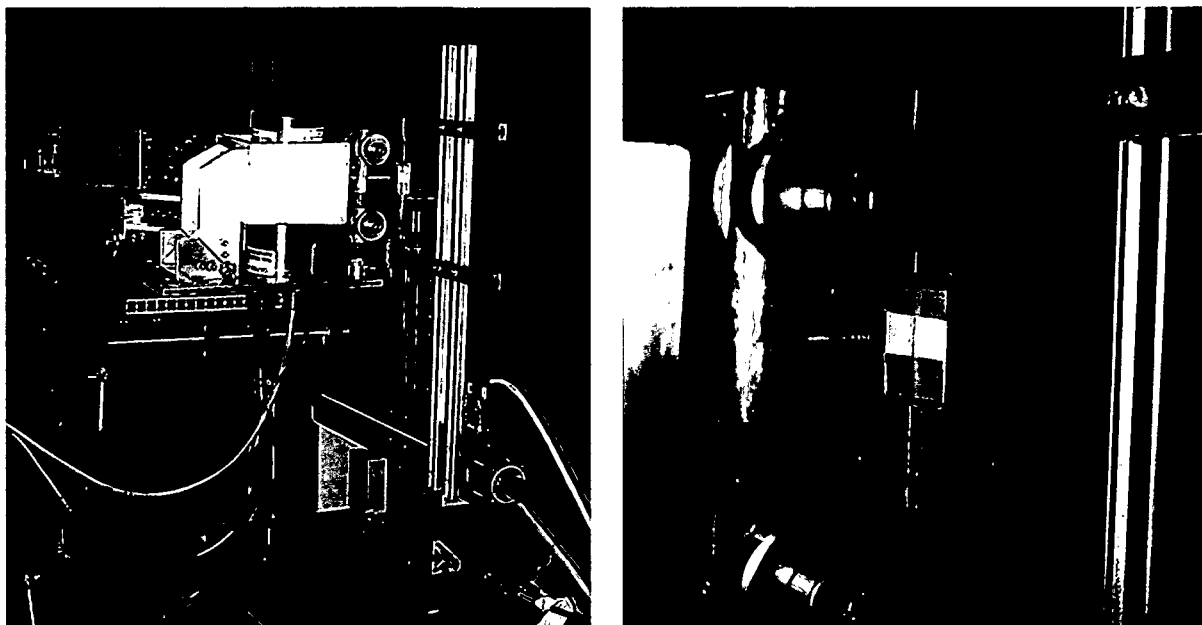


Figure 4.5: Experimental set up for determining of the x-ray beam diameter. A 0.5 mm thick Cu wire is being scanned in 0.25 steps, and the spatial resolution of the detected Cu characteristic radiation yields the diameter of the x-ray excitation beam.

diameter of the x-ray beam (Fig. 4.6). The Gaussian-like spectrum of the Cu K α intensities plotted against the scanning distance (in mm) characterizes the beam diameter as maximum 2.1 mm wide, with a FWHM of ca. 1.5 mm. Therefore, an area irradiated with x-rays during a measurement is ca. 3.8 mm².

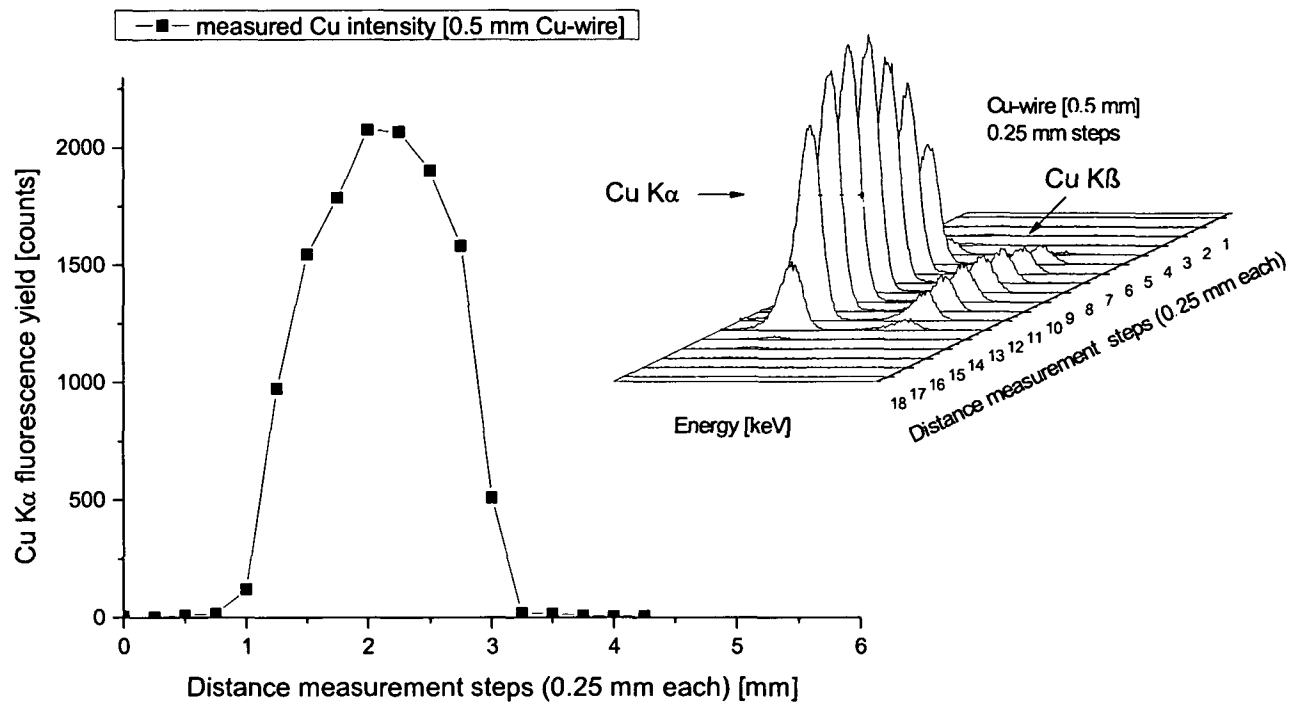


Figure 4.6: Detected Cu K α intensities plotted against the scanned distance in 0.25 mm steps. The diameter of the x-ray beam is ca. 2 mm.

4.2.4. Sum Peaks Effect and Speed Processing Electronics

Besides achieving a better MDL, the benefits of higher count rates can also be observed when investigating the sum peak effects. Processing of the pulse created by a photon must be completed before another pulse occurs and a pileup rejector acts as an electronic guard that blocks a pulse if it is received too soon. If, at high count rate applications, two photons arrive at the detector coincidentally within a time difference lower than the fast discriminator can act (i.e. the pulses in the detector are not being processed fast enough), a pileup may occur, resulting in artifact peaks, which appear at energies equal to the sum of the photon energy of the first and second photons to enter the detector.

The high advantage of the SDD detection system regarding the sum peaks could be demonstrated during an experiment, where for comparison an investigation was carried out on an iron-alloy standard (83.18 wt% Fe) using a laboratory XRF on one side, and the portable XRF on the other. The same operating conditions (30 kV, 0.6 mA, 350 s acquisition time) were employed and the resulting spectra are shown in Figure 4.7. The Fe sum peaks can be observed at the energies of 12.8 keV (double the energy of Fe $K\alpha$ line) and 13.45 keV (energy from Fe $K\alpha$ + Fe $K\beta$ line). In the inserted spectrum (on a linear scale) the difference between the spectra obtained with two different detectors can be clearly seen. The Fe sum peaks are rather strong in the spectrum obtained using the lab XRF with a Si(Li)-detector, whereas in the portable XRF spectrum using a SDD they are hardly visible. Because of extremely small overall capacitance of this type of detector, very short shaping times are possible (e.g. 1.0 μ s in our case). Consequently, extremely high count rates are possible (see Chapter 3) and due to the high pulse processor speed hardly problems with sum (pileup) peaks occur.

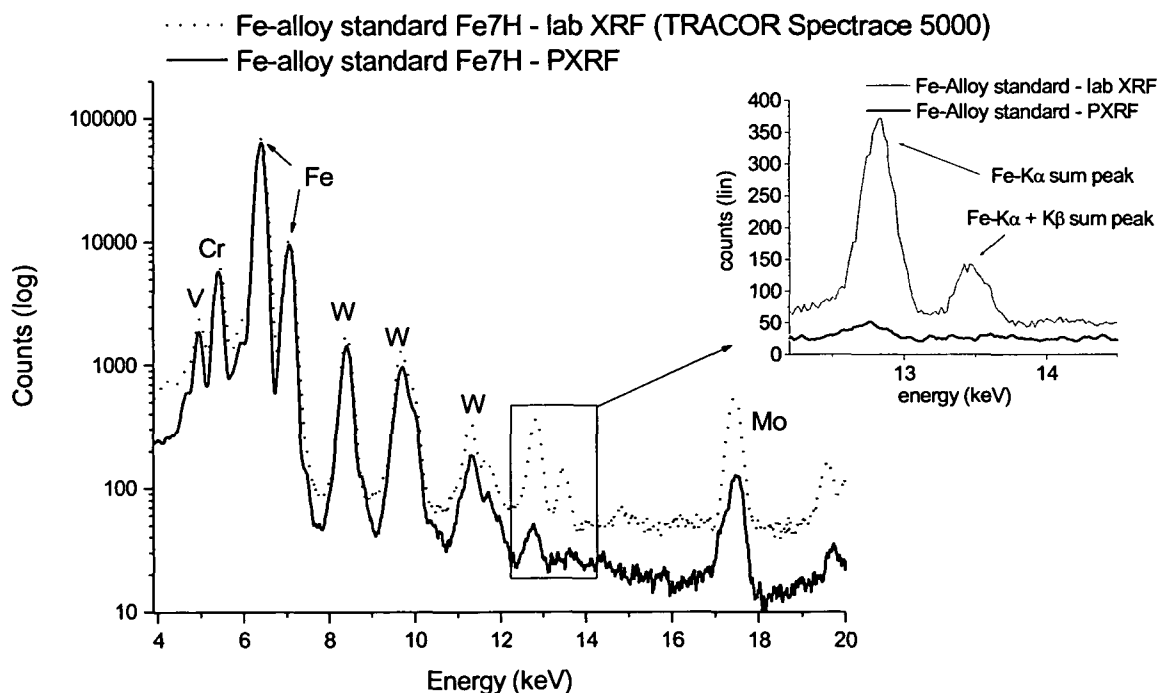


Figure 4.7: Spectra of a Fe-alloy with known elemental composition. Strong Fe sum peaks appear in the spectrum obtained with the lab XRF Spectrace 5000 of Noran Instruments/USA (marked area at ca. 13 keV). This instrument is equipped with a Si(Li) detector. The effect of the Fe sum peaks in the spectrum of the self-built portable XRF is significantly lower.

4.3. Care and Maintenance of the PXRF System

The lack of moving parts and dependable electronics make this system a reliable instrument, which can be used for many years to come. But still, some precautions and proper maintenance are necessary, and improve the reliability of this instrument.

4.3.1. X-Ray Source

The x-ray tube operates in high vacuum and the x-ray exit is sealed with a 125 μm thick beryllium window. Besides being toxic, beryllium is extremely brittle, and even a finger touch can rupture the window. In this configuration it is protected by the collimating device mounted over it, but in a case of repairs or collimator readjustment, special care should be implemented.

If the tube has not been in use for a prolonged period of time (couple of weeks) it may become gassy, and if brought rapidly to full power it may electrically arc between the filament and the anode. If this happens, the thin plating of the anode target element (Rhodium) on the copper base may be pitted. This can create intensity instability due to the migrating of the electron beam about the pit's edge, and if the pitting is sufficiently deep, copper x-rays may be emitted.

To avoid arcing in such a case, where a tube has not been used for a while, a break-in (warm up) procedure is recommended. For automatic execution of this procedure a sub-program has been written and implemented within the main software package, which may be started at any time. It is the tube voltage which is critical. Therefore, the procedure recommended by Oxford Instruments (x-ray tube manufacturer of the tube used in this PXRF) employs the following stepped pattern:

1. Turn kV on to 40% of maximum rating (=20 kV)
2. Turn mA on to 50% of maximum rating (=0.5 mA) and wait 10 seconds
3. Increase kV to 60% of maximum rating (=30 kV)
4. Increase mA to 100% of maximum rating (=1.0 mA) and wait 10 seconds
5. Increase kV to 80% of maximum rating (=40 kV) and wait 10 seconds
6. Increase kV to 100% of maximum rating (=50 kV)

Another possible reason for occurrence of the arcing effect may be a dirty connector on a high voltage cable inside the tube. In that case electrical arcing occurs due to the poor contact of the cables within the tube and not between the anode and the cathode, but it should be avoided nevertheless.

4.3.2. Detector Maintenance

The detector entrance window has a beryllium window just like the x-ray tube, but it is in our case only 8 μm thick. Therefore, similar precautions given for the x-ray tube apply. There is a zirconium collimator mounted in front of the window which protects the beryllium window, but a high degree of precaution should be applied nevertheless, especially during transportation.

4.4. Improvement Suggestions

4.4.1. Secondary Radiation for Excitation

The x-ray tube produces a polychromatic radiation, i.e. a characteristic radiation of its anode. This primary radiation is used to irradiate a sample directly or a secondary target which, in turn, irradiates the sample with secondary monoenergetic x-rays. As in the case of isotopic sources, several secondary targets would be required to efficiently cover a wide range of elements. Polychromatic radiation has an advantage in its capacity to excite a wide range of elements; however, the resulting spectrum is superimposed over a high background. With the use of monochromatic x-rays, on the other hand, one can excite a more limited range of elements, but the background is very low. Therefore, secondary irradiation is often used for trace-

element mapping, where the lower background is important, and primary excitation is used in major-element analysis, where excitation of a wide range of elements is required. Another reason, why a secondary target may be used in order to produce monochromatic radiation, is that many of the fundamental-parameter computer programs, which are used to compute intensities directly from the basic x-ray equation, require monochromatic excitation radiation.

4.4.2. Primary Filters

In practice, however, secondary target excitation only approaches the ideal monochromatic radiation. It has been shown that the proper use of direct tube excitation with well selected primary filters performs as well as secondary target techniques [96]. Furthermore, one of the main strengths of the energy dispersive techniques lies in its simultaneous multielement analysis capabilities. Therefore, any design features, which limit the instrument's potential of simultaneous multielement analysis, will diminish the advantage of the energy dispersive spectrometer.

The main reason for the use of primary filters is to reduce the background in the spectrum energy range to be investigated in the analysis. For this purpose a filter is placed between the x-ray tube and the sample, in order to filter the primary radiation from the x-ray source. By using a filter made of the same element as the tube anode (Rh), it selectively passes the characteristic lines of that element. The theory behind this effect is the following: the x-rays of a given line of an element are lower in energy than the absorption edge for that element. That means that the photoelectric component of the mass absorption coefficient is small and the filter does not efficiently absorb the characteristic lines emitted by the x-ray tube. On the other hand, the higher energy x-rays from the continuum are efficient for the photoelectric process in the filter, and are highly attenuated by absorption. Furthermore, x-rays of lower energy than the filter material absorption edge are absorbed more efficiently as the energy decreases. That means that the intensity of x-radiation striking the sample stems mostly from the characteristic lines of the tube anode, and approximates monochromatic radiation.

5. Case Studies and Experimental Results

A variety of measurements on objects/samples of different size, shape and material have been carried out using the instrument described in this thesis. It was successfully employed for studies of artistic and historical objects in museums and galleries, ceiling frescoes in churches and cathedrals, and analysis of various other objects of interest needing a swift, precise, and non-destructive chemical characterization. This chapter gives an overview of some of the more specific applications, where the PXRF has been utilized for characterization of mural paintings, both on the isolated wall fragments and directly in a church, characterization of wood panel lacquer decoration (lacquerware), and enameled stained glass fragments.

5.1. Mural Paintings on Fragments from the St. Stephan's Cathedral in Vienna

During conservation and restoration of the mural paintings on fragments originating from the St. Stephan's Cathedral in Vienna, a need for precise determination of the pigments' composition arose. The fragments stored in the Historical Museum in Vienna differ in size and shape drastically, with the biggest one being over 1 meter long and weighing well over 200 kg. So the PXRF measurements on that object had to be carried in the conservation department and the experimental set up is shown in Fig. 5.1.

The objective of the analysis was to determine chemical composition of the pigments used in red, yellow, green, black, orange and brown areas of the wall painting. The investigation was carried out on 14 different measuring points (Tab. 5.1), with instrument conditions for tube voltage, anode current and acquisition time set to 30 kV, 0.6 mA, and 200 s, respectively.

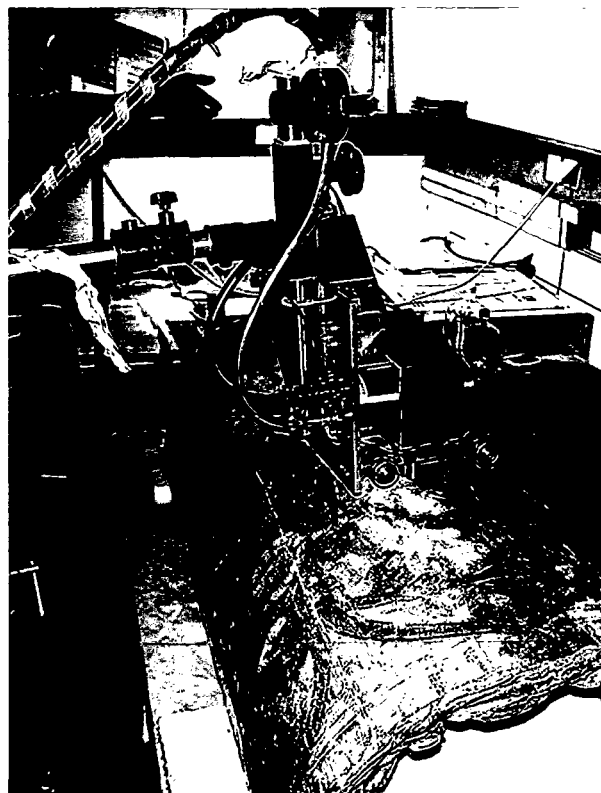
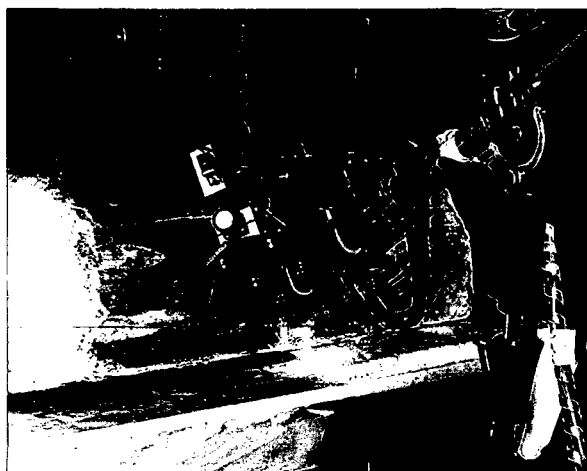


Fig. 5.1: Photographs taken during the investigations of the mural paintings on a fragment from the St. Stephan's Cathedral in Vienna.

Table 5.1 summarizes the measuring points and results obtained using the PXRF. The elements K, Ca, Ti, Mn, Fe und Sr stem presumably from the primary layer underneath the painting.

Fig. 5.2 shows a PXRF spectrum obtained on 3 different red areas of the mural painting. The high amount of lead in the reds 1 and 2 indicate that minium (Pb_3O_4) has been used as a colorant, whereas the existence of mercury and sulphur in red 3 indicates the usage of cinnabar (HgS). The elements Ca, Mn, Fe stem mostly from the primary layer. But the increased Fe intensity (relative to Ca) in the first two red areas (Fig. 5.3) indicates that, beside minium, red ochre has been used as well.

Measuring point	Color	Elements detected	Pigments possibly used
1	Red 1	Fe, Pb , Ca, Cu,	Red ochre, minium, possibly mixed with lead white
2	Red 2	Fe, Pb , Ca, Cu,	Red ochre, minium, possibly mixed with lead white
3	Yellow 1	Fe , S, Ca, Ti, Mn, Sr, Pb, (K)	Yellow ochre (possibly mixed with lead white)
4	Yellow 2	Fe, As , S, Ca, Ti, Mn, Sr, Pb, (K)	Yellow ochre + auripigment (possibly mixed with lead white)
5	Green 1	Fe, Cu , S, Ca, Ti, Mn, Sr, Pb, (K, Zn)	Green earth + green Cu-pigment, possibly lead white
6	Green 2	Fe, Cu , S, K, Ca, Ti, Mn, Sr, Pb, (Zn)	Green earth + green Cu-pigment, possibly lead white
7	Black 1	Ca, Fe , Pb, (K)	Carbon black (possibly mixed with lead white)
8	Black 2	Ca, Fe , Pb, (K)	Carbon black (possibly mixed with lead white)
9	Light yellow 1	As , K, Ca, Ti, Mn, Fe, Sr, Pb	Auripigment
10	Light yellow 2	As , K, Ca, Ti, Mn, Fe, Sr, Pb	Auripigment
11	Orange 1	Pb , Ca, Fe, Sr	Minium (possibly yellow or red ochre as well)
12	Orange 2	Pb , Ca, Fe, Sr	Minium (possibly yellow or red ochre as well)
13	Red 3	Hg , S, K, Ca, Mn, Fe, Sr, Pb	Cinnabar (possibly with lead white)
14	Brown 1	Fe , S, K, Ca, Ti, Mn, Cu, As, Hg, Pb	Brown ochre (possibly burnt umber)

Tab. 5.1: List of the analyzed measuring points as well as the found elements and possible pigments. Elements listed in bold are present as main components, elements in brackets as traces.

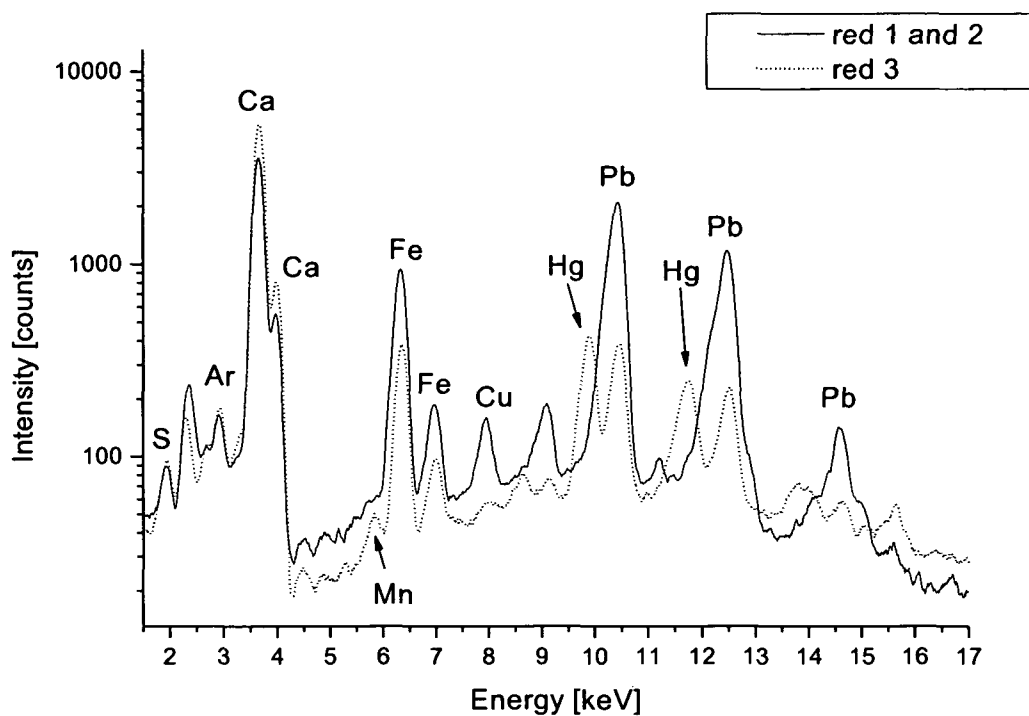


Fig. 5.2: PXRf spectra of 3 red painted areas of the mural painting on the wall fragment from St. Stephan's Cathedral in Vienna.

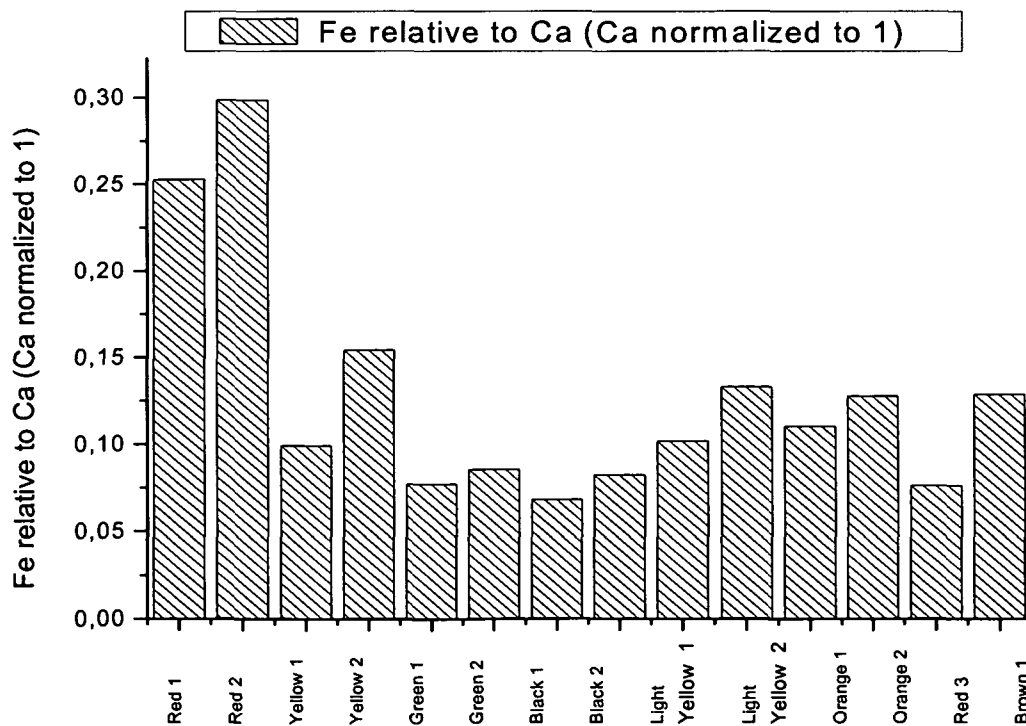


Fig. 5.3: Iron intensities detected in different pigments (peak net area) on 14 different measuring points, relative to Ca (with Ca normalized to 1).

Lead detected at the measuring points 7, 8 (both black) and 9, 10 (both light yellow) stems probably from the layer underneath. As and Pb at the measuring point 14 comes presumably from the yellow layer underneath (Auripigment, possibly with lead white), and Hg from the neighboring reddish paint layer (presumably Cinnabar). The PXRF spectra obtained at the measuring points 3-12 and 14 are shown in Fig. 5.4.-5.9, presented on the following pages.

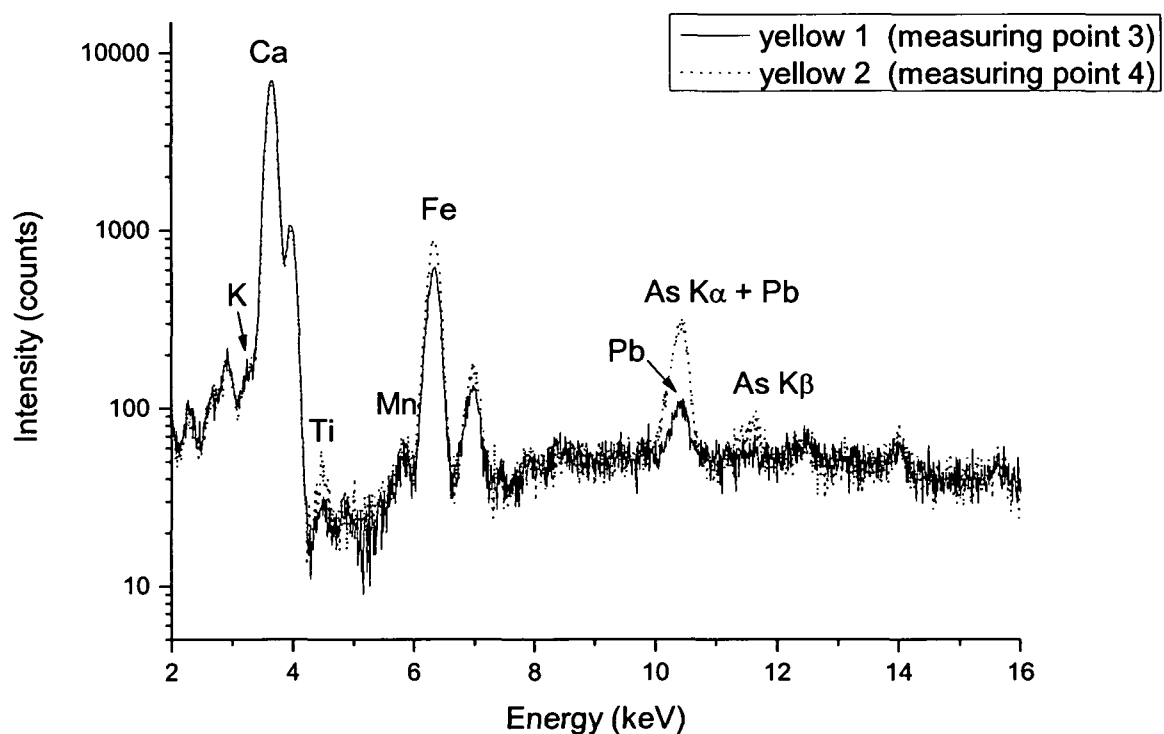


Fig. 5.4: Measuring points 3 and 4 (yellow).

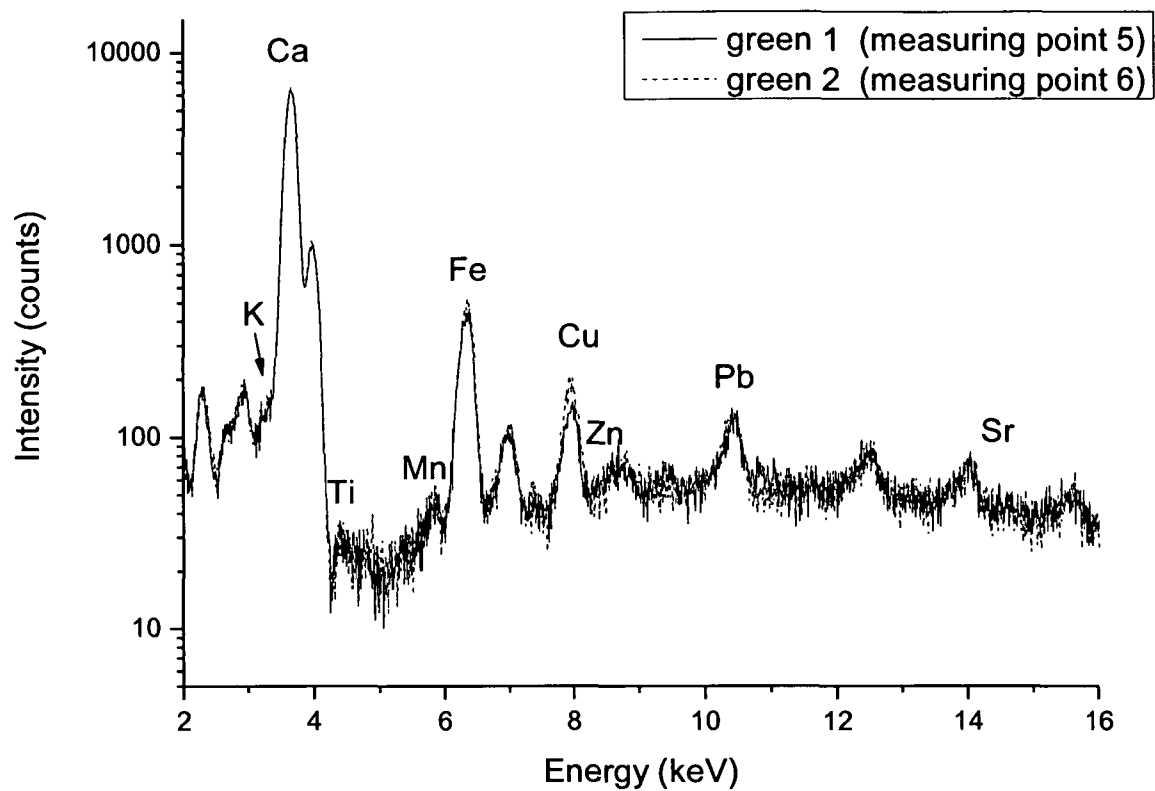


Fig. 5.5: Measuring points 5 and 6 (green).

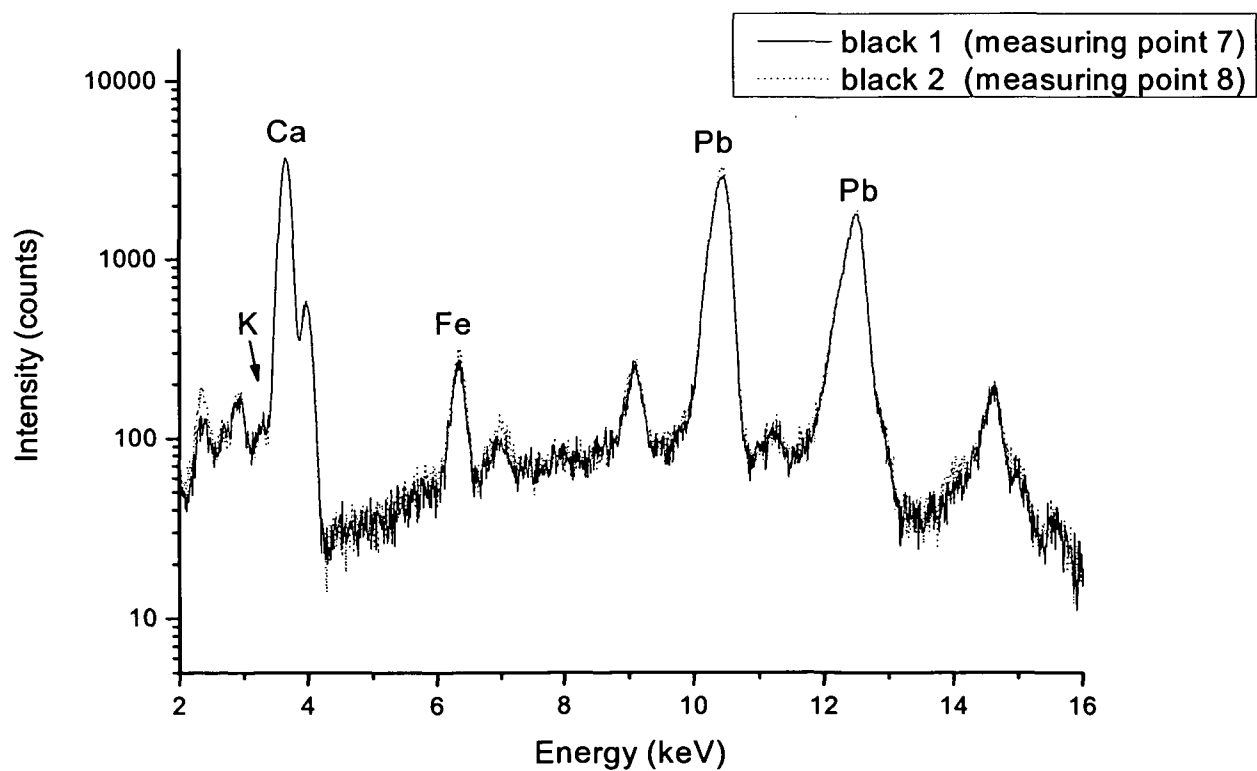


Fig. 5.6: Measuring points 7 and 8 (black).

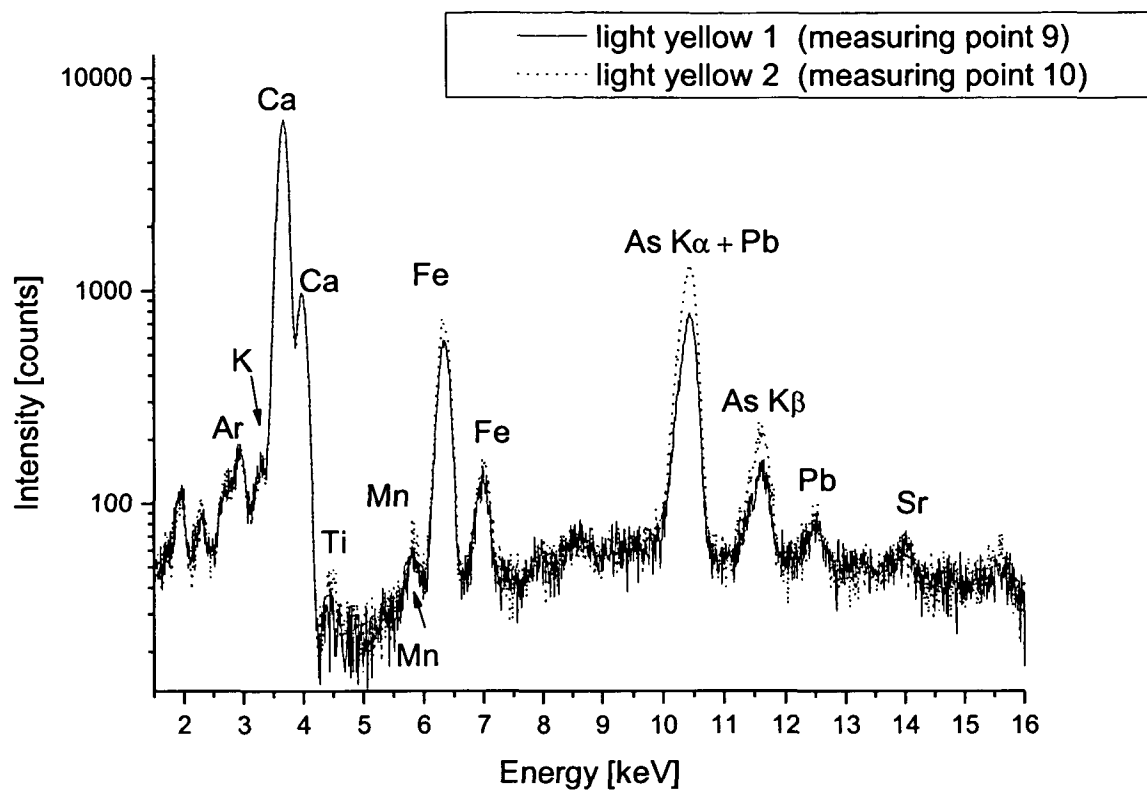


Fig. 5.7: Measuring points 9 and 10 (light yellow).

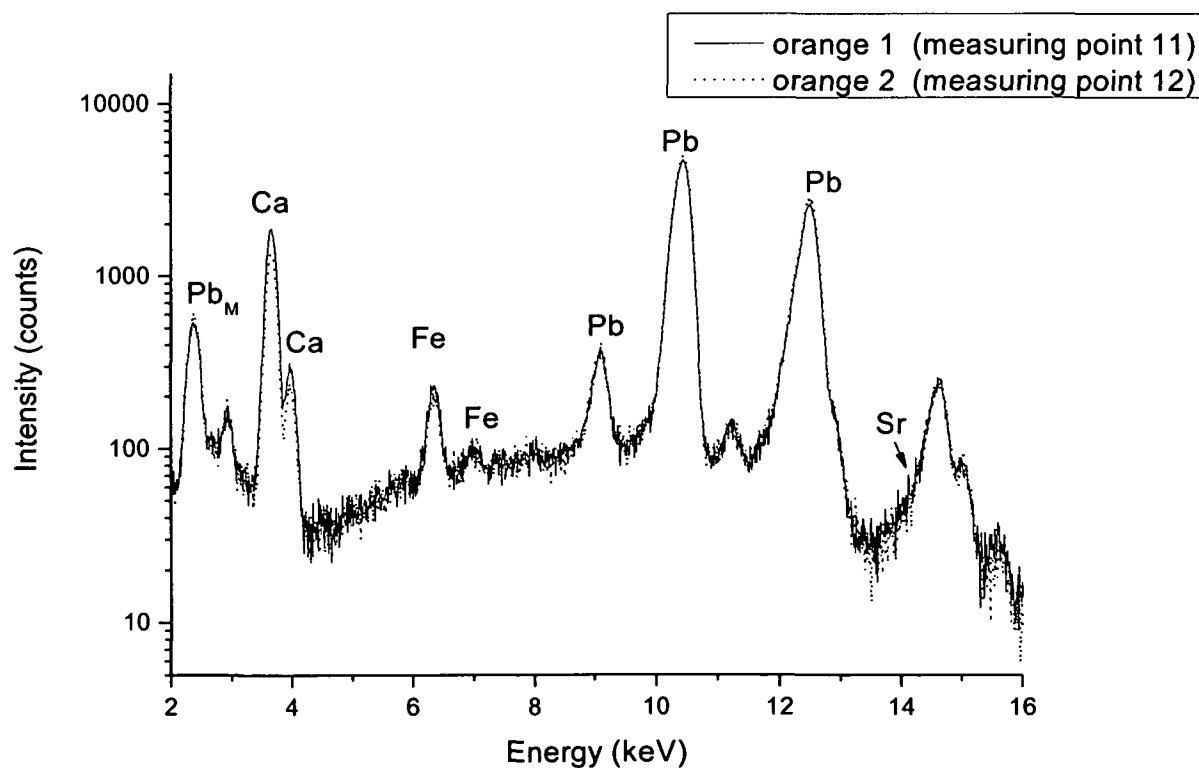


Fig. 5.8: Measuring points 11 and 12 (orange).

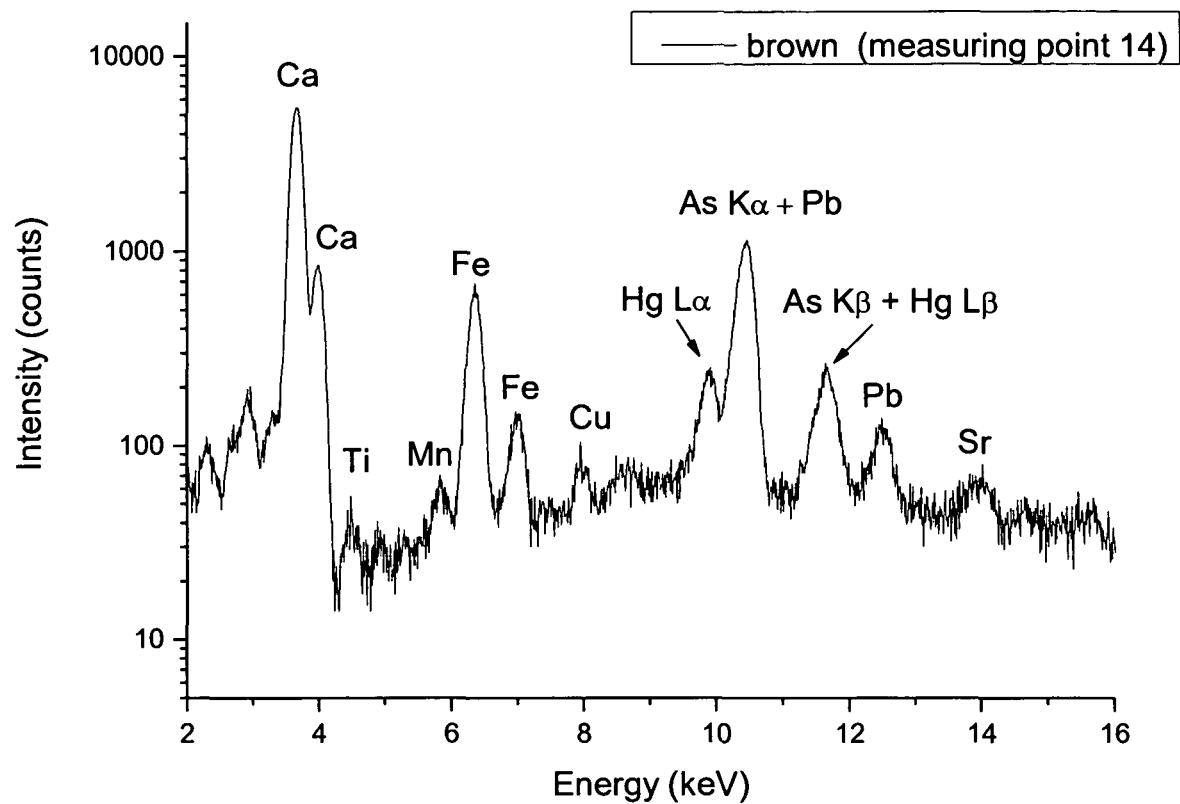


Fig. 5.9: Measuring point 14 (brown).

5.2. Chinese Lacquer Panel Paintings in the Schoenbrunn Castle in Vienna

Another example of the measurements carried out in field was a PXRf application during the conservation of the Vieux Laque Room in the Viennese Schoenbrunn Castle (Fig. 5.10). This baroque castle with more than 1400 rooms, often referred to as the "Versailles of Vienna", was designed by the architect Fischer von Erlach and built in the late 17th century. Ever since the reign of Empress Maria Theresia the castle has been the main residence of the Habsburg family in Vienna, one of the most powerful dynasties of Europe. The Vieux Laque Room ("room with old lacquered wood") is a room tiled with around 70 m² of Chinese lacquer panel paintings, presumably dating from the mid 17th century. Lacquerware is an ancient decorative art form, developed in China and evolved in Korea and Japan, in which different (mostly) metal powders and pigments are mixed with lacquer, before being applied to wooden panels and other objects to be decorated.



Fig. 5.10: Investigation of the Chinese lacquer panel paintings in the Viennese Schoenbrunn Castle.

The spectra of two differently shaded gold lacquer areas analyzed with the portable XRF during the *in situ* measurements in the Schoenbrunn Castle are shown in Fig. 5.11. Varying shades of the golden parts can be explained by the different concentrations of Fe and Cu, that were added to the gold powder before being mixed with varnish and used to decorate the panels. The darker colored gold areas show higher concentrations of Fe and Cu, whereas in the lighter areas the concentration of these additives is lower. Strong Pb L α lines come from the pigment lead white, which was applied as a primary color beneath the lacquering.

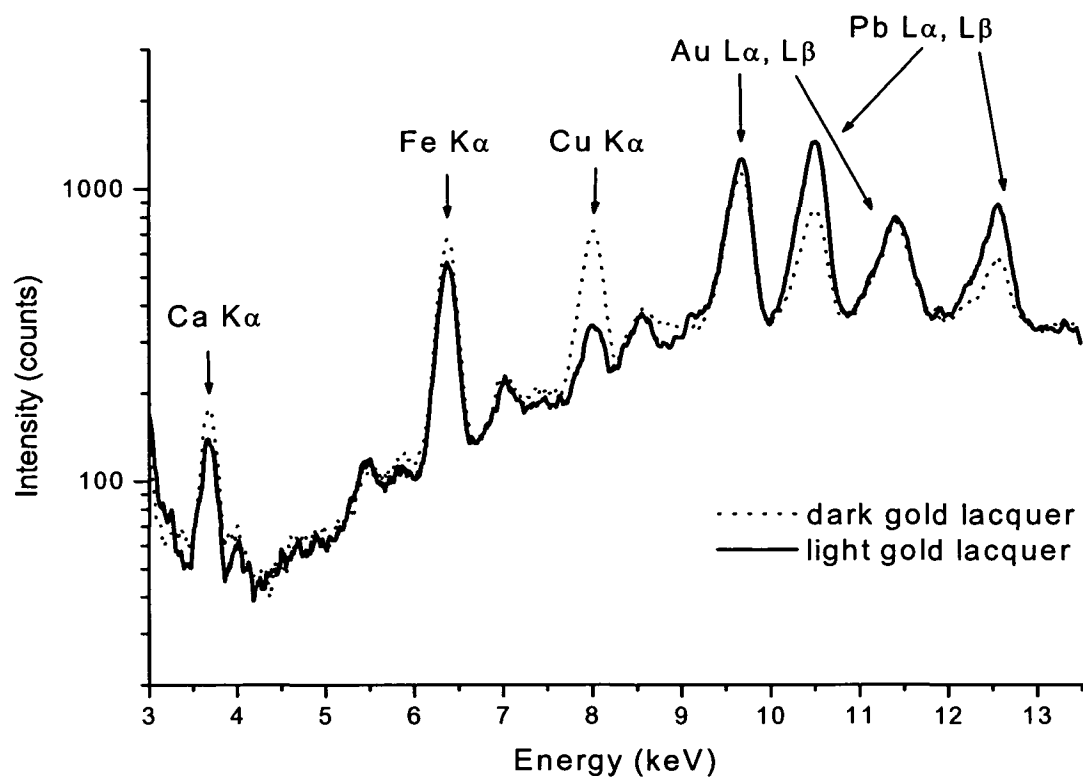


Fig. 5.11: Comparison spectra of two differently shaded gold lacquer areas obtained with the portable XRF during the examinations of the Chinese lacquer panels in the Schoenbrunn Castle in Vienna. Different shades of the golden parts can be explained by the different concentration of Fe and Cu in the golden powder used to decorate the panels.

5.3. Mural Paintings of the St. Nicholas Church in Winkl

In the year 2003, in a small town of Winkl in Lower Austria (near Vienna), a mural painting, presumably dating from the year 1220, was discovered. It was painted on the outer north wall of the St. Nicholas Church dating from the late 12th century. The painting was hidden by a second side-roof (Fig. 5.12), and was discovered during restoration of the roof above it. The national authorities started a conservation campaign one year later, in March 2004.

One of the problems encountered during conservation was that the only access to the mural painting was through a small hole in the wall (Fig. 5.12). Therefore, the scientific equipment for *in situ* investigations and determination of the pigments needed to be small, compact, and mobile. The portable XRF (PXRF) was used for this purpose and the experimental set up is



Fig. 5.12: The Church of St. Nicholas in Winkl (near Vienna), where a mural painting from the 13th century was found. Until its discovery in the year 2003 the wall with the painting was hidden by the second side-roof of the church, and is now accessible only through a small hole in the wall, as seen in the background of the right photo (arrow). This photo was taken during PXRF investigations in 2004.

shown in Fig. 5.12 and 5.13. The whole area of interest, including the measurement points, is depicted in Fig. 5.14 and the summary of the measuring points is listed in Table 5.2. During the investigation 24 measurements were carried out, with the following instrumental conditions: 35 kV accelerating voltage, 0.6 mA tube current, and 100 s acquisition time.



Fig. 5.13: Photos taken during investigations using a PXRF, in order to obtain the elemental composition of the pigments used for the mural painting.

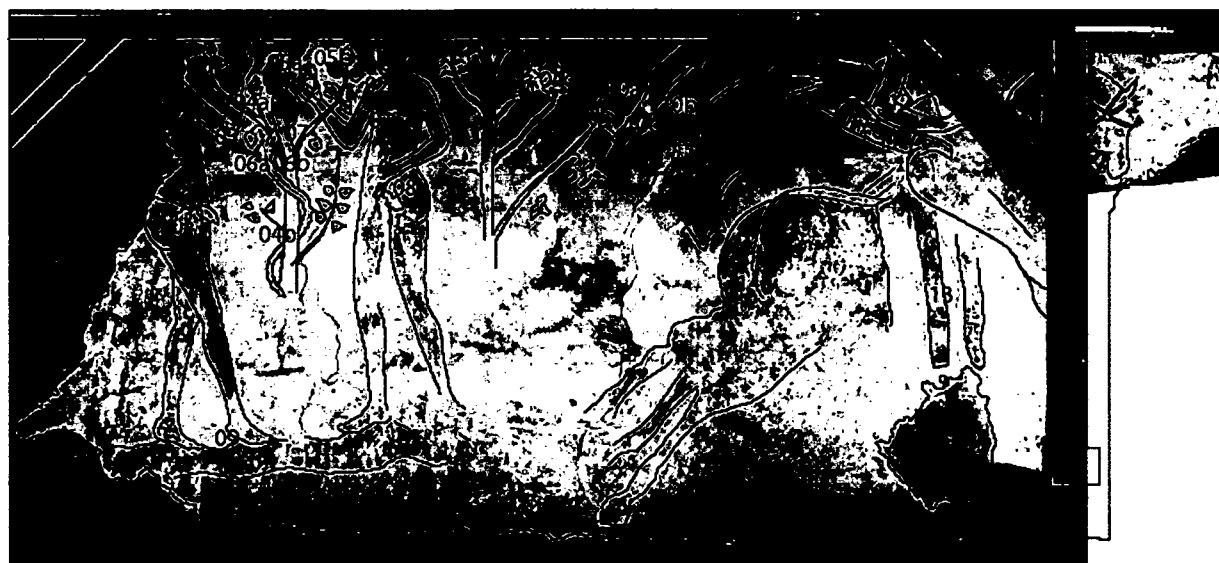


Fig. 5.14: The mural painting, with the measurement points. The contours of the figures and the numbers defining the measuring points were added for easier and clearer presentation.

Measuring point	Description	Color	Remarks	Elements detected	Pigments possibly used
1	Adam, upper arm	Pink	Comparison with Eva	Fe, Pb, K, Ca, Ti, Mn, Cu	Red ochre, mixed with minium or lead white
2	Adam's pipe	Black	Probably a more recent drawing	K, Ca, Ti, Mn, Fe	Carbon black
3	Eva, arm	Pink	Comparison with Adam	Fe, Pb, K, Ca, Ti, Mn, Cu, Sr,	Red ochre, mixed with minium or lead white
4	Leaf 1	Red	Chemical (elemental) differences between the leafs	Fe, Pb, K, Ca, Ti, Mn, Sr	Red ochre (possibly mixed with minium or lead white)
5	Leaf 2	Red		Fe, Pb, K, Ca, Ti, Mn, Sr, (Cu)	
6	Leaf 3	Red		Fe, Pb, K, Ca, Ti, Mn, Sr	
7	Apple 1, black/red mixed area	Black/red	Comparison with rider's upper garment	Fe, Pb, K, Ca, (Ti, Mn)	Minium and red ochre, possibly mixed with lead white
8	Apple 2, red area	Red	– blackening of the Pb-	Pb, P, K, Ca, Fe, (Ti, Mn)	
9	Apple 3, black area	Black	containing pigment?	Fe, Pb, Ca, (K, Ti, Mn)	
10	Snake 1, area	Green-brownish		Fe, Pb, K, Ca, Ti, Mn, (Cu, Sr)	Minium and red ochre, possibly mixed with lead white
11	Snake 2, contours	Red		Fe, Pb, K, Ca, Ti, Mn, (Sr)	Minium and red ochre, possibly mixed with lead white
12	Tree	Gray		K, Ca, Ti, Mn, Fe, Cu, (Zn, Pb, Sr)	
13	Adam, fig leaf	Colorless (whitish)		K, Ca, Ti, Mn, Fe, Cu, (Zn)	
14	Eva, flower	Black		Pb, K, Ca, Ti, Mn, Fe, (Cu, Zn, Sr)	Minium, possibly mixed with red ochre and/or lead white

15	Rider, upper garment, light	Light-red (pink)	Comparison with apple, saddle stripes	Ca, Fe, Cu, (Ti, Mn, Zn, Sr, Pb)	
16	Rider, upper garment, contour	Brownish (black)		Fe, Pb , K, Ca, Ti, Mn, (Sr)	Red ochre and minium, possibly mixed with lead white
17	Rider, upper garment, dark	Red		Fe, Pb , K, Ca, (Ti, Mn, Sr)	Minium and red ochre, possibly mixed with lead white
18	Rider, sword	Gray-brown (light)		Pb , K, Ca, Ti, Mn, Fe, (Zn, Sr)	Minium, possibly mixed with red ochre and/or lead white
19	Rider, hand	Pink		Fe , K, Ca, Ti, Mn, Cu, (Sr)	Red ochre
20	Horse, saddle top stripes	Brown-black	Comparison with apple and rider's garment	Fe, Pb , K, Ca, Ti, Mn, (Cu, Sr)	Minium and red ochre, possibly mixed with lead white
21	Horse, torso	Red (strong)		Fe , Pb, K, Ca, Ti, Mn, (Cu, Sr)	Red ochre, mixed with minium and/or lead white
22, 23, 24	Background 1, 2, 3	White		Ca, Fe, K, Ti, Mn, (Cu, Zn, Sr)	

Table 5.2: Description of the 24 measurement points with the XRF results of the mural painting in the St. Nicholas Church in Winkl (bold – main components, in brackets – trace elements).

Table 5.2 lists the measuring points, where the investigations were carried out, as well as the elements determined and the pigments possibly used for the painting. The measurements performed on the background (measuring points 22-24) yielded Ca and Fe as main constituents with K, Ti, and Mn as accompanying elements. Traces of Cu, Zn, and Sr in the background were determined as well. These results enable the calculation of a Fe/Ca ratio in the background. Comparing this value with the Fe/Ca ratios in other investigated areas (Fig. 5.15) yields valuable information regarding the coloring substance. If the Fe content (relative to Ca content) of the coloring material is 2-3 or even more times the Fe content, which was deter-

mined in the background, it can be presumed that some kind of an iron oxide (red or yellow ochre) was used as a pigment.

The black/brown appearance of the measuring points 7, 9, 14, 16, 18, and 20 (see Table 5.2), whose initial color was presumably red, can be explained by the blackening of the applied pigment. Under the influence of light, minium (Pb_3O_4) may turn with the time into brown to black PbO_2 . Lead white may also show tendency of blackening with the time, by reacting with sulphur hydrogen (from the air or from other colorants), and turn to lead sulphide (PbS). Thus, pigments with higher Pb concentration (meaning more minium and/or lead white) may exhibit stronger darkening. This corresponds well to the visual comparison of the investigated areas with the corresponding XRF spectra.

When comparing the values in Fig. 5.15, one should consider the possible non-linear correlation between the altering of the Fe/Ca ratio in the sample and the altering of the iron's real concentration in the pigment itself. As already mentioned, Fe and Ca can be found in the background, as well as in the layer underneath the painting. Therefore, a certain amount of Fe and Ca detected in the painted area stems actually from these layers. Theoretically, if there is no Fe and Ca in the pigment, the detected Fe/Ca ratio should remain more or less constant. Consequently, the certain amount of Fe in the pigment should cause proportionally higher overall Fe intensity. However, even though, e.g., Apple 1 (measuring point 7) exhibits very strong Fe intensities relative to Ca (see Fig. 5.15 and Fig. 5.16), it must not automatically mean that the pigment in Apple 1 exhibits correspondingly higher Fe absolute concentration. Stronger Fe intensities in Apple 1, then in Apple 2, may also be explained by a higher Pb content detected in Apple 2. Pb may attenuate the incident radiation to, and fluorescent radiation from Fe and Ca in the background layer, yielding much lower initial Fe and Ca background intensity values, thus altering the background layer information. In that case, with a lower initial Fe/Ca ratio, an iron increase stemming from red ochre will yield a much higher percent difference and have a much stronger impact on the change of the overall Fe/Ca ratio. Therefore, not only the Fe/Ca ratio should be considered when investigating the colorants, but the varying of the overall Fe and Ca concentration should be taken into account as well.

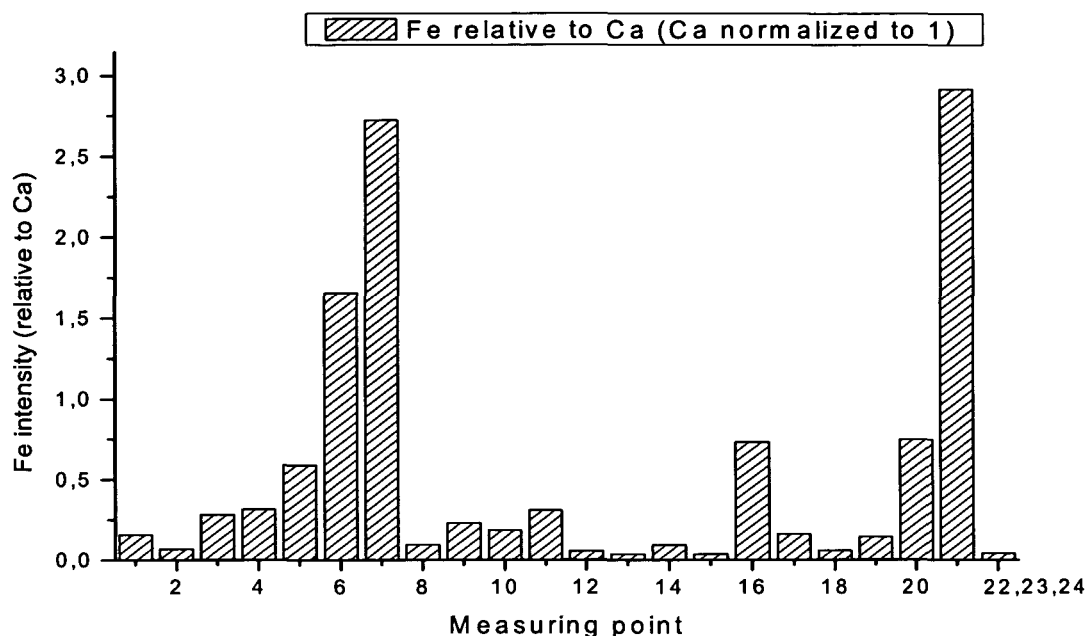


Fig. 5.15: Fe/Ca ratios determined in each measuring point; Ca is normalized to 1. Ratio of 0.041, as determined in the background as well as in the layer underneath the painting (measuring points 22, 23, 24), can be used as a comparative value in determining Fe containing colorants used in other measuring points.

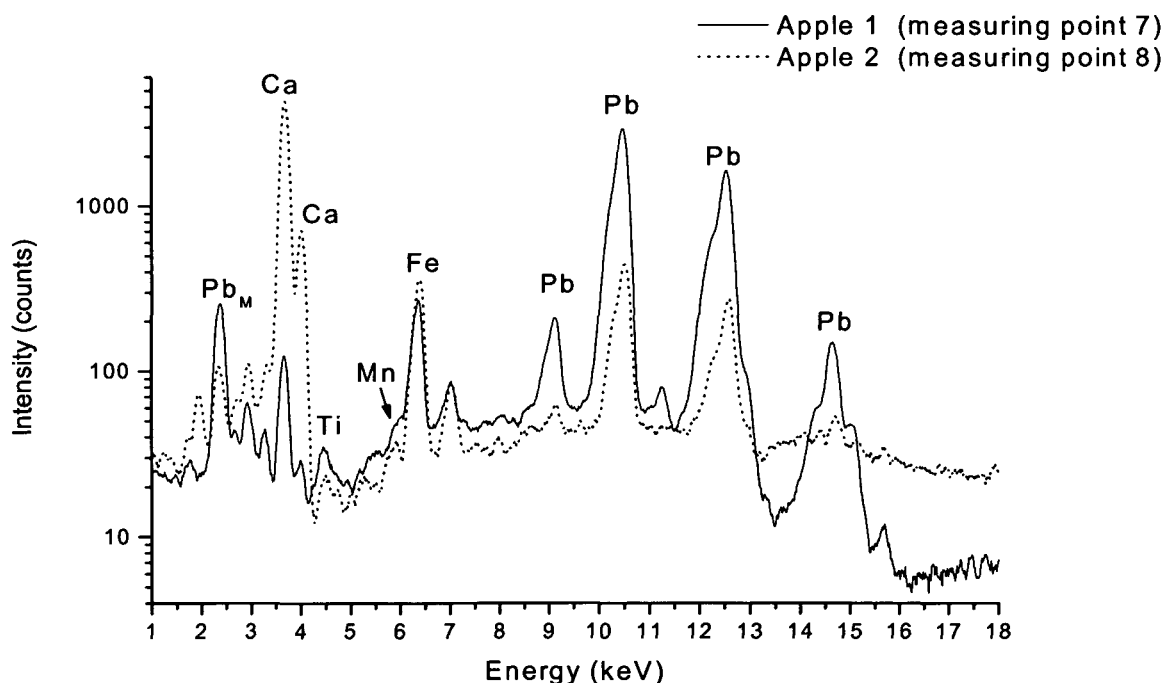


Fig. 5.16: Spectra obtained at the measuring points 7 and 8 corresponding to Apple 1 and Apple 2, respectively. Lower Ca and Fe concentrations from the background of Apple 1 may be explained by the higher Pb content in the pigment used for Apple 1, which alters the information from the layers beneath.

5.4. Research of the Enameled Stained Glass Fragments

The use of enamel for glass painting dates back to the 16th century and reaches its high point during the 17th century. In the 18th century white windows started dominating again, parallel to the new spirit dictating as much light into a church/cathedral as possible. Furthermore, there was a fear that the stained glass would produce colored light, which may obstruct the color of the displayed paintings. During that period a lot of stained glass was destroyed and changed to white glass. Hence the knowledge of producing and manufacturing such artifacts was lost until the 19th century, where a kind of Renaissance of such techniques took place. However, a great difference in constructing such objects as well as in the glass production (chemical composition of the bulk glass and the enamel) must be determined.

In order to obtain material, which can be used for enameling glass, colored glass was used, heated, and ground until a fine powder is obtained. To lower the melting temperature of the paint extra glass flux is added to the powder. Most fluxes contain around 45% PbO, 35% SiO₂, and 10% B₂O₃, but other elements can be added as well. It is baked at 1000-1300°C for 80-120 minutes and afterwards mixed with glass, in an 80/20% flux to fine glass powder ratio. The mixture is then ground and let through a sieve, where the largest grains stay behind. To get a glass paint powder these grains are dried, pulverized, and subsequently sifted. Depending on the factory where the powder is manufactured, an organic medium may be added. When applied to the glass surface, these enamel colors are baked at 580°C. The lowest temperatures for applying glass paints lies around 630°C, and that is the reason why the enamel is applied as a last paint layer on a stained glass piece.

Purple (violet) enamel occurs less frequently than other colors of enamel, but it corrodes, together with the blue enamel, much faster than other enamel colors. Earlier research of the blue enamel differentiates two phases of corrosion: it first shows signs of fissures and then follows a phase of desquamate. In order to try to understand this corrosion mechanism of old enamel painted glasses it is, besides researching the historical recipes for paint making, important to investigate the chemical composition of the historical glass pieces, where enamel has been used. Only by knowing the exact elemental composition and by being able to monitor chemical changes in a course of time, it is possible to further investigate the corrosion mechanism of the enamel stained glass.

There is very little known about the composition of purple enamel. It was, therefore, interesting to compare the paints of different centuries (17th century compared to 19th century) and to try to obtain as much information as possible (Fig. 5.17). The enamel colors were mostly applied to the exterior side of the glass, but sometimes also to the interior side. The enamel on the glass samples used in this analysis was mostly painted on the interior side.

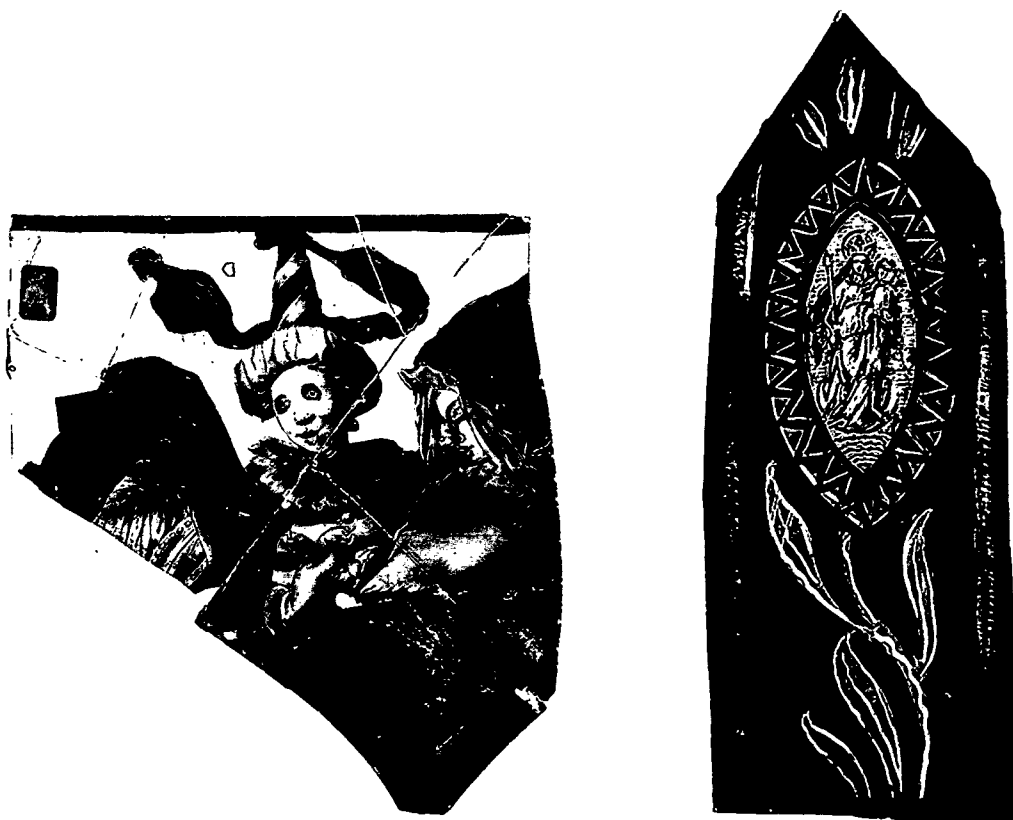


Fig. 5.17: Two examples of the analyzed enameled stained glass fragments, dating from the 17th (left, ID no.: JC48) and the 20th (right, ID no.: JC63) century.

With help of the PXRF analyzer 14 historical glass pieces containing purple enamel were analyzed. The measuring conditions of the instrument (Fig. 5.18) were set to 35 kV accelerating voltage, 0.5 mA tube current, and 100 s acquisition time. Most of them date from the 17th century, except the two which are from the 19th-20th century, and one for which the date of manufacture is unknown. The origin of the fragments is not exactly known, but it can be presumed they were produced in the south part of the Netherlands and north part of Belgium. Therefore, it is most likely that the paint used to color these glass pieces came from somewhere around

Identification number	Date	Object description
jc14	First half of the 17 th century	Figurative, holy Internal side: black contour, grisaille à modeler, red carnation, purple and blue enamel External side: silver stain
jc16	First half of the 17 th century	Figurative, architectural element Internal side: black contour, grisaille à modeler, blue and purple enamel External side: silver stain
jc19	17 th century	Non-figurative Internal side: black contour, grisaille à modeler, blue enamel, purple enamel External side: silver stain
jc21	First half of the 17 th century	Figurative, floral Internal side: black contour, grisaille à modeler, blue enamel with a rougher shining surface, purple enamel with blue tints, carnation External side: silver stain
jc45	First half of the 17 th century	Figurative, flowers in a vase Internal side: black contour, grisaille à modeler, blue enamel, purple enamel (decoration head), carnation External side: silver stain
jc46	First half of the 17 th century	Figurative, hatchment Internal side: black contour, grisaille à modeler, blue enamel, purple enamel, carnation red External side: silver stain
jc47	First half of the 17 th century	Figurative Internal side: black contour, grisaille à modeler, purple enamel, carnation, blue enamel with a hard desquamation External side: silver stain
jc48	Second half of the 17 th century	Figurative, masked persons Internal side: black contour, grisaille à modeler, blue enamel with a rougher shining surface with desquamation purple enamel, carnation External side: silver stain
jc49	First half of the 17 th century	Figurative Internal side: black contour, grisaille à modeler, blue enamel with desquamation, purple enamels with blue tints, carnation External side: silver stain
jc50	Last quarter of the 19 th and first quarter of the 20 th century	Figurative, shield with cross Internal side: black contour, grisaille à modeler External side: silver stain, red purple enamel
jc55	Unknown	Non-figurative Internal side: black contour, grisaille à modeler, purple enamel, carnation red External side: silver stain
jc61	Middle of the	Figurative, grass

	17 th century	Internal side: black contour, grisaille à modeler, blue and purple enamel with desquamation and blue enamel with a rougher surface External side: silver stain
jc63	First half of the 20 th century	Figurative, Maria with child Internal side: black contour, grisaille à modeler External side: silver stain, blue and purple enamel
jc73	Second half of the 17 th and first quarter of the 18 th century	Figurative, architectural element Internal side: black contour, grisaille à modeler, blue enamel, purple enamel with blue spots, carnation red External side: silver stain

Table 5.3: An overview of the glass samples analyzed with PXRF showing their identification number, date, and description of the object.

this area, meaning the Netherlands, Belgium, England, France and/or Germany. The goal was to determine the elemental constituents of differently painted glass fragments and to define the coloring elements. The glass fragments were analyzed on 180 measuring points, on the interior and exterior glass surfaces, and on both colored and clear glass areas. Table 5.3 gives an overview of the analyzed glass samples, showing their identification number, date, and description of the object.

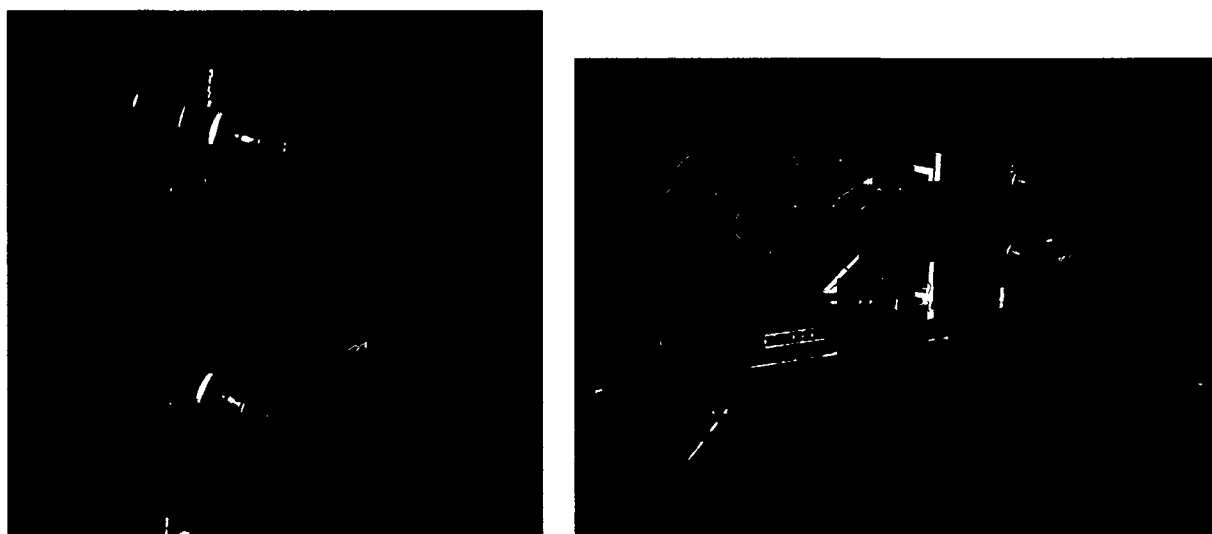


Fig. 5.18: Enameled stained glass fragments in front of the PXRF instrument during measurements.

A thorough data analysis yields a well-defined elemental distinction between the glass samples from the 17th century and the samples from the 19th-20th century. The concentration of K is rather high in all old glass samples (e.g. JC48), whereas no K could be determined in the modern glass samples (e.g. JC63), as shown in Fig. 5.19. Sodium, which can not be detected using the XRF method in air, was subsequently detected in modern glasses using electron beam micro-analysis (EPMA). It can be, therefore, concluded, that the old glasses are based on potash-lime-silica glass, whereas the modern ones are soda-lime-silica glasses. Additional difference between the two glass types is a high Sn content, which could be detected only in modern glass samples (Fig. 5.20).

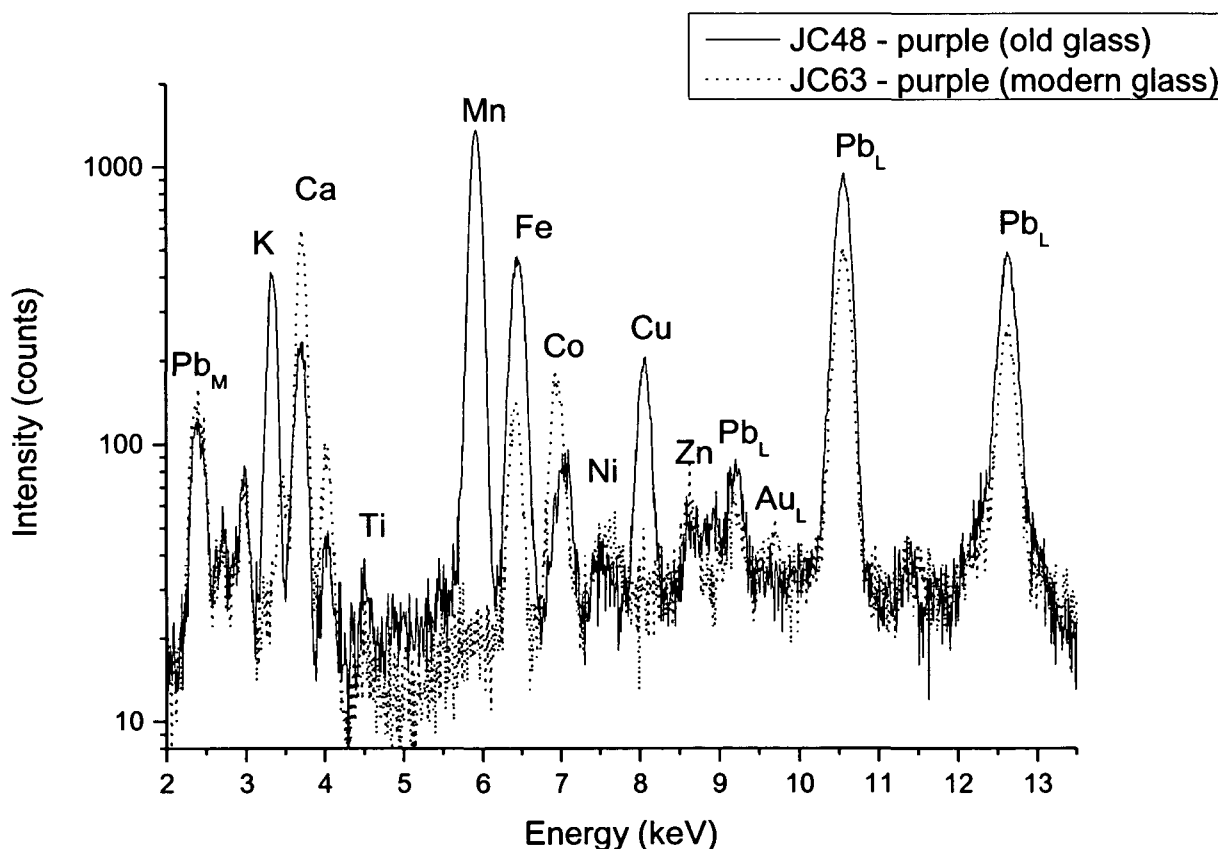


Fig. 5.19: PXRf spectra of two representative 17th and 20th century glass samples (denoted old and modern, respectively). The measurements were carried out on purple painted areas.

When investigating purple enamel, the analyses showed that the coloring element in old purple enamel was Mn, whereas no Mn was found in the purple areas of the modern glasses (Fig. 5.19 and Fig. 5.20). Furthermore, old glass enamel samples exhibit much higher Fe and Cu content than the modern glass enamel, with a moderate amount of Co, Ni, and Zn. A substantial amount of Au could be detected in many of the samples as well, possibly coming from the

so-called Purple of Cassius. The recipe for this enamel color dates to the year 1685 and involves dissolving fine gold powder in aqua regia, adding water, and then adding a piece of pure tin. This may also explain the observed proportional dependency of Sn to Au in many of the samples.

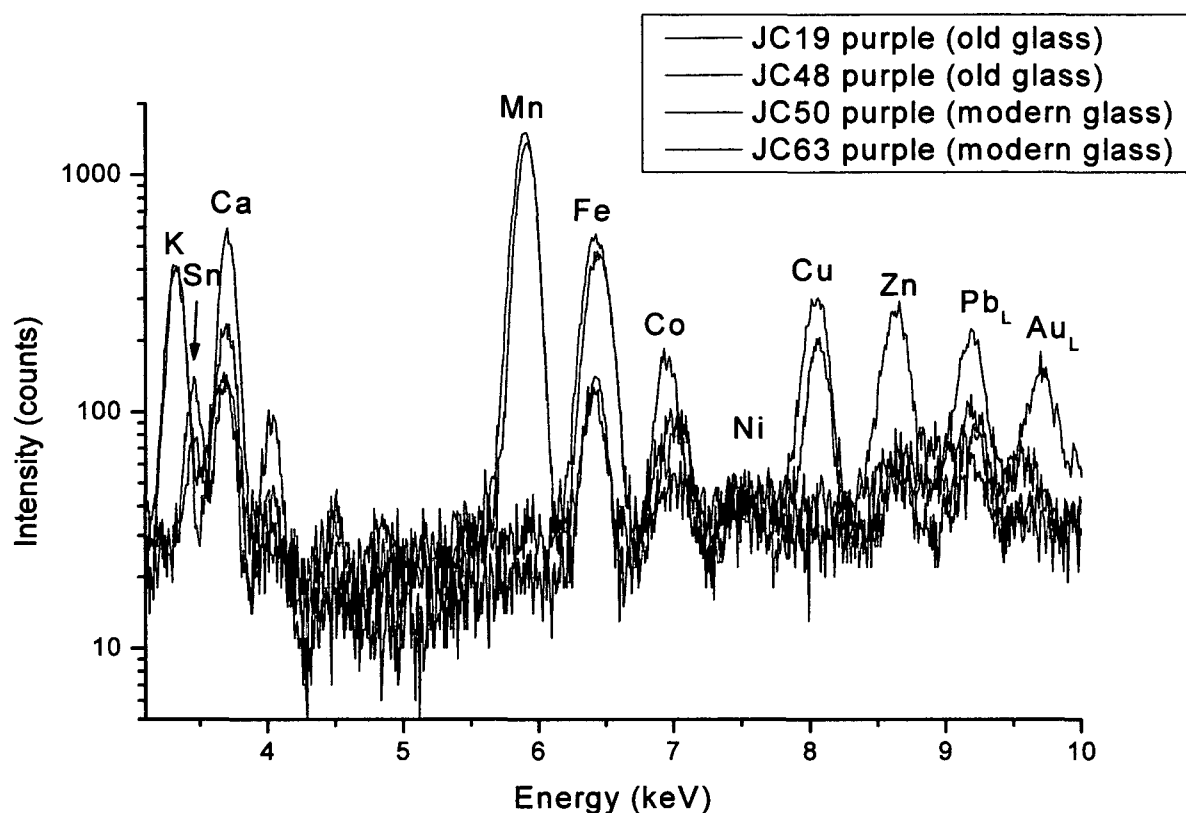


Fig. 5.20: PXRF analysis spectra of four representative 17th and 20th century glass samples (denoted old and modern, respectively), carried out on purple stained areas. In modern glass samples no Mn could be detected; Sn could be detected only in modern glasses. Furthermore, old glass enamel samples exhibit much higher Fe, Cu (and Co to some extent) content than the modern glass enamel.

Therefore, with help of the XRF analysis, it was possible to analyze qualitatively different colorants of the glass samples and to distinct between the samples regarding their chronologically different origin.

6. Summary and Conclusions

The x-ray fluorescence analysis (XRF) is regarded as one of the most appropriate analytical methods in the field of archaeometry, due to its versatility, sensitivity, acquisition quickness, and non-destructiveness. Therefore, it is widely used for various applications, yielding valuable information to conservators, archaeologists, and art historians. However, one of the downsides of conventional laboratory XRF instrumentation is that it can not be easily transported to a museum, gallery or archaeological site where the objects of interest are stored or displayed. To overcome this problem, parallel to a technological development and miniaturization of the separate components, portable XRF instrumentation suitable for field applications started emerging. The possibility of working *in situ* extended the range of use of XRF to virtually any type of an object.

Having that in mind, a portable x-ray fluorescence analyzer (PXRF) was designed and developed. The goal was to construct an instrument suitable for portable applications, yet whose spectroscopic abilities would still be comparable to those of a conventional laboratory XRF. The system is based on energy dispersive XRF and the components employed are simple, compact and lightweight, and at the same time precise, quick and with satisfactory x-ray power. The correct selection of the components when designing and building such an instrument has a crucial impact on its precision, usefulness, and of course on its techno-economical feasibility.

As a radiation source, an x-ray tube from Oxford/USA, type XRF5011, was chosen. It has a maximum power of 50 W, reached at 50 kV accelerating voltage and 1.0 mA tube current. This tube is strong enough to provide satisfactory x-ray fluorescence intensity for most applications, yet the air cooling, an important requisite for portable instrumentation, still provides enough heat dissipation for the tube to function properly. For anode material rhodium was chosen, a very good tube anode material for general purposes. When utilizing both the characteristic Rh lines and the continuum spectrum of the anode, a wide range of elements can be efficiently excited and detected.

To collimate the x-ray primary radiation a collimator using a 1.5 mm diameter pin-hole was constructed and mounted on the x-ray tube. It utilizes a system of 2 lead apertures with different diameters (4 and 1.5 mm) in order to avoid interactions of the primary beam with the inner side of the collimator, and hence secondary radiation from the cylinder material itself. Furthermore, the inside of the collimator tube is coated with a 1 mm thick aluminum foil, which, beside Al, contains mostly light elements, whose characteristic radiation practically does not affect the measurements. Additionally, between the aluminum foil and the brass tube an additional 1 mm thick lead cylinder is mounted for safety reasons. The final aperture defining the radiation beam diameter is 1.5 mm, yielding a radiation spot on a sample of a little bit over 1.5 mm in diameter.

As a pointing device and a distance controller between a sample on one side and the x-ray tube and detector on the other, a system of two lasers was applied. They are positioned in such a way, that their beam intersection coincides with the cross-point of the x-ray source and detector axes.

Due to its many advantageous features, a silicon drift detector SDD (XFlash Detector, Series 1000, from Roentec/Germany) was chosen for this application. It is small, robust, employs a LN₂-free operation and, equipped with a single Peltier element for cooling, reaches excellent energy resolution. Consequently, these features make this detection system a perfect choice for portable use. In connection with the XSVP 60 pulse processor from Roentec, it yields nominal energy resolution around 150 eV FWHM at 1 kcps for Mn K α line (5.9 keV).

The communication between single components, data acquisition, qualitative spectrum evaluation, and result presentation is established through a software package, which was developed specifically for this purpose. It is based on LabVIEW[®] development environment from National Instruments/USA. Additionally, the software was made compatible with the spectrum processing package WinAXIL[®], from Canberra Eurisys/Belgium, which can be used for subsequent quantitative evaluation.

After assembly has been completed, numerous experiments have been conducted in order to test particular components, as well as the performance of the system as a whole, i.e. components' stability tests, definition of the energy distribution for the excitation spectrum, primary beam definition, pulse processor characterization etc.

Subsequent measurements on various actual objects established this system as an excellent tool for analytical investigation of various artistic and historical objects/samples of different shape, size, age, and material. In this work several specific case studies are discussed in more detail, which demonstrated the extensive capabilities and precision of the instrument. In particular, characterization of mural paintings on the wall fragments from the St. Stephan's Cathedral in Vienna, Romanesque mural paintings in the St. Nicholas church in Winkl, wood panel lacquer decoration (lacquerware) in Schoenbrunn Castle in Vienna, and Belgian enameled stained glass fragments from the 17th century. These analytical results can be subsequently used by specialists from different fields, i.e. by art-historians for defining the origin and age of an object, by technologists for understanding the process and technique of its fabrication, and by conservators to help them modify and apply diverse conservation and restoration methods.

7. References

- [1] V. Thomsen, D. Schatzlein, *Spectroscopy* **17**(7), 2002, 14-21.
- [2] K. Janssens, R. Van Grieken, in: *Comprehensive Analytical Chemistry*, Vol. XLII (eds: K. Janssens, R. Van Grieken). Elsevier B.V., Amsterdam 2004, 1-10.
- [3] Ch. Lahanier, G. Amsel, Ch. Heitz, M. Menu, H.H. Andersen, *Nuclear Instruments and Methods in Physics Research B* **14**, 1986, 1-5.
- [4] A. Johansson, J. L. Campbell, *PIXE: A Novel Technique for Elemental Analysis*. Wiley, Chichester 1988.
- [5] A. M. Pollard, C. Heron, *Archeological Chemistry*. Royal Society of Chemistry, Cambridge, 1996.
- [6] M. H. Klaproth, *Abhandlungen der Königlichen Akademie der Wissenschaft und Schönen Künste zu Berlin, Teil Experimental-Philosophie (1792-1797)*, 1795, 3-14.
- [7] M. H. Klaproth, *Abhandlungen der Königlichen Akademie der Wissenschaft und Schönen Künste zu Berlin, Teil Experimental-Philosophie (1792-1797)*, 1795, 72-78.
- [8] M. H. Klaproth, *Abhandlungen der Königlichen Akademie der Wissenschaft und Schönen Künste zu Berlin, Teil Experimental-Philosophie (1798-1800)*, 1798, 31-40.
- [9] H. Raehlmann, *Über die Maltechnik der Alten mit besonderer Berücksichtigung der Römisch-Pompejanischen Wandmalerei*. Dissertation Thesis, Berlin, 1910.
- [10] A. P. Laurie, *Analyst* **58**, 1933, 468.
- [11] A. Eibner, *Mouseion* **29-30**, 1935, 113.

- [12] R. J. Gettens, *Technical Study in Field Fine Arts* **5**, 1936, 18.
- [13] H. Malissa, *Mikrochemie* **35**, 1950, 302.
- [14] J. Plesters, *Studies in Conservation* **2**, 1956, 110.
- [15] H.-P. Schramm, B. Hering, *Historische Malmaterialien und ihre Identifizierung*. VEB Deutscher Verlag der Wissenschaften, Berlin 1989.
- [16] F. Feigl, *Spot Tests in Inorganic Analysis*. Elsevier, Amsterdam 1954.
- [17] F. Feigl, *Spot Tests in Organic Analysis*. Elsevier, Amsterdam 1954.
- [18] H. G. J. Moseley, *Philosophical Magazine* **26**, 1913, 1024-1034.
- [19] W. D. Coolidge, *Physical Review* **2**, 1913, 409-430.
- [20] D. Coster, G. von Hevesy, *Nature* **111**, 1923, 182.
- [21] H. Geiger, W. Müller, *Physics Z* **29**, 1928, 839-841.
- [22] H. Friedman, L. S. Birks, *Review of Scientific Instruments* **19**, 1948, 323-330.
- [23] F. X. Spiegel, E. Horowitz, *Instruments for the Sorting and Identification of Scrap Metal*. Center for Material Research, The Johns Hopkins University, Baltimore 1981.
- [24] J. M. Jaklevic, F. S. Goulding, *IEEE Transactions on Nuclear Science* **NS-19**, 1972, 384-389.
- [25] S. Bichlmeier, *Entwicklung, Bau und Test einer kompakten Mikro-Röntgenfluoreszenzsonde*. Thesis, Technische Universität Darmstadt, 2000.

- [26] R. G. Johnson, B.-S. L. King, in: *Methods for Geochemical Analysis* (ed.: P. A. Baedecker), U.S. Geological Survey Professional Paper 1770, 1987, F1-F5.
- [27] K. Linden, N. Strafelt, *Arkiv Fysik* **7**, 1953, 193.
- [28] J. R. Rhodes, T. Florkowski, J. F. Cameron, Determination of Sulfur and Cobalt in Hydrocarbons using a $^{147}\text{Pm}/\text{Al}$ Bremsstrahlung Source. U.K.A.E.A. Research Group Report No. AERE-R3925, Harwell 1962.
- [29] C. G. Clayton (ed.), *Radioisotope X-Ray Fluorescence Spectrometry – Report of a Panel held in Vienna, Austria, 1968*, IAEA, Vienna 1970, Technical Report Series No. 115.
- [30] H. Sipila, *Nuclear Instruments and Methods in Physics Research* **133**, 1976, 251.
- [31] P. F. Berry, G. R. Voots, in: *Non-Destructive Testing*, (eds.: J. Boogaard, G.M. Van Dijk), Elsevier Science Publishers, Amsterdam 1989, 737-742.
- [32] R. Cesareo, G. E. Gigante, A. Castellano, *Nuclear Instruments and Methods in Physics Research A* **428**, 1999, 171-181.
- [33] R. Cesareo, A. Castellano, C. Fiorini, G. E. Gigante, J. S. Iwanczyk, A. Longoni, J. A. Pantazis, J. L. P. Chapa, M. A. Rosales, *SPIE--The International Society for Optical Engineering* **3115**(Hard X-Ray and Gamma-Ray Detector Physics, Optics, and Applications), 1997, 274-283.
- [34] G. Vittiglio, K. Janssens, B. Vekemans, F. Adams, A. Oost, *Spectrochimica Acta B* **54**, 1999, 1697-1710.
- [35] A. Loupilov, A. Sokolov, V. Gostilo, *Radiation Physics and Chemistry* **61**, 2001, 463-464.
- [36] A. K. Khusainov, T. A. Antonova, S. V. Bahlanov, A. V. Derbin, V. V. Ivanov, V. V. Lysenko, F. Morozov, V. G. Mouratov, V. N. Muratova, Y. A. Petukhov, A. M. Pirogov, O.

P. Polytsia, V. D. Saveliev, V. A. Solovei, K. A. Yegorov and M. P. Zhucov, *Nuclear Instruments and Methods in Physics Research A* **428**(1), 1999, 223-231.

[37] M. Al-Turany, J. D. Meyer, K. Bethge, *Nuclear Instruments and Methods in Physics Research B* **155**(1-2), 1999, 137.

[38] K. Sato, *Nuclear Instruments and Methods in Physics Research A* **436**(1-2), 1999, 285.

[39] A. V. Golubev, E. G. Pivinskii, V. V. Akulinichev, A. A. Sorokin, S. V. Bobashev, *Technical Physics* **44**(5), 553.

[40] N. Ota, T. Murakami, M. Sugizaki, M. Kaneda, T. Tamura, H. Ozawa, T. Kamae, K. Makishima, T. Takahashi, M. Tashiro, Y. Fukazawa, J. Kataoka, K. Yamaoka, S. Kubo, C. Tanihata, Y. Uchiyama, K. Matsuzaki, N. Iyomoto, M. Kokubun, T. Nakazawa, A. Kubota, T. Mizuno, Y. Matsumoto, N. Isobe, Y. Terada, M. Sugiho, T. Onishi, H. Kubo, H. Ikeda, M. Nomachi, T. Ohsugi, M. Muramatsu and H. Akahori, *Nuclear Instruments and Methods in Physics Research A* **436**(1-2), 1999, 291.

[41] A. C. Huber, J. A. Pantazis, V. Jordanov, *Nuclear Instruments and Methods in Physics Research B* **99**, 1995, 665.

[42] E. Gatti, P. Rehak, *Nuclear Instruments and Methods in Physics Research A* **225**, 1984, 608.

[43] P. Leutenegger, A. Longoni, C. Fiorini, L. Strüder, J. Kemmer, P. Lechner, S. Sciuti, R. Cesareo, *Nuclear Instruments and Methods in Physics Research A* **439**, 2000, 458-470.

[44] P. Lechner, C. Fiorini, R. Hartmann, J. Kemmer, N. Krause, P. Leutenegger, A. Longoni, H. Soltan, D. Stötter, R. Stötter, L. Strüder, U. Weber, *Nuclear Instruments and Methods in Physics Research A* **458**, 2001, 281-287.

[45] A. Longoni, C. Fiorini, P. Leutenegger, S. Sciuti, G. Fronterotta, L. Strüder, P. Lechner, *Nuclear Instruments and Methods in Physics Research A* **409**, 1998, 407-409.

- [46] C.Fiorini, A. Longoni, *IEEE Transactions on Nuclear Science* **46**(6), 1999, 2011-2016.
- [47] S. Piorek, *Field Analytical Chemistry & Technology* **1**(6), 1997, 317-329.
- [48] O. Hahn, W. Malzer, B. Kanngieser, B. Beckhoff, *X-Ray Spectrometry* **33**, 2004, 234-239.
- [49] R. Cesareo, G. E. Gigante, P. Canegallo, A. Castellano, J. S. Iwanczyk, A. Dabrowski, *Nuclear Instruments and Methods in Physics Research A* **380**, 1996, 440-445.
- [50] A. Castellano, R. Cesareo, *Nuclear Instruments and Methods in Physics Research B* **129**, 1997, 281-283.
- [51] K. Sugihara, K. Tamura, M. Satoh, Y. Hayakawa, Y. Hirao, S. Miura, H. Yotsutsuji, Y. Tokugawa, *Advances in X-Ray Analysis* **44**, 2001, 432-441.
- [52] R. Cesareo, *Nuclear Instruments and Methods in Physics Research B* **211**, 2003, 133-137.
- [53] J. L. Ferrero, C. Roldan, M. Ardid, E. Navarro, *Nuclear Instruments and Methods in Physics Research A* **422**, 1999, 868-873.
- [54] J. L. Ferrero, C. Roldan, D. Juanes, C. Morera, E. Rollano, *Advances in X-Ray Analysis* **44**, 2001, 425-430.
- [55] Z. Szökefalvi-Nagy, I. Demeter, A. Kocdonya, I. Kovacs, *Nuclear Instruments and Methods in Physics Research B* **226**, 2004, 53-59.
- [56] P. Moioli, C. Seccaroni, *X-Ray Spectrometry* **29**, 2000, 48-52.
- [57] A. K. Karydas, D. Kotzamani, R. Bernard, J. N. Barrandon, Ch. Zarkadas, *Nuclear Instruments and Methods in Physics Research B* **226**, 2004, 15-28.

- [58] R. Cesareo, A. Castellano, G. Buccolieri, M. Marabelli, *Nuclear Instruments and Methods in Physics Research B* **155**(3), 1999, 326.
- [59] J. L. Ferrero, C. Roldan, E. Navarro, M. Ardid, M. Marzal, J. Almirante, P. Ineba, J. Vergara, C. Mata, *Journal of Radioanalytical Nuclear Chemistry* **240**(2), 1999, 523.
- [60] W. A. Oddy, *Archaeometry* **14**, 1972, 1.
- [61] P. D. C. Brown, F. Schweizer, *Archaeometry* **15**, 1973, 2.
- [62] E. T. Hall, F. Schweizer, P. A. Toller, *Archaeometry* **15**, 1973, 53.
- [63] R. Woldseth, X-Ray Energy Spectrometry. Kevex Corporation, Burlingame 1977.
- [64] J. E. Fernandez, in: Microscopic X-Ray Fluorescence Analysis, (eds: K. Jansens, F. Adams, A. Rindby), John Wiley & Sons, Chichester 2000, 17-62.
- [65] M. Mantler, *Progress in Crystal Growth Characterization* **14**, 1987, 213
- [66] R. Jenkins, J. L. de Vries, Practical X-Ray Spectrometry. Macmillan, London 1969.
- [67] G. Anderman, J. W. Kemp, *Analytical Chemistry* **30**, 1958, 1306-1309.
- [68] M. Mantler, M. Schreiner, *X-Ray Spectrometry* **29**, 2000, 3-17.
- [69] G. R. Lachance, R. Traill, *Canadian Spectroscopy* **11**, 1966, 43-48.
- [70] S. D. Rasberry, K. F. J. Heinrich, *Analytical Chemistry* **46**, 1974, 81-89.
- [71] H. J. Lucas-Tooth, C. Pyne, Advances in X-Ray Analysis. Plenum Press, New York 1968, 7.

- [72] W. K. deJongh, *X-Ray Spectrometry* **2**, 1973, 151-158.
- [73] R. M. Rousseau, *X-Ray Spectrometry* **113**, 1984, 115-120.
- [74] J. W. Criss, L. S. Birks, *Analytical Chemistry* **40**, 1968, 1080-1086.
- [75] M. Mantler, *Advances in X-Ray Analysis* **41**, 1999. CD-ROM by ICDD, Newton Square, PA 19073-3273 USA.
- [76] M. Mantler, M. Schreiner, *Journal of Radioanalytical and Nuclear Chemistry* **247**(3), 2001, 635-644.
- [77] P. J. Potts, *A Handbook of Silicate Rock Analysis*. Blackie, Glasgow and London 1992.
- [78] M. Mantler, J. Klikovits, *Advances in X-Ray Analysis* **47**, 2004. CD-ROM by ICDD, Newton Square, PA 19073-3273 USA.
- [79] J. Lutz, E. Pernicka, *Archaeometry* **38**, 1996, 313-323.
- [80] M. Ferretti, L. Miazzo, P. Moiola, *Studies in Conservation* **42**, 1997, 241-246.
- [81] C. Caneva, M. Ferretti, Proceedings CD, 15th World Conference on Non-destructive Testing, Roma (Italy), 15-21 October 2000.
- [82] D. E. Leyden, *Fundamentals of X-Ray Spectrometry as Applied to Energy Dispersive Techniques*. Tracor Xray Incorporated, California 1984.
- [83] M. Milazo, C. Cicardi, *X-Ray Spectrometry* **26**, 1997, 211.
- [84] Y. Hosokawa, S. Ozawa, H. Nakazawa, T. Nakayama, *X-Ray Spectrometry* **26**, 1997, 380.

- [85] K. Larsson, P. Engstrom, A. Rindby, B. Stocklassa, *Advances in X-Ray Analysis* **33**, 1990, 623.
- [86] K. Janssens, B. Vekemans, L. Vincze, F. Adams, A. Rindby, *Spectrochimica Acta B* **51**, 1996, 1661.
- [87] S. Bichlmeier, K. Janssens, J. Heckel, D. Gibson, P. Hoffmann, H. M. Ortner, *X-Ray Spectrometry* **30**, 2001, 8-14.
- [88] M. C. Nichols, D. Boehme, R. Ryon, D. Wherry, B. Cross, G. Aden, *Advances in X-Ray Analysis* **30**, 1987, 45.
- [89] D. R. Boehme, *Advances in X-Ray Analysis* **30**, 1987, 39.
- [90] M. C. Nichols, R. W. Ryon, *Advances in X-Ray Analysis* **29**, 1986, 423.
- [91] W. H. McMaster, N. Kerr Del Grande, J. H. Mallet, J. H. Hubbell, *Compilation of X-Ray Cross Sections*. Lawrence Radiation Laboratory, California 1969.
- [92] A. T. Ellis, M. Holmes, P. Kregsamer, P. J. Potts, Ch. Streli, M. West, P. Wobrasuchek, *Journal of Analytical Atomic Spectrometry* **13**, 1998, 209R-232R.
- [93] P. J. Potts, A. T. Ellis, M. Holmes, P. Kregsamer, Ch. Streli, M. West, P. Wobrasuchek, *Journal of Analytical Atomic Spectrometry* **15**, 2000, 1417-1442.
- [94] P. J. Potts, A. T. Ellis, P. Kregsamer, J. Marshall, Ch. Streli, M. West, P. Wobrasuchek, *Journal of Analytical Atomic Spectrometry* **16**, 2001, 1217-1237.
- [95] J. Kemmer, G. Lutz, E. Belau, U. Prechtel, W. Welser, *Nuclear Instruments and Methods in Physics Research A* **253**, 1987, 378-381.
- [96] F. He, P. J. Van Espen, *Analytical Chemistry* **63**, 1991, 2237-2241.
- [97] R. A. Vane, *Advances in X-Ray Analysis* **26**, 1983, 369.

APENDIX A

Analysis Software Manual

A.1. About this manual

This manual is for the user of the portable XRF (PXRF) instrument, developed at the Institute of Science and Technology in Art, Academy of Fine Arts in Vienna, in 2004. It explains the main features of the software and gives some insight into the theory behind particular steps. It should be useful to newcomers as well as to experienced users. In easy cases it will assist in solving problems, which may appear during the application of the instrument.

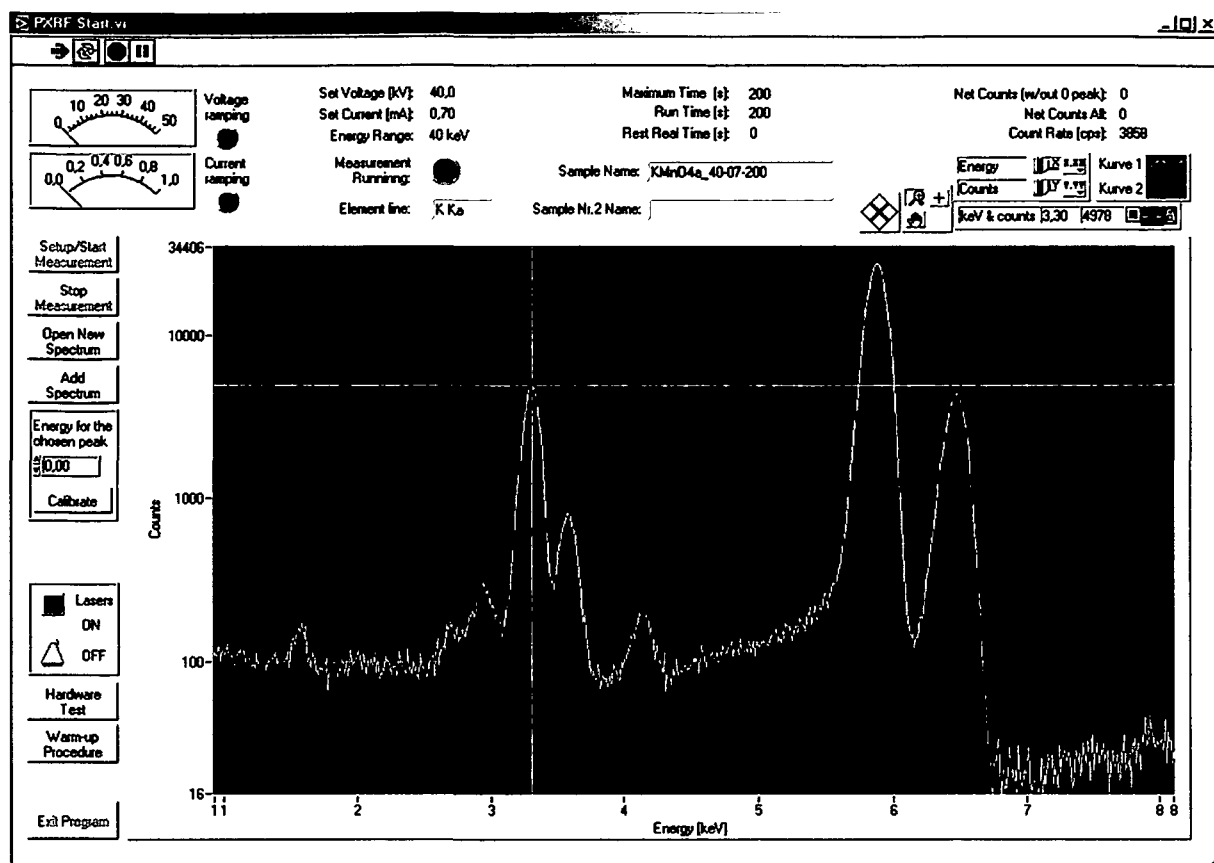
The following procedures are performed by the instrument and will be separately discussed in this manual:

- Measurement setup
- Measurement sequence
- Spectrum analysis
- Hardware test

Additionally, Chapter A.6 gives an overview of some important syntax commands, which might be useful when communicating manually via serial interface. Chapters A.7 – A.9 give a more detailed explanation of the LabVIEW development software as well as charts of data flow and functions used in the PXRF software.

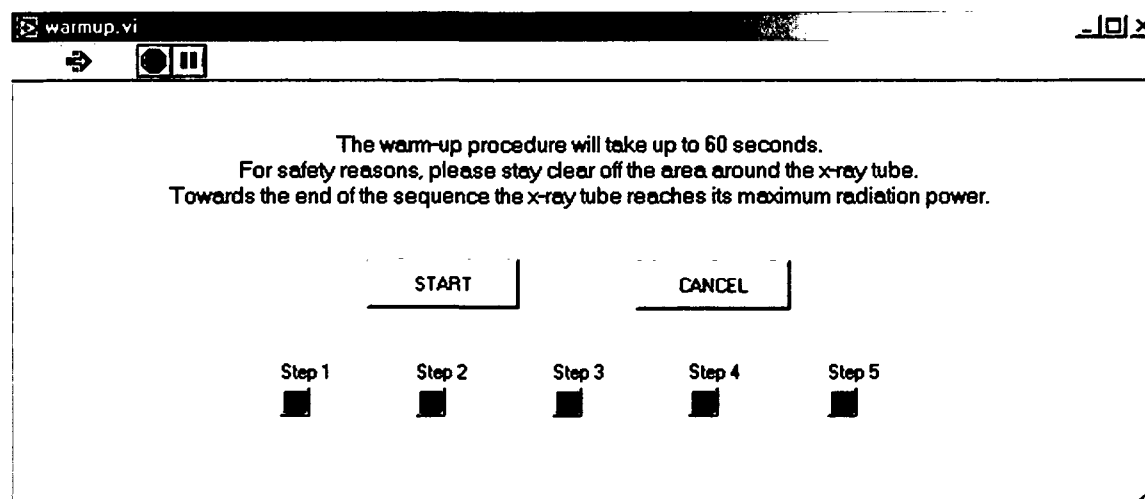
A.2. Measurement setup

When the program is started, the *main window* is displayed. From this window all the measurements are started and managed. Furthermore, it allows verification of the instrumental and measuring conditions, as well as monitoring of information relevant for data acquisition (DAQ) during a measurement. Special functions and particular buttons in the *main window* will be explained throughout the manual.



Warm-up procedure

In case the x-ray tube has not been used for a prolonged period of time (several weeks) it is recommended to carry out a warm-up procedure. It takes 60 seconds and is fully automatic. By clicking on the *Warm-up Procedure* button the *warm-up procedure dialogue window* is activated:

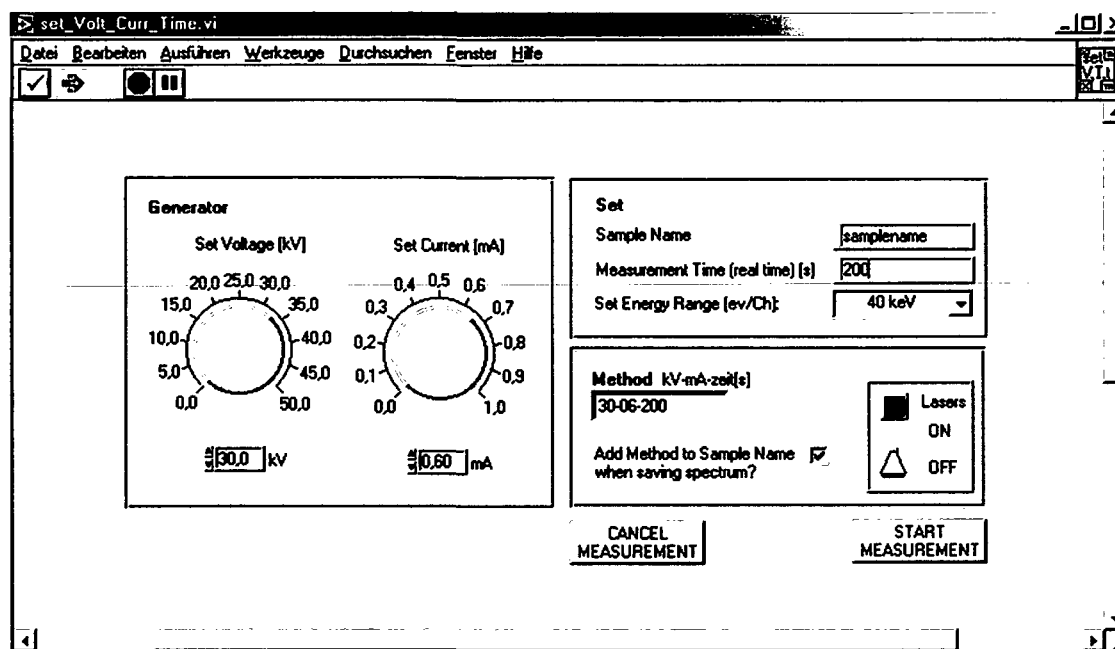


To start the sequence, click the *Start* button. You can cancel it any time by clicking the *Cancel* button. The sequence stops automatically after ca. 60 seconds

Setup/Start
Measurement

When starting a measurement, the *Setup/Start Measurement* button is selected.

This will open the *measurement set-up window*:



This option allows setting of the following parameters:

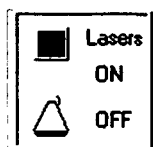
- x-ray tube acceleration voltage (0.5 - 50 kV)
- tube current (0.05 – 0.99 mA)
- measurement time (in seconds)
- sample name

X-ray tube acceleration voltage and tube current are set either by turning the knobs or by entering the exact numerical values, and the measurement time and sample name are set by typing in the values using a keyboard.

Method is a code of three values, which is displayed automatically when the above mentioned parameters are chosen. It defines the measurement conditions and is internally stored with the obtained spectrum for a given measurement. Its number sequence *n1-n2-n3* corresponds to the

values of acceleration voltage, tube current and measurement time, respectively, which were previously set. For example, 30-06-200 means the measurement will be carried out with 30 kV acceleration voltage, 0.6 mA tube current, and 200 s measurement time.

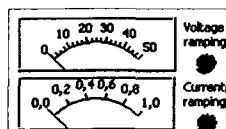
The *sample name* does not have to be unique, but it should help to identify the samples. By checking the box next to "*Attach method to the sample name?*" it can be chosen to include the method of the measurement together with the sample name when saving the spectrum. In that case the spectrum will be saved as: *samplename_method.PXR*.



By clicking on the *Lasers ON/OFF* switch the lasers are turned on and off. The red light indicates the lasers are switched on. The point to be analysed can now be chosen, and a proper position of the measuring head set.

When the parameters and the point of investigation have been chosen, the measurement can be started by clicking the *Start Measurement* button. In case the *Cancel* button is clicked, the *main window* is reopened – the measurement does not start and the previously entered measurement parameters are erased. For guidance and suggestions on choosing the instrumental conditions and measurement parameters please see Chapter 4.

A.3. Measurement sequence



When the *Start Measurement* button in the *measurement set-up window* is clicked on, the measurement does not start immediately. The accelerating voltage and the tube current first have to be ramped up to the pre-set working conditions and only then the data acquisition starts. During the ramping period the corresponding two red lamps are lit.



The lit green light in the *main window* indicates that the measurement is running. At this time special attention should be given to the safety precautions, ensuring the adequate x-ray radiation shielding and clearing the persons from around the area of investiga-

tion. The obtained spectrum is displayed in the window after the measurement has been completed.

During a measurement the *main window* allows verification of the instrumental and measuring conditions, as well as monitoring of information relevant for data acquisition, i.e. net counts with and without the influence of zero peak, count rate, energy range of the detector etc.



A measurement sequence can be stopped any time during measurement with a mouse click on a *Stop Measurement* button in the *main window*.

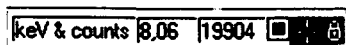
When DAQ is completed, the measurement sequence is finished automatically. The green light turns off and ramping down of the tube voltage and current occurs. During this time the red lamps are lit. After this procedure is finished and the red lights turn off, the sound signal informs the user that the x-ray tube has been shut down and the interlock is off. The measurement is complete and it is safe again to handle the measurement head and the object which was under investigation.

A dialogue box "Save Spectrum" appears, prompting a user to save the spectrum. The file's name can be here verified again, and altered if needed.

A.4. Spectrum analysis

More or less simultaneously to appearance of the "Save Spectrum" dialogue, the measured spectrum is displayed in the *main window*.

When a spectrum is displayed the x- and y-scales (energy and intensity scale, respectively) are adjusted automatically to accommodate the whole plot. This behaviour is called autoscaling. Turn autoscaling on or off by right-clicking the graph and selecting *X Scale» Autoscale X* or *Y Scale»Autoscale Y* from the shortcut menu. By default, autoscaling is enabled for graphs.



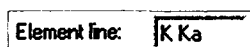
Cursors on graphs allow reading the exact value of a point on a plot. The cursor values are displayed in the cursor legend, shown at left. The left numerical value corresponds to the energy in keV, and the right one to the intensity in counts. Use the *Lock* button (shown furthest right on the cursor legend) to lock and unlock the cursor onto a plot, and to choose the plot which is followed by the cursor (in case of two plots). Click on the cursor sign (second from right) to define the starting position of the cursor, its style, and color.



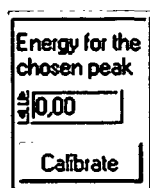
The scale legend is used to label scales and configure scale properties. To configure the format, precision and mapping mode of the energy and intensity scale, click on the *X.XX* and *Y.YY* button, respectively, and choose from the drop-down menu. Clicking on the *X-Scale* and on the *Y-Scale* button autoscales the x- and y-axis, respectively, showing the whole spectrum data set.



Use the *Cursor Mover* (four squares) to move the cursor by clicking on the squares showing the desired direction. By clicking on the *Cursor* button (top right) a mouse can be used to move the cursor. By clicking on the *Plot View* button (second from right, top row) different options for displaying the plot in the graph can be chosen from. Use the *Hand* button to grab-and-move the plot around.

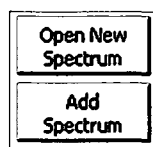


When going over the spectrum peaks with a cursor, the names of the elements and their characteristic lines are displayed. Not all the elements are displayed, and due to possible errors through automatic calibration, this data should be used only as guide-lines.



The spectrum intensity data obtained from a spectrometer is sorted according to their energies and the entire range is divided into a certain number of intervals, i.e. channels. For a more convenient display of the spectrum this channel number is converted to energy units by calibration. An internal sequence calibrating each spectrum is implemented in

the software, but there may be cases where the automatic calibration error is too big, thus impeaching the analysis. In that case the calibration sequence can be carried out manually: Place the cursor on a peak with a known energy and type its energy in the field above the *Calibrate* button. Press the *Calibrate* button and the calibration will be carried out.



To open a new spectrum from a file, click the *Open New Spectrum* button. The spectrum is displayed in the *main window* and its name is displayed in the *Sample Name* field. To overlap another spectrum, click the *Add Spectrum* button. The second spectrum is displayed and its name is displayed in the *Sample No. 2 Name* field.



The spectra are displayed in different colors and the *Spectrum Color Indicator* indicates which spectrum corresponds to which sample name.

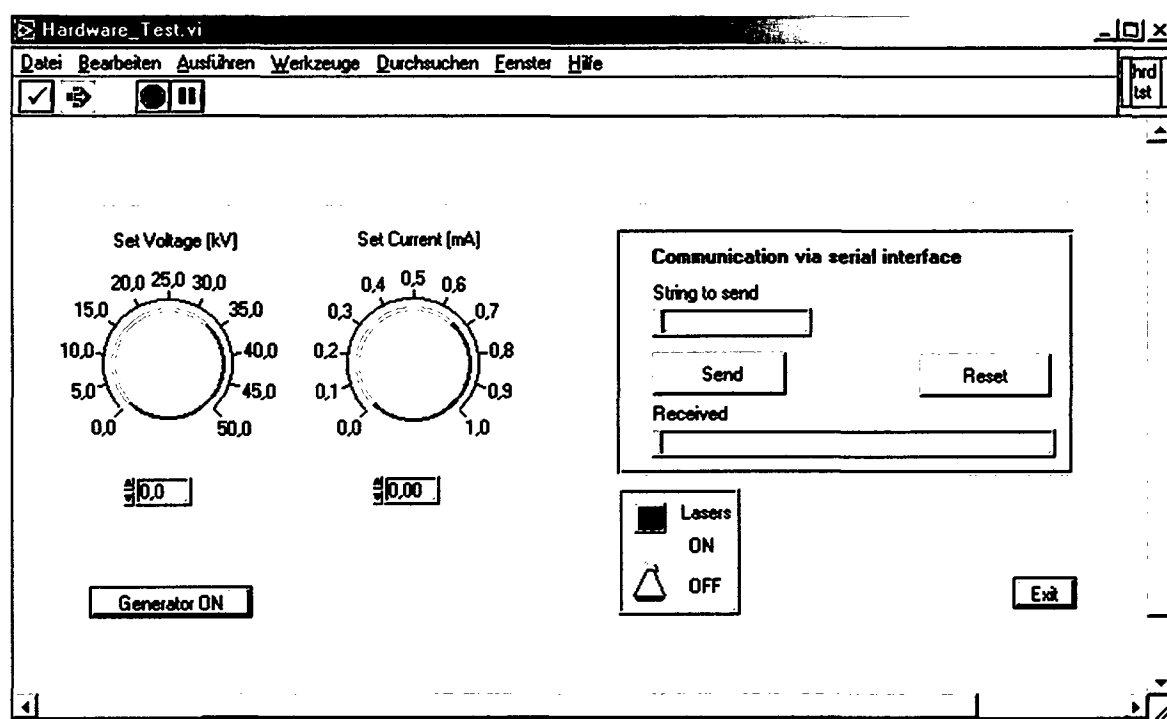
Further analysis of the spectra obtained with the PXRf can be carried out with any other analytical software which supports data saved in ASCII format, e.g. WinAxil, Origin etc. When converting the channels into energy (x-axis) it should be kept in mind that the zero peak center has an offset x_0 of 96 channels. Furthermore, a correction by a gain factor dx , dependent on the channel number and on the detector energy range, has to be carried out. E.g. for 4096 channels and the detector energy range of 40 keV the gain is 0.0100756. Thus, when importing spectrum data into Origin, the x-column values would be set as:

$$\text{Col(A)} = (i-96) * 0.0100756.$$

A.5. Hardware test



To test the hardware and communication between single components of the PXRF the *hardware test window* can be opened by clicking with a mouse on the *Hardware Test* button. This will open a new sub-window and allow testing of several instrument features.



Under this test sequence the high voltage power supply (HVPS) can be turned on without having to start a measurement, by clicking the *Generator ON* button. The voltage and current can be varied continuously and the set parameters can be checked using a voltmeter at the generator itself (please see HVPS manual).

Proper functioning of the lasers can be tested as well, by switching the *Lasers ON/OFF* switch.

To test the software communication capabilities via serial interface a dialogue box for sending and receiving of command strings has been set. Clicking on the *Send* button will send a string, clicking on the *Reset* button will reset the spectrometer system software (equivalent of send-

ing a *###* string). Section A.6. gives a list of some important syntax commands, which might be needed during a testing phase.

By clicking on the *Exit* button the *hardware test window* is closed and the *main window* is displayed again.

Once in the *main window*, lasers can be turned on and off any time by switching the *Lasers ON/OFF* switch.



To exit the program, click on the *Exit Program* button.

A.6. Syntax commands

The following list displays some important syntax commands, which might be useful when communicating manually via serial interface. All time values are given in milliseconds.

Sent command	Received answer	Description of the command	Notes
\$\$\$		Reset spectrometer software	
\$OK	!OK	Send system time (time since the program start)	
\$CC	!CC	Erase spectrum	
\$CT	!CT	Set counter cycle time	Standard: 1000 ms
\$TC	!TC	Ask cycle time	
\$BC	!BC	Ask brut count rate	In case CT = 1000, BC is given in cps
\$NC	!NC	Ask net count rate	In case CT = 1000, NC is given in cps
\$MS	!MS	Ask measuring time (real time)	
\$LS	!LS	Ask measuring time (live time)	
\$MR	!MR	Ask rest of measuring time (real time)	
\$LR	!LR	Ask rest of measuring time (live time)	
\$MT time	!MT	Set measuring time (real time) and start measurement	"time" = 0.....4204067295
\$LT time	!LT	Set measuring time (live time) and start measurement	"time" = 0.....4204067295
\$MP cmd	!MP	Pause	"cmd" = ON or NO, meaning start or stop measurement

\$SS start channel, step size, sum value, d max value	!SS hi(1) lo(1) hi(2) lo(2) ... lo(d value) or: !SS hi(1) mh(1) ml(1) lo(1) ... lo(d value)	Copy spectrum in buffer, possibly erase, and send buffer	"start channel", "d max value" = 0...4095 "step size", "sum value" = 0...4096
\$SR start channel, step size, sum value, d max value	!SR hi(1) lo(1) hi(2) lo(2) ... lo(d value) or: !SR hi(1) mh(1) ml(1) lo(1) ... lo(d value)	Send spectrum buffer again	"start channel", "d max value" = 0...4095 "step size", "sum value" = 0...4096
\$SM format mode	!SM	Set sending mode for SS/SR commands	<ul style="list-style-type: none"> • "format" = 2 2 byte/channel, floating (eeeemmmm mmmmmmmm); value=m*2^e • "format" = 4 4 byte/channel, longint (hhhhhhhh llllllll) • "mode" = 0 accumulate spectrum • "mode" = 1 send parts of spectrum as soon as received
\$SE e	!SE	Set amplifier energy range	"e" = 0: 10 keV = 1: 20 keV = 2: 40 keV = 3: 80 keV
\$FE	!SE e	Ask amplifier energy range	"e" = 0: 10 keV = 1: 20 keV = 2: 40 keV

			= 3: 80 keV
\$FC	!FC offs gain	Ask energy calibration data	“offs” = 100*(zero channel) “gain” = 10000*eV/channel $E(k) = 0,0001\text{eV} \cdot (k - 0,01 \cdot \text{offs}) \cdot \text{gain}$
\$XR1_ON	!XR1_ON	Turn on laser 1 & 2	
\$XR1OFF	!XR1OFF	Turn off laser 1 & 2	
\$XR2_ON	!XR2_ON	Turn on output 2	
\$XR2OFF	!XR2OFF	Turn off output 2	
\$HVP_ON	!HVP_ON	Turn on interlock contact	Allows turning on the x-ray tube
\$HVPOFF	!HVPOFF	Turn off interlock contact	Prohibits turning on the x-ray tube
\$HVI n1 n2 n3	!HVI385	Set current output to 0,385	n1, n2, n3 – three digits of a number
\$HVU n1 n2 n3	!HVU125	Set voltage output to 12,5 kV	n1, n2, n3 – three digits of a number
\$HV???I	!HV???I (e.g. 0.385mA)	Send readings about measured current	7 ASCII character sequence, i.e. 0 . n1 n2 n3 mA
\$HV???U	!HV???U (e.g. 12.5kV)	Send readings about measured voltage	7 ASCII character sequence, first (and others for values under 10) is always blank (blank, ASCII code 32) i.e. bl n1 n2 . n3 kV

The complete syntax command list can be found in the manual “Standardinterface RCL 2.2 Referenchandbuch” (in German language), from the Roentec XFlash 1000 spectrometer manual.

A.7. LabVIEW Overview

LabVIEW is a graphical programming language of National Instruments¹, USA, that uses icons instead of lines of text to create applications. In contrast to text-based programming languages, where instructions determine program execution, LabVIEW uses dataflow programming, where the flow of data determines execution. In LabVIEW, you build a user interface by using a set of tools and objects. The user interface is known as the front panel. You then add code using graphical representations of functions to control the front panel objects. The block diagram contains this code. In some ways, the block diagram resembles a flowchart.

LabVIEW programs are called virtual instruments, or VIs, because their appearance and operation imitate physical instruments, such as oscilloscopes and multimeters. Every VI uses functions that manipulate input from the user interface or other sources and display that information or move it to other files or other computers.

A VI contains the following three components:

- **Front panel** — Serves as the user interface.
- **Block diagram** — Contains the graphical source code that defines the functionality of the VI.
- **Icon and connector pane** — Identifies the VI so that you can use the VI in another VI. A VI within another VI is called a subVI. A subVI corresponds to a subroutine in text-based programming languages.

LabVIEW includes extensive documentation for new and experienced LabVIEW users. With help of the documentation listed below it should be possible to solve most of the problems when modifying or upgrading the PXRF software. For updated documentation resources refer to the National Instruments Product Manuals Library at www.ni.com.

- **LabVIEW Bookshelf** — Use this PDF to search PDF versions of all the LabVIEW manuals and Application Notes. Access the *LabVIEW Bookshelf* by selecting **Help»Search the LabVIEW Bookshelf**.

¹ Version 6i, License G12X06537, Copyright 2000 National Instruments, <http://www.ni.com/labview/>

• **Getting Started with LabVIEW** — Use this manual to familiarize yourself with the LabVIEW graphical programming environment and the basic LabVIEW features you use to build data acquisition and instrument control applications.

• **LabVIEW Tutorial** — Use this tutorial to learn basic LabVIEW concepts. The tutorial guides you through several activities to familiarize you with graphical programming. Access the *LabVIEW Tutorial* by selecting **Help»VI, Function, and How-To Help** or by clicking the **LabVIEW Tutorial** button in the LabVIEW dialog box.

• **LabVIEW Quick Reference Card** — Use this card to get started with LabVIEW quickly. The card describes the LabVIEW palettes and general editing, wiring, and debugging techniques.

• **LabVIEW User Manual** — Use this manual to learn about LabVIEW programming concepts, techniques, features, VIs, and functions you can use to create test and measurement, data acquisition, instrument control, data logging, measurement analysis, and report generation applications.

• **LabVIEW Help** — Use this help file as a reference for information about LabVIEW palettes, menus, tools, VIs, and functions. The *LabVIEW Help* also includes step-by-step instructions for using LabVIEW features. Access the *LabVIEW Help* by selecting **Help»VI, Function, and How-To Help**. The *LabVIEW Help* includes links to the following resources:

– *LabVIEW Tutorial*

– *LabVIEW Bookshelf*, which includes PDF versions of all the LabVIEW manuals and Application Notes

– Technical support resources on the National Instruments Web site, such as the Developer Zone, the Knowledge Base, and the Product Manuals Library

• **LabVIEW Measurements Manual** — Use this manual to learn more about building data acquisition and instrument control applications in LabVIEW. If you are a new LabVIEW user, read the *Getting Started with LabVIEW* manual and the *LabVIEW User Manual* before you read this manual.

- **LabVIEW Development Guidelines** — Use this manual to learn how to build VIs that are easy to understand, use, and revise. The manual describes project tracking, design, and documentation techniques.
- **LabVIEW Application Notes** — Use the LabVIEW Application Notes to learn about advanced or specialized LabVIEW concepts and applications. Refer to the NI Developer Zone at ni.com for new and updated Application Notes.
- **LabVIEW VXI VI Reference Manual** — Use this manual to learn about the hardware VXI VIs for LabVIEW. This manual is a companion guide to the *NI-VXI Programmer Reference Manual* that comes with the VXI hardware.

A.8. Functional Structures of the PXRF Software

This part of the appendix gives an overview of the structure and the VIs used in the PXRF control and analyzing software. For more detailed explanation of the LabVIEW specific code instructions and commands please refer to the LabVIEW documentation resources.

The main block diagram consists of four *sequence structures*², which define the main course of the program. The first sequence is where the program is being run from, the second and third serve a safety purpose, making sure that when exiting the software the lasers and the high voltage interlock are turned off. The forth one is a spare. Fig. A.1 shows the first sequence, and the subsequences and subroutines within it.

All commands from the first sequence structure are placed inside a *while loop*³, which runs as long as the sequence is running. From there the measurements can be set up and started, lasers can be turned on and off, hardware test and warm up sequence can be started, spectra can be opened and laid one over another, and the energy scale for existing spectra can be calibrated.

² Sequence structure — contains one or more subdiagrams, which execute in sequential order.

³ While Loop — executes a subdiagram until a condition is met.

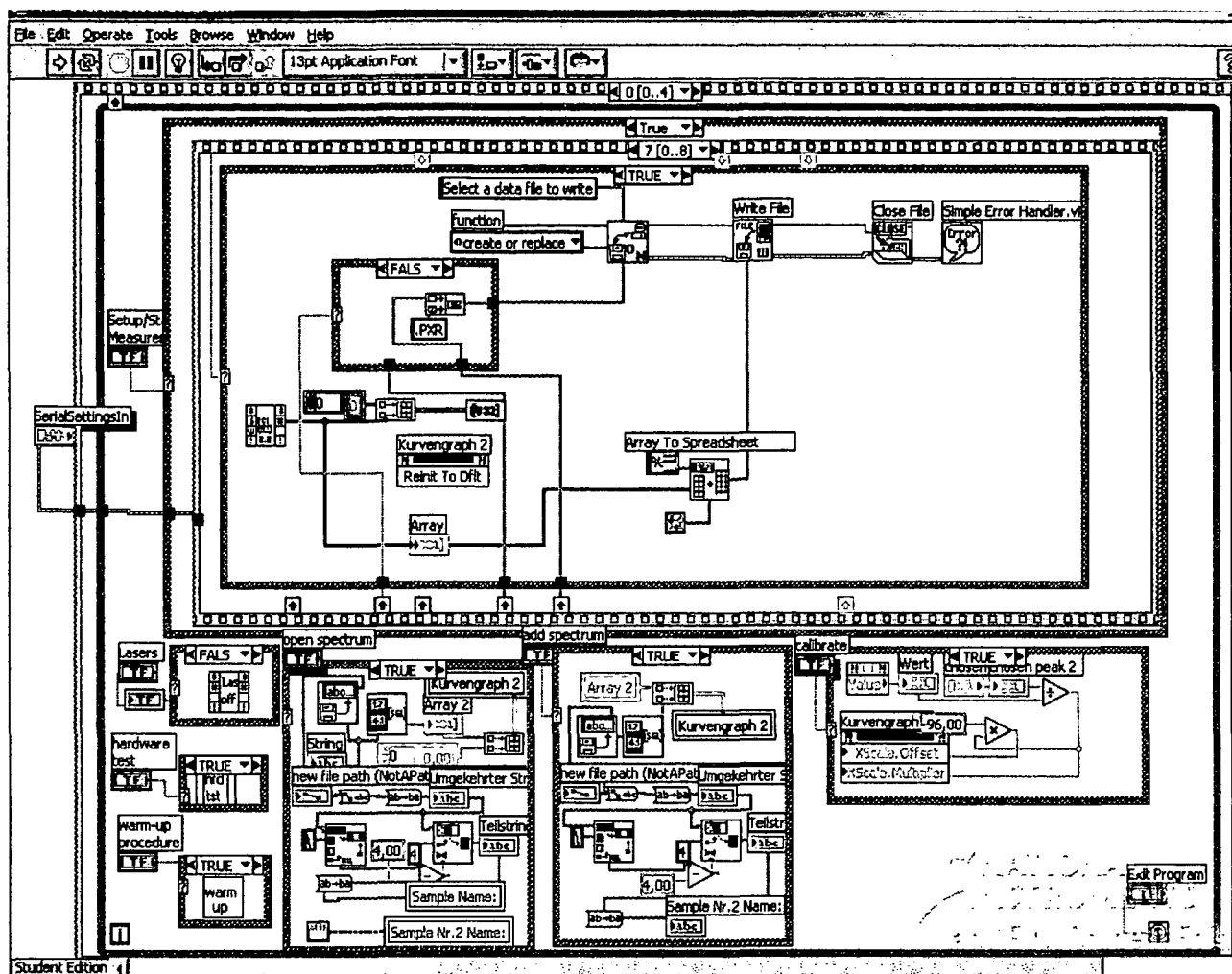


Fig. A.1: Screen shot of the block diagram, showing the first main sequence of the program. Subsequence which displays and saves the spectrum with the chosen file name is displayed in the upper half of the main sequence, and commands to control lasers, to test hardware, to run the warm up procedure, to open and calibrate spectra can be seen in the lower half.

Many VIs (LaserON/OFF, Hardware test, Warm up sequence, Open spectrum etc.) are placed inside *case structures*⁴, and by clicking on the selector terminal the VI inside the structure is activated. Fig. A.7 shows a flowchart of the case structure which is used to turn on and off the lasers.

⁴ Case structure — has one or more subdiagrams, or cases, which are executed when the chosen structure executes.

The data defining serial settings for the interface is passed between the frames of the stacked sequence structure using a sequence local terminal, and is set as following:

Communication port: COM1, RS-232
 Baud rate: 38400 baud
 Configuration: 8 bit, no parity, 1 stop bit

Most of the actions in the software are carried out by sending a command string (as listed in the Chapter A.6.) to an interface using the virtual instrument WriteStringToRCL_2_2.vi, as shown in Fig. A.2.

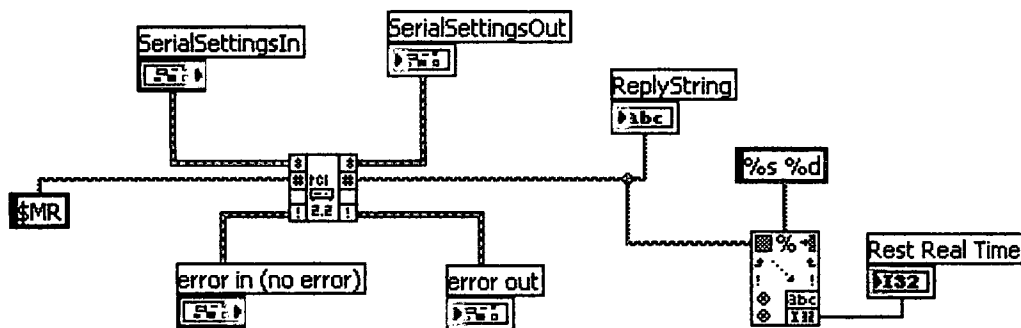
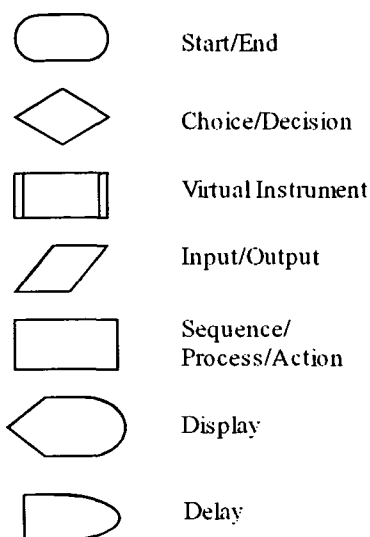


Fig. A.2: An example of sending a command to an interface. Here the **\$MR** string command is sent to the spectrometer using the VI WriteStringToRCL_2_2.vi to inquire the measurement rest real time. The reply string is then converted using “Scan for string” function to get the rest time in milliseconds.

A.9. Flowcharts for Specific Sequences and Subsequences

The following list shows the symbols used in the flowcharts and gives a short explanation.



Virtual Instrument symbol describes the VIs and subroutine VIs (sub-VIs). A short explanation of the action it performs as well as its file name is displayed inside the symbol. The VI's file name has an extension ".vi" (e.g. SetVoltage.vi). Fig. A.3 shows the main flowchart of the actions performed by the PXRF control and analyzing software. Fig. A.4 to Fig. A.7 present flowcharts for more complicated VIs used in the main flowchart, which consist of further sub-VIs.

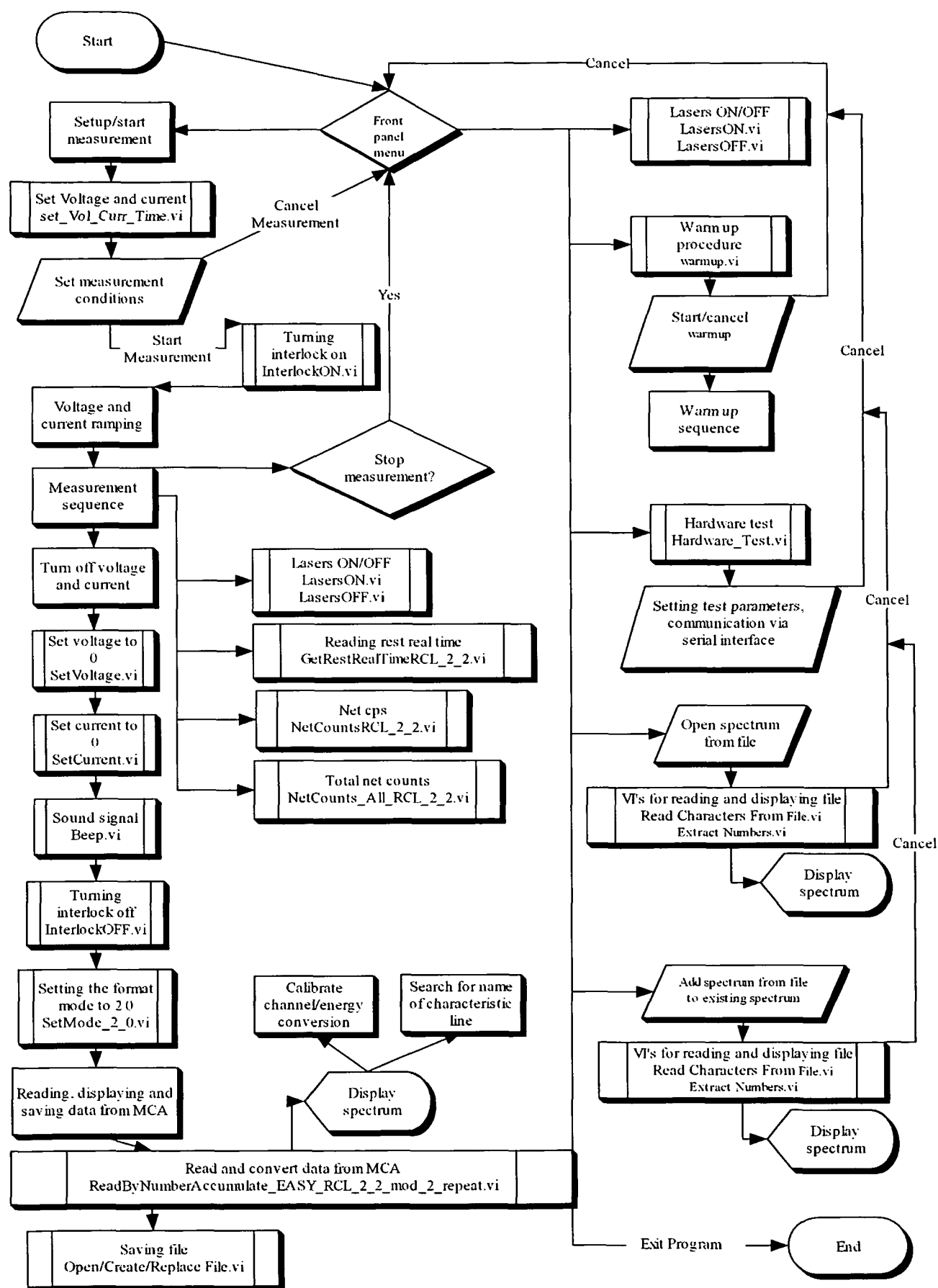
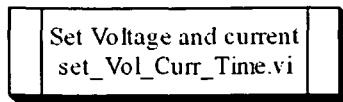
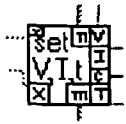


Fig. A.3: Flowchart of the PXRf control and analyzing software.



Flowchart symbol defining this VI used for setting the voltage, current, measurement time, detector energy range.



LabVIEW icon defining this VI.

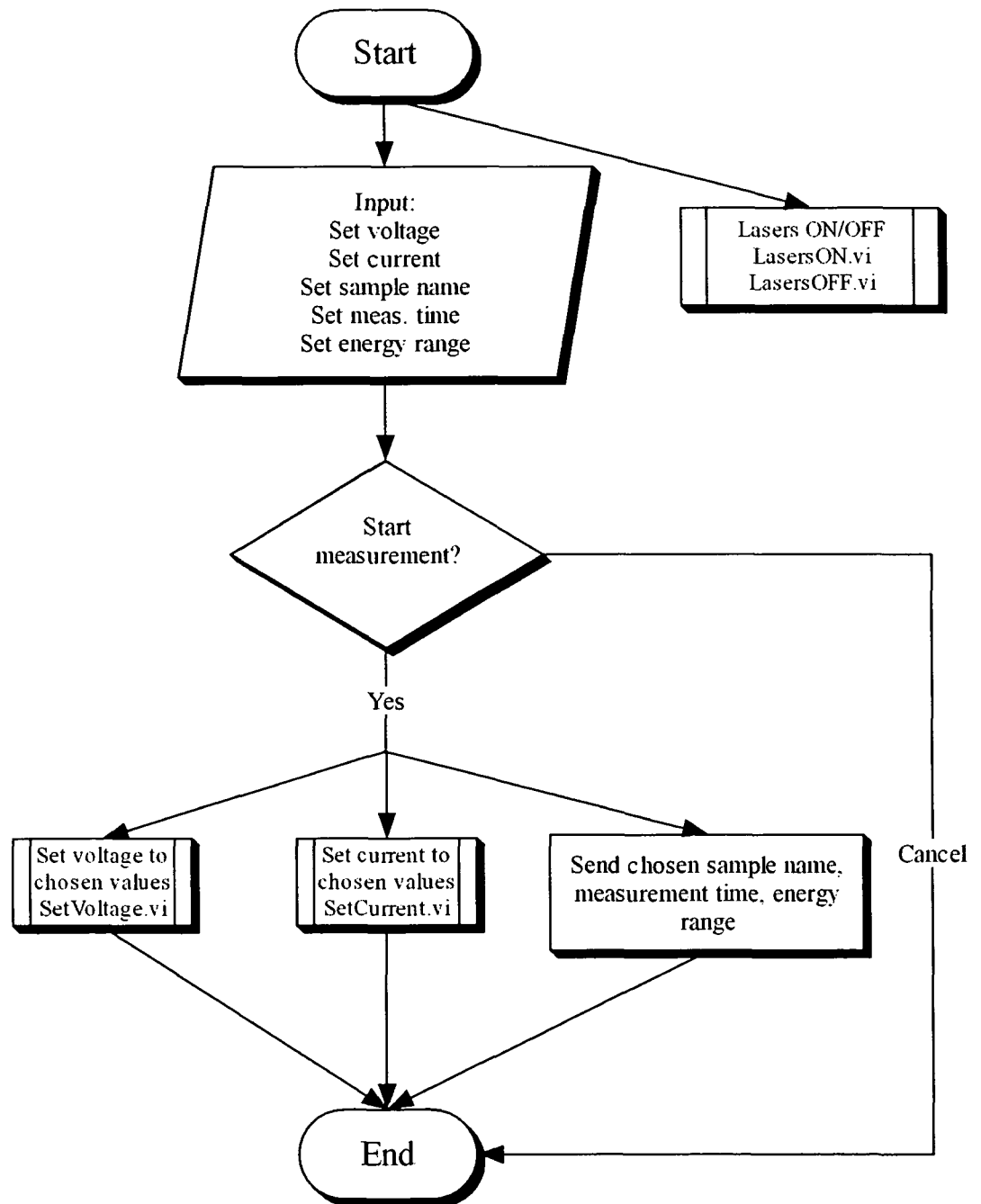
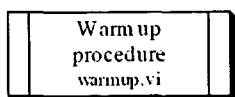


Fig. A.4: Flowchart of the subroutine, which sets measurement conditions.



Flowchart symbol defining this VI which is used to carry out the tube warm up procedure for the PXRF.



LabVIEW software icon defining this VI.

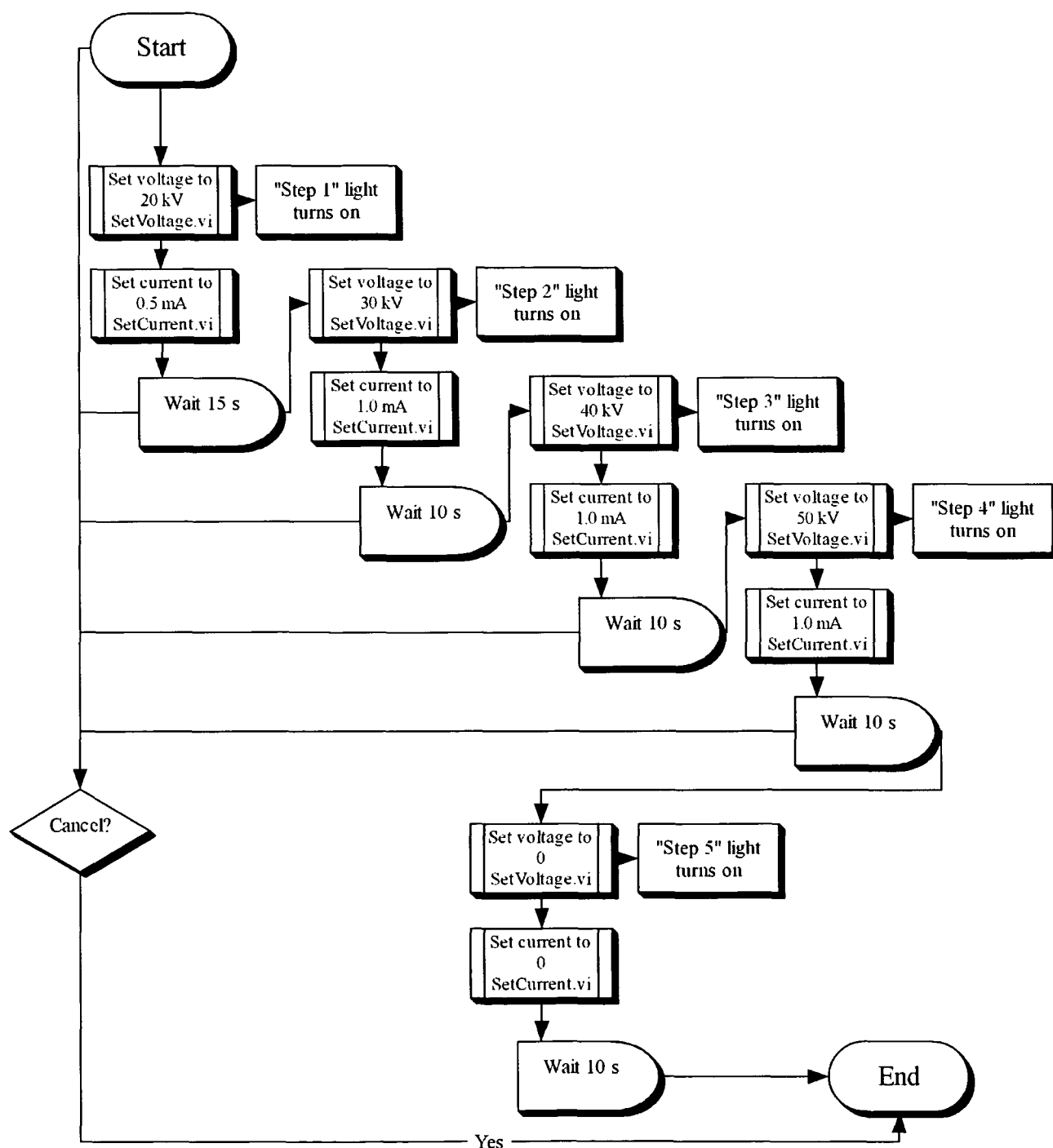
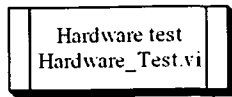


Fig. A.5: Flowchart of a warm up subroutine.



Flowchart symbol defining this VI which is used to test the hardware and communication between single components of the PXRF.



LabVIEW software icon defining this VI.

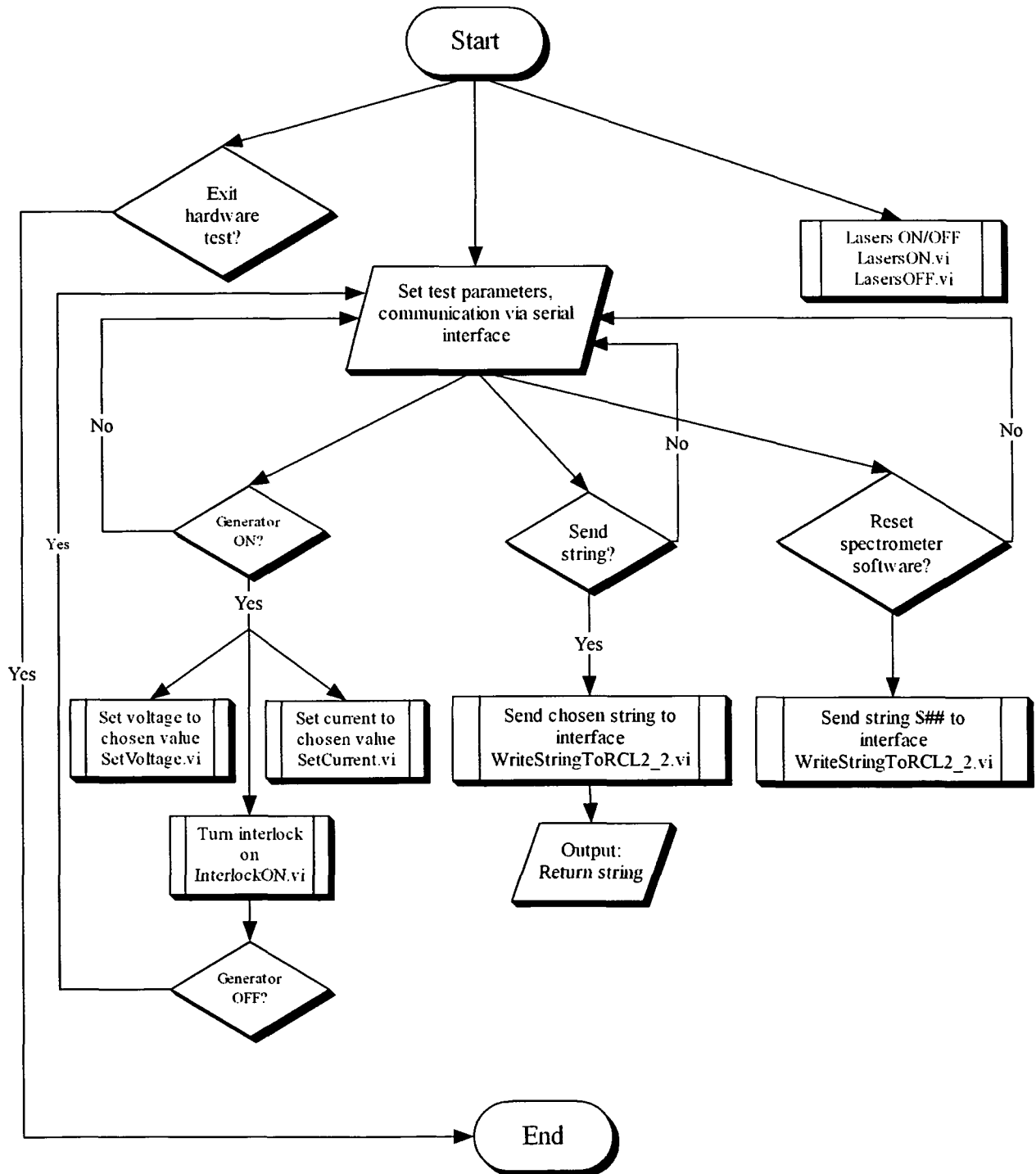
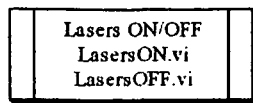
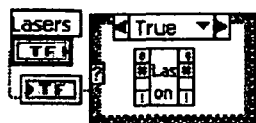


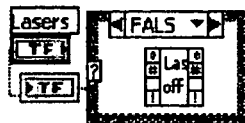
Fig. A.6: Flowchart of subroutine, which allows testing of hardware components and communication between individual components.



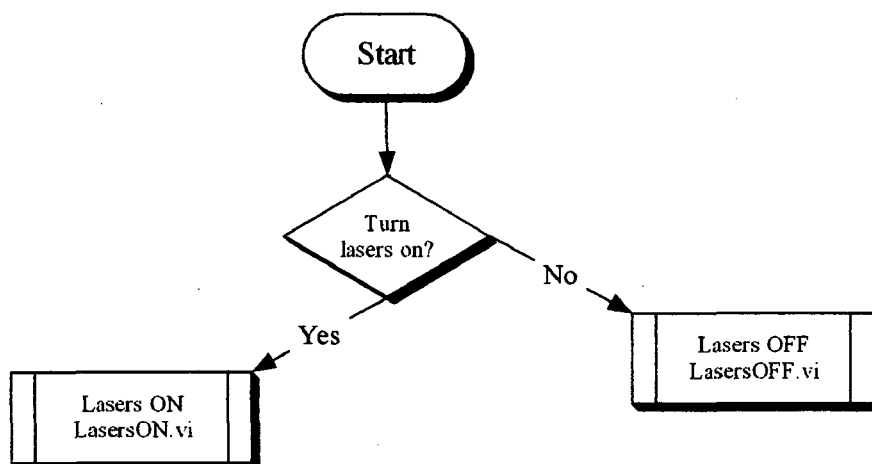
Flowchart symbol defining this VI, which is used to turn on and off the laser pointers.



and

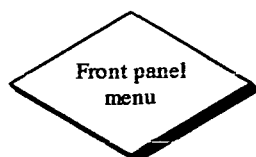


LabVIEW software commands defining these VIs. Two different VIs (LasersON.vi and LasersOFF.vi) are placed within one case structure. By clicking on the boolean selector terminal the VI inside the structure is activated.

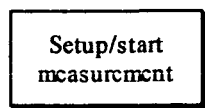


A.7: VIs for turning the lasers on and off, showing the principle of the execution of the case structure commands.

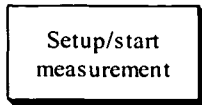
The following is a list of short explanations for each symbol function used in the flowcharts above.



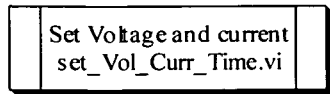
From the front panel (user interface) *main window* all the measurements are started and managed. Furthermore, it allows verification of the instrumental and measuring conditions, as well as monitoring of information relevant for data acquisition (DAQ) during a measurement.



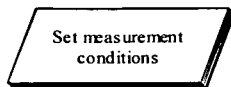
The beginning of the measurement sequence, consisting of 8 subsequent *Stacked Sequence Structures*.



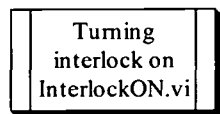
The beginning of the measurement sequence, consisting of 8 subsequent stacked sequence structures.



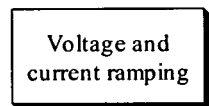
Launches a dialog to set measurement conditions and uses further sub-VI's to pass the data to other VI's.



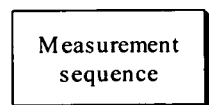
A dialog to set measurement conditions. Choose either to continue with the measurement, or cancel the measurement and return to the main window.



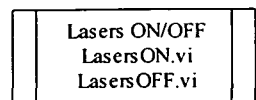
A VI which sends a string **HVP_ON** over the VI WriteStringToRCL_2_2.vi to the HVPS interface, which then turns the interlock on.



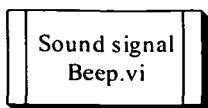
Ramps up the preset voltage and current to the desired values.



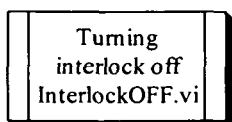
The start of the measurement. During this time the VIs allowing turning on and off of the lasers, reading and displaying count rate and the rest time are active. The measurement can be aborted any time by pressing the Stop Measurement button.



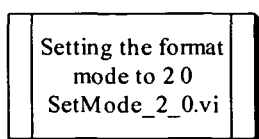
A VI which turns the lasers on and off. It sends the command strings **XR1_ON** and **XR1OFF** to the HVPS interface to turn the lasers on and off, respectively (see Fig. A.7).



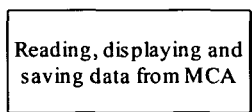
A VI which generates a sound signal. It is used to notify the user that the measurement is finished.



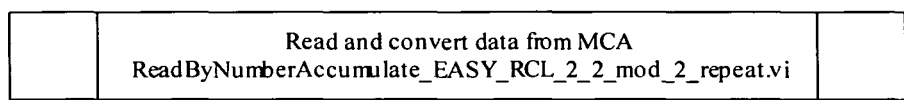
A VI which sends a string **HVPOFF** over the VI WriteStringToRCL_2_2.vi to the HVPS interface, which then turns the interlock off.



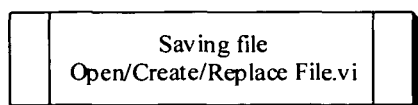
Sets the sending format and mode for SS/SR commands to 2 and 0, by sending the string **\$SM 2 0** to the spectrometer. For detailed explanation of the format and mode sending commands please refer to Chapter A.6.



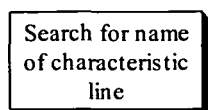
Start of a sequence which reads the measured data from the MCA, displays it as a spectrum and prompts a dialog to save the data as a file.



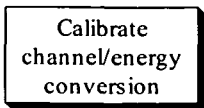
A VI which reads and converts data from MCA. The data is read by using a "sending format mode 2_0" (see Chapter A.6 for command explanation).



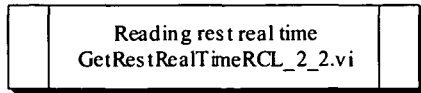
A VI which prompts a dialog to save the data as a file.



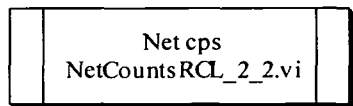
This symbol denotes the sequence which allows searching for the name of a characteristic fluorescent line. So far the energies of around 40 characteristic lines are defined in the program; further line-specific energies will be added.



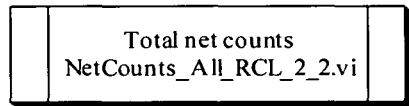
This symbol denotes the sequence which allows energy calibration for a displayed spectrum.



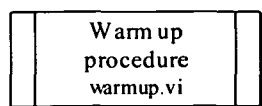
This VI inquires the rest real time from the spectrometer by sending the string **\$MR** over the VI WriteStringToRCL_2_2.vi to the spectrometer (Fig. A.2). The reply string is the rest real time in ms.



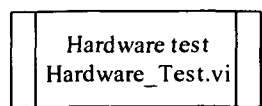
This VI inquires the net count rate from the spectrometer by sending the string **\$NC** over the VI WriteStringToRCL_2_2.vi to the spectrometer. The reply string is the count rate in cps.



This VI reads the total net count from the spectrometer by sending the string **\$NI** over the VI WriteStringToRCL_2_2.vi to the spectrometer.



This VI consisting of further sub-VIs starts the warm up procedure. For detailed flowchart see Fig. A.5.



This VI consisting of further sub-VIs starts the sequence to test hardware and communication between single components. For detailed flowchart see Fig. A.6.

	VI's for reading and displaying file Read Characters From File.vi Extract Numbers.vi	
--	--	--

Two VIs used in the sequence to open an existing spectrum from a file and display it. Both of these VIs are already predefined in LabVIEW development software and can be found in the “examples” section of the original software.

APENDIX B

X-Ray Absorption Edges

X-ray characteristic absorption edges for some elements, important for spectroscopic applications.

Atomic Number	Element	Edge	Energy (keV)	Wavelength (Å)
11	Na	K	1.0721	11.5646
12	Mg	K	1.3050	9.5007
13	Al	K	1.5596	7.9497
14	Si	K	1.8389	6.7423
15	P	K	2.1455	5.7788
16	S	K	2.4720	5.0155
17	Cl	K	2.8224	4.3929
18	Ar	K	3.2029	3.8710
19	K	K	3.6074	3.4369
20	Ca	K	4.0381	3.0704
22	Ti	K	4.9664	2.4965
23	V	K	5.4651	2.2687
24	Cr	K	5.9892	2.0701
25	Mn	K	6.5390	1.8961
26	Fe	K	7.1120	1.7433
27	Co	K	7.7089	1.6083
28	Ni	K	8.3328	1.4879
29	Cu	L-I	1.0081	12.2988
		K	8.9789	1.3808
		L-I	1.0961	11.3114
30	Zn	K	9.6586	1.2837
		L-I	1.1936	10.3874
		L-II	1.0428	11.8896
		L-III	1.0197	12.1589
31	Ga	K	10.3671	1.1959
		L-I	1.2977	9.5542
		L-II	1.1423	10.8539
		L-III	1.1154	11.1157
32	Ge	K	11.1031	1.1167
		L-I	1.4143	8.7665
		L-II	1.2478	9.9362
		L-III	1.2167	10.1902

33	As	K	11.8667	1.0448
		L-I	1.5265	8.1221
		L-II	1.3586	9.1259
		L-III	1.3231	9.3707
34	Se	K	12.6578	0.9795
		L-I	1.6539	7.4965
		L-II	1.4762	8.3989
		L-III	1.4358	8.6352
35	Br	K	13.4737	0.9202
		L-I	1.7820	6.9576
		L-II	1.5960	7.7684
		L-III	1.5499	7.9995
38	Sr	K	16.1046	0.7699
		L-I	2.2163	5.5942
		L-II	2.0068	6.1782
		L-III	1.9396	6.3923
40	Zr	K	17.9976	0.6889
		L-I	2.5316	4.8975
		L-II	2.3067	5.3750
		L-III	2.2223	5.5791
42	Mo	K	19.9995	0.6199
		L-I	2.8655	4.3268
		L-II	2.6251	4.7230
		L-III	2.5202	4.9196
45	Rh	K	23.2199	0.5340
		L-I	3.4119	3.6339
		L-II	3.1461	3.9409
		L-III	3.0038	4.1276
46	Pd	K	24.3503	0.5092
		L-I	3.6043	3.4399
		L-II	3.3303	3.7229
		L-III	3.1733	3.9071
47	Ag	K	25.5140	0.4859
		L-I	3.8058	3.2578
		L-II	3.5237	3.5186
		L-III	3.3511	3.6998
48	Cd	K	26.7112	0.4642
		L-I	4.0180	3.0857
		L-II	3.7270	3.3266
		L-III	3.5375	3.5049
50	Sn	K	29.2001	0.4246
		L-I	4.4647	2.7770
		L-II	4.1561	2.9832
		L-III	3.9288	3.1558
51	Sb	K	30.4912	0.4066

52	Te	L-I	4.6983	2.6389
		L-II	4.3804	2.8304
		L-III	4.1322	3.0004
		K	31.8138	0.3897
		L-I	4.9392	2.5102
		L-II	4.6120	2.6883
53	I	L-III	4.3414	2.8559
		M1	1.0060	12.3245
		K	33.1694	0.3738
		L-I	5.1881	2.3898
		L-II	4.8521	2.5553
		L-III	4.5571	2.7207
55	Cs	M1	1.0721	11.5646
		K	35.9846	0.3445
		L-I	5.7143	2.1697
		L-II	5.3594	2.3134
		L-III	5.0119	2.4738
		M1	1.2171	10.1869
56	Ba	M2	1.0650	11.6417
		K	37.4406	0.3311
		L-I	5.9888	2.0703
		L-II	5.6236	2.2047
		L-III	5.2470	2.3630
		M1	1.2928	9.5904
74	W	M2	1.1367	10.9074
		M3	1.0622	11.6724
		K	69.5250	0.1783
		L-I	12.0998	1.0247
		L-II	11.5440	1.0740
		L-III	10.2068	1.2147
78	Pt	M1	2.8196	4.3972
		M2	2.5749	4.8151
		M3	2.2810	5.4355
		M4	1.8716	6.6245
		M5	1.8092	6.8530
		K	78.3948	0.1582
79	Au	L-I	13.8799	0.8933
		L-II	13.2726	0.9341
		L-III	11.5637	1.0722
		M1	3.2960	3.7617
		M2	3.0265	4.0966
		M3	2.6454	4.6868
		M4	2.2019	5.6308
		M5	2.1216	5.8439
		K	80.7249	0.1536

80	Hg	L-I	14.3528	0.8638
		L-II	13.7336	0.9028
		L-III	11.9187	1.0402
		M1	3.4249	3.6201
		M2	3.1478	3.9388
		M3	2.7430	4.5200
		M4	2.2911	5.4116
		M5	2.2057	5.6211
		K	83.1023	0.1492
		L-I	14.8393	0.8355
		L-II	14.2087	0.8726
		L-III	12.2839	1.0093
		M1	3.5616	3.4811
		M2	3.2785	3.7817
		M3	2.8471	4.3548
81	Tl	M4	2.3849	5.1987
		M5	2.2949	5.4026
		K	85.5304	0.1450
		L-I	15.3467	0.8079
		L-II	14.6979	0.8436
		L-III	12.6575	0.9795
		M1	3.7041	3.3472
		M2	3.4157	3.6298
		M3	2.9566	4.1935
		M4	2.4851	4.9891
		M5	2.3893	5.1891
		K	88.0045	0.1409
		L-I	15.8608	0.7817
		L-II	15.2000	0.8157
		L-III	13.0352	0.9511
82	Pb	M1	3.8507	3.2198
		M2	3.5542	3.4884
		M3	3.0664	4.0433
		M4	2.5856	4.7952
		M5	2.4840	4.9913
		K	90.5259	0.1370
		L-I	16.3875	0.7566
		L-II	15.7111	0.7892
		L-III	13.4186	0.9240
		M1	3.9991	3.1003
		M2	3.6963	3.3543
		M3	3.1769	3.9027
		M4	2.6876	4.6132
		M5	2.5796	4.8063
		K	90.5259	0.1370
83	Bi	L-I	16.3875	0.7566
		L-II	15.7111	0.7892
		L-III	13.4186	0.9240
		M1	3.9991	3.1003
		M2	3.6963	3.3543
		M3	3.1769	3.9027
		M4	2.6876	4.6132
		M5	2.5796	4.8063
		K	90.5259	0.1370
		L-I	16.3875	0.7566
		L-II	15.7111	0.7892
		L-III	13.4186	0.9240
		M1	3.9991	3.1003
		M2	3.6963	3.3543
		M3	3.1769	3.9027
		M4	2.6876	4.6132
		M5	2.5796	4.8063

APPENDIX C

High Voltage Power Supply (HVPS) Interface

(to be used with a model HVPS Matsusada HXR-505-50-01)

C.1. Technical Specifications

Communication port:	RS-232, duplex
Transfer speed:	96000 baud
Configuration:	8, bit, no parity, 1 stop bit
Manipulation (Handshaking):	hardware
Connector:	25 pin, F
<u>Outputs:</u>	
Lasers 1 & 2:	5 V DC, 100 mA max, Isolated cinch connector, black
Output 2 (not used):	5 V DC, 100 mA max, Isolated cinch connector, yellow
Interlock:	40 V DC, 100 mA max, Turned ON = contact with GND Non-isolated cinch connector, yellow
Voltage control output: (0 – 10V >> 0 – 50 kV) +/- 1%	0 – 10 V DC / 5mA max, 5kV/V
Current control output: (0 – 10V >> 0 – 50 kV) +/- 1%	0 – 10 V DC / 5mA max, 0,1mA /V
<u>Inputs:</u>	
Current monitoring input:	0.02-10 V >> 0.02 – 0.999 mA +/- 2%
Voltage monitoring input:	0.02-10 V >> 1 – 50 kV +/- 2%
<u>Power supply:</u>	
	220 V AC / 12V DC adapter, 400mA Plus on inner contact
Fuse:	0.315 A (F)

C.2. Programming

Interface decodes commands obtained via RS-232 port by checking a 6 byte sequence, i.e. 6 ASCII characters (capital letters and numbers) and executes them according to the following table:

ASCII sequence	Example	Command
XR1_ON	XR1_ON	Turns on laser 1 & 2
XR1OFF	XR1OFF	Turns off laser 1 & 2
XR2_ON	XR2_ON	Turns on output 2
XR2OFF	XR2OFF	Turns off output 2
HVP_ON	HVP_ON	Turns on interlock contact
HVPOFF	HVPOFF	Turns off interlock contact
HVI n1 n2 n3	HVI385	Sets current output to 0.385 mA *
HVU n1 n2 n3	HVU125	Sets voltage output to 12.5 kV *
HV???I	HV???I (0.385mA)	Sends readings about measured current, 7 ASCII character sequence, i.e. 0 . n1 n2 n3 mA
HV???U	HV???U (12.5kV)	Sends readings about measured voltage, 7 ASCII character sequence, first (and others for values under 10) is always blank (blank, ASCII code 32) i.e. bl n1 n2 . n3 kV

* n1, n2, n3 – three digits of a number

Notice: During command decoding, except for commands HVUnnn and HVInnn, the 4th and the 5th byte are not affected, so they can be interchanged with any character (command XR1xxN will be executed as XR1_ON). The sequence is decoded continuously, so in case of a false command the first next correct character order in the sequence continuation will be accepted.

C.3. Connecting the Cables

Connect the communication port (RS-232) to a standard 25-pin serial cable for modem-computer connection (NOT null-modem cable) or to an USB/serial adapter for a laptop.

Connect I/O Control connector using a 9-pin 1:1 cable (pins connected with same numbers) to a voltage control connector J5 of the high-voltage power supply. Connect the other I/O control connector with an appropriate cable to a monitor connector J4 of the high-voltage power supply (both I/O connectors are connected parallel, so that pins with the same number are interlinked).

I/O connector (interface)	J4 (HV source)
Pin 2 -----	Pin 2 kV mon
Pin 5 -----	Pin 3 mA mon
Pin 9 -----	Pin 1 GND

Lasers should be connected by attaching “+” to the inner contact of the connector, and “-” to the outer contact. Figure C.1 shows the adapter and adequate connecting of the cables.

Interlock connection is connected according to Figure C.2, by attaching “+” to the inner contact of the connector. The outer cinch contact must be connected to ground (GND) of the loop. Interlock connector will be bypassed after receiving command HVP_ON and allow closing the interlock loop to ground.

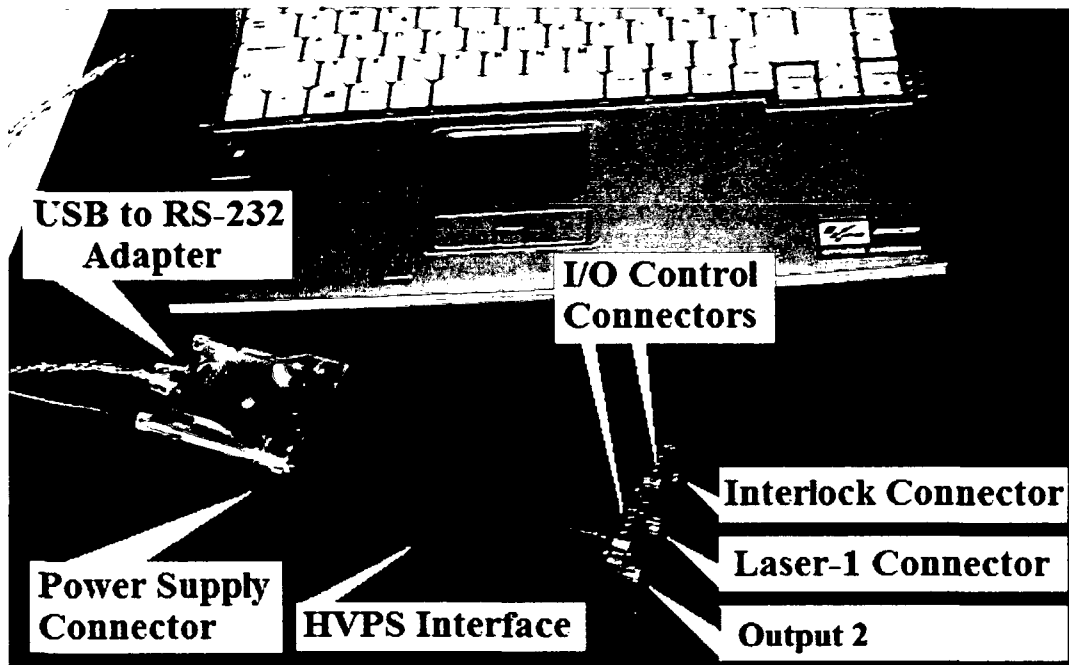


Fig. C.1: HVPS interface with the connection scheme.

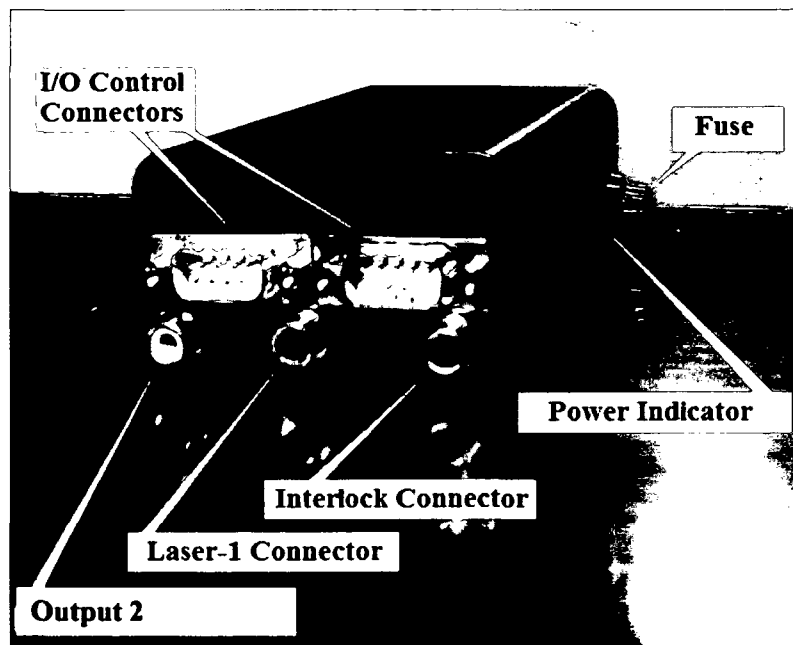


Fig. C.2: Side of the HVPS interface showing the connectors for lasers, interlock, and input/output controls

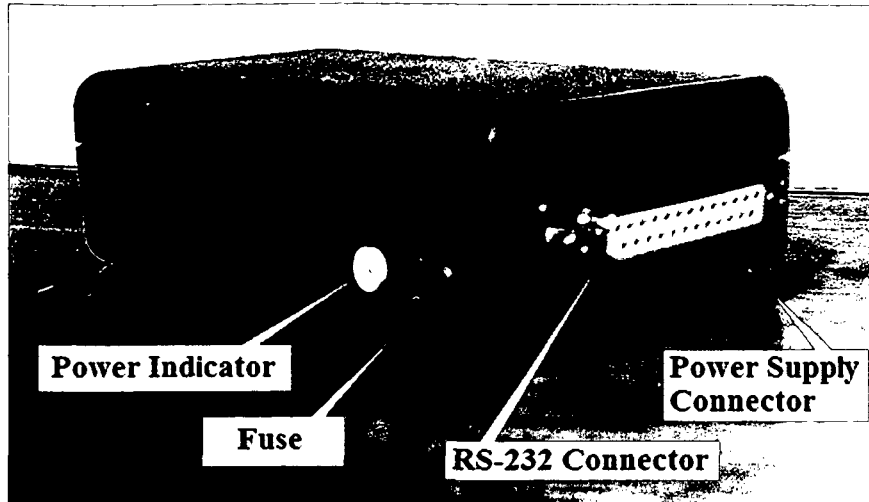


Fig. C.3: Side of the HVPS interface showing the red lamp power indicator and the fuse case, as well as connectors for RS-232 interface, and interface power supply.

C.4. Software and Operational Tests

Any software supporting RS-232 communication port (COM port on a PC) can be used. For test operations under Windows operation system it is recommended to use a program called HYPERTERMINAL, which can be found in the Windows Accessories program support. If this program is not installed, it can be installed from Control Panel (Add or Remove Programs, Add Windows Components). COM port settings should be set to 9600 baud, 8 bit, no parity, 1 stop bit. To test AD/DA operational functioning a voltmeter and a 9-pin Sub-D connector is needed. To connect this connector use the following scheme:

Pin 2 and 3 connected together	-----	control voltage for kV, 0-10 V
Pin 5 and 6 connected together	-----	control voltage for mA, 0-10 V
Pin 9	-----	ground (GND)

After sending a command for setting voltage or current, the voltmeter displays a corresponding control voltage, and using the commands HV???U and HV???I the same voltage can be displayed via PC.

Notice: Accuracy of the AD converter for measuring the control voltage is less accurate than the DA converted value, and should serve only to control the proper functioning of the High

Voltage (HV) source. In case there is a need to adjust the output voltage for control of the HV source, it can be accomplished using potentiometers on the circuit board, as shown in Figure C4.

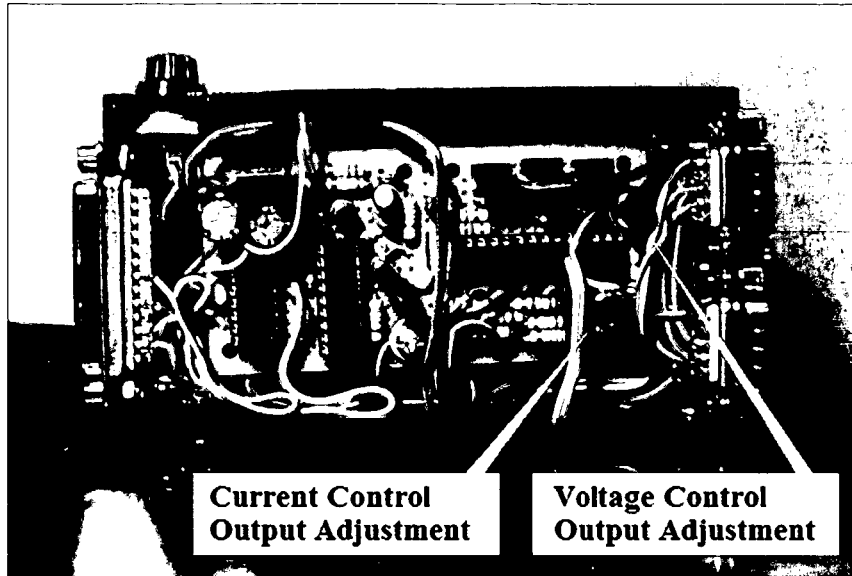


Fig. C.4: Potentiometers on the circuit board, used for adjusting the output voltage for voltage and current controls.

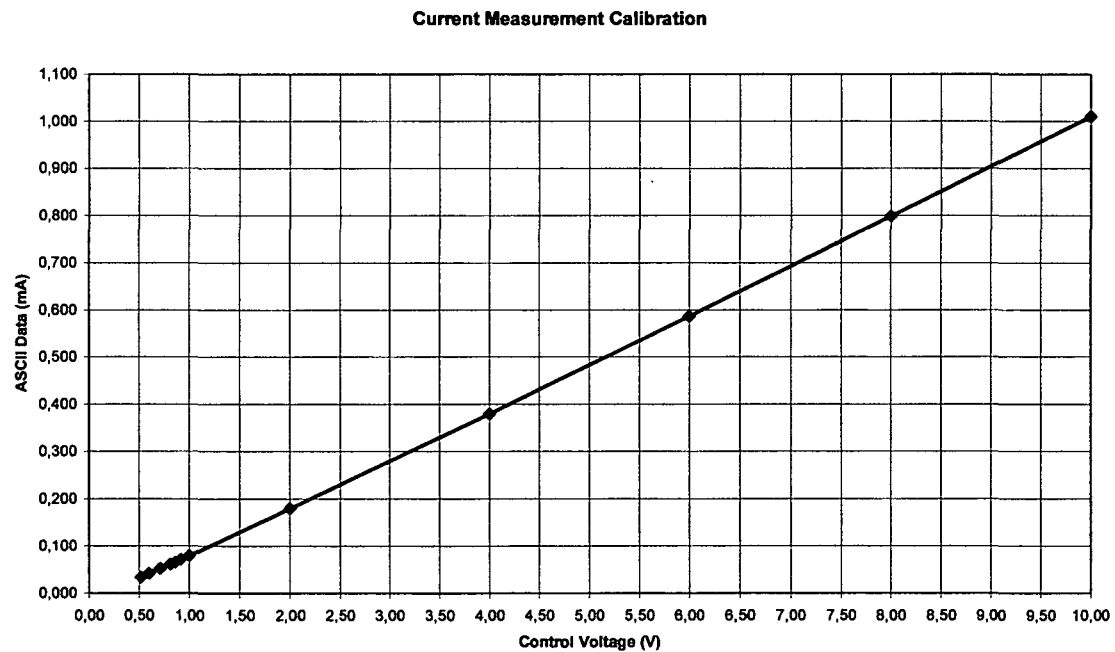
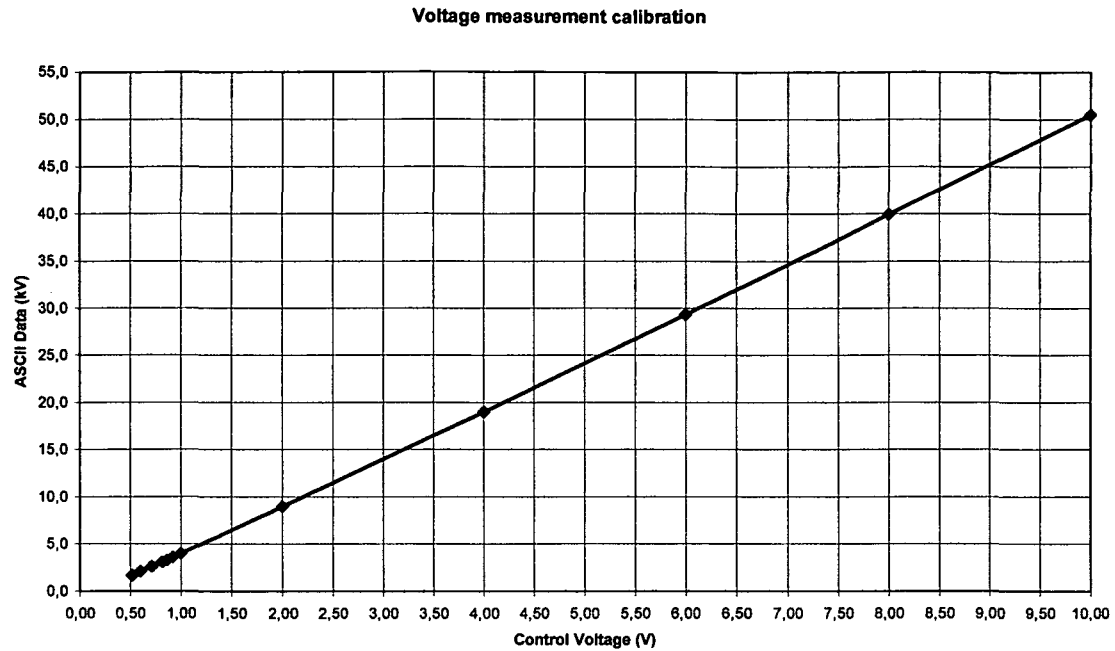


Figure C.5: Calibration spectra for conversion operations of the AD/DA converter. The x-axis shows the applied control voltage and the y-axis the ASCII data, corresponding to the output voltage and current, respectively.

Curriculum Vitae

Personal Data

Name: Vladan Desnica
Date of Birth: 29.12.1971
Place of Birth: Zagreb, Croatia
Address: Gymnasiumstr. 85, 1190 Vienna, Austria

Education

1978 – 84 Elementary School, Zagreb, Croatia
1984 – 87 Daley Middle School + Lowell High School, Lowell, MA, USA
1988 – 90 Secondary School, Zagreb, Croatia
6/90 Graduation exam (Matura)
1991 – 92 German language – obligatory preliminary study course
(Vorstudienlehrgang)

1992 – 2001 Study of Physics at the University of Vienna
Diploma Thesis: “Charakterisierung von historischen Farbpigmenten mittels
Röntgenfluoreszenzanalyse, Röntgenbeugung, Raman- und IR-
Spektroskopie”, carried out at the Institute for Solid State Physics at the
TU Vienna, under supervision of Prof. Dr. Mantler.

2002 – 2004 PhD Study at the Vienna University of Technology
PhD Thesis: “Development, Construction and Application of a Portable X-Ray
Fluorescence Device for the Analysis of Art Objects”, carried out at the
Institute of Science and Technology in Art of the Academy of Fine Arts
in Vienna, under supervision of Prof. Dr. Schreiner.

Publications

M. Schreiner, V. Desnica, D. Jemrih-Simbuerger,
Naturwissenschaftliche Untersuchungen an der Heiligen Lanze,
in: Die Heilige Lanze in der geistlichen Schatzkammer des KHM in
Wien (working title). F. Kirchweger Herausgeber, KHM Wien 2005, in
press.

V. Desnica, M. Furic, M. Schreiner, Multianalytical characterization of
a variety of ultramarine pigments, *e-Preservation Science* 1, 2004, 15-
21.

V. Desnica, K. Furic, B. Hochleitner, M. Mantler, A Comparative
analysis of five chrome green pigments based on different spectroscopic
techniques, *Spectrochimica Acta B* 58, 2003, 681-687.

B. Hochleitner, V. Desnica, M. Mantler, M. Schreiner, Historical
pigments: a collection analyzed with X-ray diffraction analysis and

X-ray fluorescence analysis in order to create a database, *Spectrochimica Acta B* 58, 2003, 641-649.

D. Jembrih-Simbuerger, V. Desnica, M. Schreiner, E. Thobois, H. Singer, K. Bouvagnet, Paintings and drawings of A. Duerer in Albertina, Wien, *Techné*, submitted.

V. Desnica, M. Schreiner, Application of a portable X-ray fluorescence device for the analysis of art objects, *X-Ray Spectrometry*, submitted.

Conferences/Presentations

Talk at the ChemArt Symposium (Chemie in Kunst und Denkmalpflege): V. Desnica, M. Schreiner, "Anwendung eines tragbaren RFA-Geraetes zur Analyse von Kunstobjekten", September 2004, Vienna, Austria.

Talk at the European X-Ray Spectrometry Conference (EXRS): V. Desnica, M. Schreiner, "Development and application of a portable X-Ray Device in art and archaeometry", June 2004, Alghero, Italy.

Poster presentation at the Festkoerperanalytik Conference (FKA): V. Desnica, M. Schreiner, "Importance of using different analytical techniques for pigment characterization", September 2003, Vienna, Austria.

Poster presentation at the International Conference on X-Ray Optics and Microanalysis (ICXOM): V. Desnica, K. Furic, M. Mantler, "A comparative analysis of five Cr-based green pigments by using XRF, XRD, Raman- and IR-Spectroscopy" July 2001, Vienna, Austria.

Experimental Methods used during M.Sc. and Ph.D. Studies

X-ray diffraction (XRD), X-ray fluorescence (XRF), including micro-XRF, Raman spectroscopy, Fourier transform infrared spectroscopy (FTIR), including micro-FTIR, colorimetry.

Collaborations

Institute of Solid State Physics, Prof.Dr. M. Mantler, Vienna University of Technology, Austria.

Division of Material Physics, Dr. K. Furić, "R. Bošković" Institute, Zagreb, Croatia.

Croatian Conservation Institute, K. Škarić, Zagreb, Croatia.

Military Service 1990 – 91

Obligatory military service (12 months)